



Norwegian University of
Science and Technology

Impact against coated offshore steel pipes

Steffen Hammersvik
Eirik Bugge Kulsrud

Master of Science in Engineering and ICT

Submission date: June 2017

Supervisor: Tore Børvik, KT

Co-supervisor: Magnus Langseth, KT
Ole Vestrum, KT

Norwegian University of Science and Technology
Department of Structural Engineering



MASTER THESIS 2017

SUBJECT AREA: Computational Mechanics	DATE: 11.06.2017	NO. OF PAGES: 16 – 114 – 13
--	---------------------	--------------------------------

TITLE: **Impact against coated offshore steel pipes**
Støt på offshore stålrør med isolasjonslag av polymer

BY:

Steffen Hammersvik
Eirik Bugge Kulsrud



SUMMARY: This thesis is part of an ongoing research program between SIMLab and Statoil about impacts on coated offshore pipelines. Impact loads may occur from objects such as anchors or trawls, causing severe damage to the pipe which may lead to oil or gas production to shut down. The steel pipe had been sufficiently researched concerning the impact event, but much work remained on the coating.

The coating investigated in this thesis was the five layer polymer insulation system, Thermotite, produced by Shawcor (formerly Bredero Shaw). The main focus was to characterise the porous polypropylene layer. Experiments were conducted; X-ray computed tomography to get a look inside the coating and determine the pore morphology by image analyses, and uniaxial compression tests to investigate the mechanical properties. Image analyses suggested several statistics of the pore structure. The results showed that the morphology is highly inhomogeneous and anisotropic. Furthermore, the relative density was varying between 0.7 to 1.0 depending on the radial coordinate of the pipe. The lowest value was found in the middle. The pore structures on either side, were different (asymmetric morphology). The reason for that was assumed to be the extrusion process during manufacturing. The other directions (hoop and axial) revealed no dependency.

The uniaxial compression tests suggested that the pores affect the strength of the polymer significantly. The different pore structures seemed to have a distinct effect on the force-displacement behaviour. The coating was characterised as a solid with isolated pores, not foam because the transverse expansion was greater than zero and the high relative density. Compression tests on solid polypropylene were employed to establish a material model, calibrated by the use of edge tracing and inverse modelling. The model assumed isotropic hardening and insensitivity to temperature, pressure, and strain rate.

To numerically re-create the test specimens, a direct modelling technique was employed. The method utilises the computed tomography image slices to replicate the samples. A sensitivity study indicated that the accuracy of the models was sensitive to mesh size, friction and the material model properties. Compared to the experimental values, the simulations were satisfactory, but a bit stronger, most likely due to insufficient mesh refinement. However, the models captured the shape of the deformation and the force-displacement curves. The numerical models were employed to characterise the coating further. The simulations suggested that the reduction in yield force is due to strain localisation between adjacent pores. Simulations of the re-created specimens subjected to tension suggested that the tensile strength is significantly lower than the compressive strength, as the strain gets strongly localised. Mechanical anisotropy (orthotropy) was investigated as well. The results indicated differences throughout the height of the porous layer, and that the coating was weaker when compressed in the radial direction.

A block of porous polypropylene layer was simulated under compression. To re-create the pore structure of the coating satisfactorily, the block needed about one million elements. Therefore, it was assumed that a large-scale simulation of the pipe with the direct modelling technique would require too many elements.

RESPONSIBLE TEACHER: Tore Børvik

SUPERVISOR(S): Tore Børvik, Ole Vestrum and Magnus Langseth (NTNU). Håvar Iltstad (Statoil)

CARRIED OUT AT: Department of Structural Engineering, NTNU



MASTER THESIS 2017

FAGOMRÅDE: Beregningsmekanikk	DATO: 11.06.2017	ANTALL SIDER: 16 – 114 – 13
----------------------------------	---------------------	--------------------------------

TITTEL: **Støt på offshore stålrør med isolasjonslag av polymer**
Impact against coated offshore steel pipes

UTFØRT AV:

Steffen Hammersvik
Eirik Bugge Kulsrud



SAMMENDRAG: Denne oppgaven er en del av et pågående forskningsprogram på isolerte offshore stålrør utsatt for støtlast, i samarbeid med SIMLab og Statoil. Offshore rør blir fra tid til annen utsatt for støtlaster fra blant annet ankre eller tråler, og kan føre til så store skader at produksjonen må stoppes. Rikelig med arbeid har blitt utført på ståldelen av røret, men mye arbeid gjenstår på isoleringen.

Isoleringen undersøkt i denne oppgaven, var et femlags polymeriseringsssystem, Thermotite, produsert av Shawcor (tidligere Bredero Shaw). Hovedfokuset var å karakterisere det porøse polypropylenlaget. To forsøk ble utført. X-ray computertomografi ble brukt for å betrakte innsiden av det porøse laget, samt bestemme poremorfologien ved hjelp bildeanalyser. Enaksiale komprimeringstester ble gjort for å undersøke de mekaniske egenskapene. Bildeanalysene indikerte flere egenskaper om porestrukturen. Det ble funnet at morfologien er svært inhomogen og anisotropisk. Videre var den relative tettheten varierende mellom 0.7 og 1.0, samt avhengig av rørets radielle koordinat. Den laveste verdien ble funnet i midten. Porestrukturene på hver side av midten var forskjellige (asymmetrisk morfologi). Det var antatt at dette skyldtes ekstruderingsprosessen under produksjonen. De andre retningene viste ingen avhengighet.

De enaksiale kompresjonstestene antydte at porene påvirker det porøse polymerens styrke betydelig. De forskjellige porestrukturene virker til å ha en tydelig effekt på styrken. Isoleringlaget ble karakterisert som et fast stoff med isolerte porer, istedenfor skum, ettersom tverrkontraksjonen var større enn null og dens høye relative tetthet. Kompresjonstester på rent polypropylen ble benyttet for å etablere en materialmodell, kalibrert ved å måle tverrforskyvningen og invers modellering. Modellen antok isotropisk herding og tok ikke hensyn til effekten av temperatur, trykk og belastningshastighet.

En direkte-modelleringsteknikk ble benyttet for å gjenskape testprøvene. Metoden benytter CT-bilder for å duplisere prøvene. En sensitivitetsstudie indikerte at nøyaktigheten av modellene var følsom for mesh-størrelse, friksjon og materialmodellen. Sammenlignet med eksperimentelle verdier var simuleringene tilfredsstillende, men litt sterkere, trolig grunnet utilstrekkelig mesh-størrelse. Imidlertid fanget modellene deformasjonsformen og kurvaturen til kraft-forskyvningskurverne. De numeriske modellene ble benyttet for å karakterisere isoleringlaget ytterligere. Simuleringene antydte at reduksjonen i flytningskraften skyldes lokalisering mellom nærliggende porer. Simuleringer av de gjenskapte prøvene utsatt for spenning antydte at strekkstyrken er betydelig lavere enn kompresjonsstyrken, ettersom flytningen blir sterkt lokalisert. Mekanisk anisotropi (ortotropi) ble også undersøkt. Resultatene indikerte forskjeller gjennom høyden av det porøse laget, og at det var svakere for kompresjon i radiell retning.

En blokk av det porøst polypropylenlag ble simulert for kompresjon. For å tilstrekkelig gjenskape porestrukturen av isoleringlaget, trengte blokken omtrent en million elementer. Det ble derfor antatt at en storskala simulering av røret ved bruk av direkte-modelleringsteknikken ville kreve for mange elementer.

FAGLÆRER: Tore Børvik

VEILEDER(E): Tore Børvik, Ole Vestrum and Magnus Langseth (NTNU). Håvar Ilstad (Statoil)

UTFØRT VED: Department of Structural Engineering, NTNU

MASTER'S THESIS 2017

for

Steffen Hammersvik and Eirik Bugge Kulsrud

Impact against coated offshore steel pipes

1. INTRODUCTION

After discussions with Statoil and Gassco, a need for increased knowledge regarding behaviour, modelling and design of subsea constructions exposed to impact loading from e.g. trawl gear have been identified. Metallurgical investigations have shown that cracks may propagate from the internal wall of the steel pipe after an impact event, making such fractures hard to discover – which in turn may result in severe consequences. Previous studies have indicated the protective effect of polymeric coating in the events of impact against pipelines. In this master thesis, the beneficial contribution of a specific coating systems which is found on steel pipelines, will be further investigated. This will be done in conjunction with advanced numerical simulations. Accurate numerical models will be an invaluable aid when predicting the probability of fracture after an impact event.

2. OBJECTIVES

The main objective of the research project is to examine the behaviour of polymeric coating to determine how coated steel pipes can be numerically modelled under impact loading.

3. A SHORT DESCRIPTION OF THE RESEARCH PROJECT

The main topics in the research project will be as follows;

1. A comprehensive literature review will be conducted to understand the pipe impact event, impact load design, testing facilities, constitutive and failure modelling of metallic and polymer materials exposed to extreme loadings, and explicit finite element methods.
2. A thorough material characterization of the polymer coating material will be performed using various experimental methods, including computer tomography (CT).
3. Important material parameters will be obtained through post-processing of experimental data.
4. Non-linear FE numerical simulations of the porous coating will be performed, and the numerical results shall be compared and discussed based on the experimental findings.
5. Parametric studies, with a special focus on optimisation of the numerical model, will be conducted.

Supervisors: Tore Børvik, Ole Vestrum and Magnus Langseth (NTNU). Håvar Ilstad (Statoil).

The thesis must be written according to current requirements and submitted to the Department of Structural Engineering, NTNU, no later than June 11th, 2017.

NTNU, January 15th, 2017



Tore Børvik
Professor

Acknowledgements

This thesis is written for Structural Impact Laboratory (SIMLab) at Norwegian University of Science and Technology (NTNU). The Structural Impact Laboratory was a Center for Research-based Innovation (CRI) appointed by the Research Council of Norway. After the CRI-SIMLab project ended in 2014, a new project was awarded to the research group resulting in Centre for Advanced Structural Analysis (CASA). The centre aims to build an attractive scientific working environment where fundamental knowledge is created through multidisciplinary theoretical, numerical and experimental research on different scales.

Our supervisors have been Professor Tore Børvik and Professor Magnus Langseth. Their enthusiasm, thoughts and guidance have been much appreciated. They have provided us with the necessary theoretical background and critique.

We want to especially thank our co-supervisor, Ph.D. candidate Ole Vestrum, for his guidance and support. But maybe most of all, we want to thank him for his patience and encouragement.

The experimental work has been carried out with the help of laboratory staff at the Department of Structural Engineering, NTNU. Especially Tore Wisth and Trond Auestad have been of great assistance.

We would also like to thank Dr. Torodd Berstad with the assistance with the computer cluster Snurre, Researcher Egil Fagerholt with the help with Digital Image Correlation (DIC) analyses, Staff Engineer Ole Tore Buset with the assistance with the X-ray computed tomography scanner, and Senior Development Engineer Trond Schjelderup (Shawcor) with the informative tour of their factory in Orkanger.

Furthermore, we wish to thank Postdoc Martin Kristofferesen for valuable guidance in the initiation of this thesis. Also, Håvar Ilstad and Statoil are acknowledged for motivating this project.

Thanks to the all the master students and Ph.D.-candidates at SIMLab for the fun working environment and all constructive discussions.

Trondheim, June 9, 2017



Steffen Hammersvik



Eirik Bugge Kulsrud

Abstract

This thesis is part of an ongoing research program between SIMLab and Statoil about impacts on coated offshore pipelines. Impact loads may occur from objects such as anchors or trawls, causing severe damage to the pipe which may lead to oil or gas production to shut down. The steel pipe had been sufficiently researched concerning the impact event, but much work remained on the coating.

The coating investigated in this thesis was the five layer polymer insulation system, Thermotite, produced by Shawcor (formerly Bredero Shaw). The main focus was to characterise the porous polypropylene layer. Experiments were conducted; X-ray computed tomography to get a look inside the coating and determine the pore morphology by image analyses, and uniaxial compression tests to investigate the mechanical properties.

Image analyses suggested several statistics of the pore structure. The results showed that the morphology is highly inhomogeneous and anisotropic. Furthermore, the relative density was varying between 0.7 to 1.0 depending on the radial coordinate of the pipe. The lowest value was found in the middle. The pore structures on either side, were different (asymmetric morphology). The reason for that was assumed to be the extrusion process during manufacturing. The other directions (hoop and axial) revealed no dependency.

The uniaxial compression tests suggested that the pores affect the strength of the polymer significantly. The different pore structures seemed to have a distinct effect on the force-displacement behaviour. The coating was characterised as a solid with isolated pores, not foam because the transverse expansion was greater than zero and the high relative density. Compression tests on solid polypropylene were employed to establish a material model, calibrated by the use of edge tracing and inverse modelling. The model assumed isotropic hardening and insensitivity to temperature, pressure, and strain rate.

To numerically re-create the test specimens, a direct modelling technique was employed. The method utilises the computed tomography image slices to replicate the samples. A sensitivity study indicated that the accuracy of the models was sensitive to mesh size, friction and the material model properties. Compared to the experimental values, the simulations were satisfactory, but a bit stronger, most likely due to insufficient mesh refinement. However, the models captured the shape of the deformation and the force-displacement curves.

The numerical models were employed to characterise the coating further. The simulations suggested that the reduction in yield force is due to strain localisation between adjacent pores. Simulations of the re-created specimens subjected to tension suggested that the tensile strength is significantly lower than the compressive strength, as the strain gets strongly localised. Mechanical anisotropy (orthotropy) was investigated as well. The results indicated differences throughout the height of the porous layer, and that the coating was weaker when compressed in the radial direction.

A block of porous polypropylene layer was simulated under compression. To re-create the pore structure of the coating satisfactorily, the block needed about one million elements. Therefore, it was assumed that a large-scale simulation of the pipe with the direct modelling technique would require too many elements.

Contents

Acknowledgements	vii
Abstract	ix
Nomenclature	xiii
1 Introduction	1
1.1 Background and motivation	1
1.2 Prior work	3
1.3 Objectives and scope	5
1.4 Outline of thesis	6
2 Theory	7
2.1 Material mechanics	7
2.1.1 Work hardening	7
2.1.2 Viscoplasticity	8
2.1.3 Ductile damage and failure	9
2.1.4 Yield criterion	10
2.2 Arbitrary Lagrangian-Eulerian analysis	12
2.3 Computational tomography	13
2.4 Cellular solids	15
2.5 Image processing	16
2.5.1 Binary image	16
2.5.2 Region properties	17
3 Preliminary Studies	19
3.1 Steel pipe	19
3.1.1 Forming of X65 steel pipes	19
3.1.2 Material parameters	19
3.1.3 Numerical model	21
3.1.4 Results	22
3.2 Coated steel pipe	23
3.2.1 Coating manufacturing process	23
3.2.2 Material parameters	24
3.2.3 Numerical model	25
3.2.4 Results	26
3.3 Summary and discussion	28
4 Experimental work	29
4.1 Measurements	29
4.2 Computer tomography	34
4.2.1 Test setup	34

4.2.2	Results	36
4.3	Uniaxial compression	41
4.3.1	Test setup	41
4.3.2	Results	42
4.4	Summary and discussion	50
5	Porous Polypropylene Characterisation	51
5.1	Initial assumptions and simplifications	51
5.2	Pore morphology	54
5.2.1	Relative density	54
5.2.2	Other characteristics	56
5.2.3	Three dimensional representation of the pores	58
5.3	Characterisation of the specimens	62
5.4	Mechanical properties	66
5.4.1	Polypropylene material model	66
5.4.2	Transverse expansion	71
5.4.3	Compression	73
5.5	Summary and discussion	75
6	Numerical studies	77
6.1	Numerical model	77
6.2	Sensitivity study	81
6.2.1	Mesh size	81
6.2.2	Element type	86
6.2.3	Material model	87
6.2.4	Friction	88
6.2.5	Imperfections	90
6.3	Validation of the direct model	92
6.4	Further characterisation and model capabilities	94
6.4.1	Stress localisation	94
6.4.2	Block	96
6.4.3	Mechanical anisotropy	98
6.4.4	Tension	99
6.5	Summary and discussion	104
7	Concluding remarks	107
7.1	Conclusions	107
7.2	Recommendations for further work	109
	Bibliography	111
A	CT scans	i
B	Calculate mass by the use of relative density	v
C	Python script	vii

Nomenclature

List of Symbols

α	Pressure sensitivity constant (Drucker-Prager)
β	Friction angle (Drucker-Prager)
σ	Stress tensor
ΔL	Incremental length
$\dot{\lambda}$	Plastic parameter
\dot{p}	Equivalent plastic strain rate
\dot{p}_0	Reference (initial) plastic strain rate
λ	Thermal conductivity
ν	Poisson's ratio
ω	Damage variable
ρ	Density
ρ^*	Relative density
ρ_s	Matrix material density (foam)
σ	True stress
σ^*	Stress triaxiality
σ_0, Q_{Ri}, C_{Ri}	Voce hardening rule constants
σ_e	Engineering stress
σ_f	Fracture stress
σ_Y	Yield stress
σ_{eq}	Equivalent stress
σ'_{ij}	Deviatoric stress tensor
σ_{VM}	von Mises stress

σ_{YC}	Yield stress in compression
σ_{YT}	Yield stress in tension
θ_L	Lode angle
ε	True (logarithmic) strain
ε^{pl}	True plastic strain
ε_e	Engineering strain
ε_Y	Yield strain
$\varphi(\boldsymbol{\sigma})$	Equivalent stress function
A	Area
A, B, n	Power law hardening constants
A_0	Initial area
C, m	Rate sensitivity constants in the (Modified) Johnson-Cook model
c_p	Specific heat
D	Specimen diameter
D_1, D_2, D_3, D_4	Johnson-Cook fracture criteria constants
E	Elastic modulus (Young's modulus)
F	Force
f	Yield function
h	Specimen height
I_σ	First invariant
L	Length
L_0	Initial length
M	Mass
P	Pressure
p	Equivalent plastic strain
p_f	Failure strain
T	Temperature
T_m	Melting temperature
T_r	Reference temperature
V	Volume
v	Vertical displacement
W_C, ϕ, γ	Cockcroft-Latham fracture constants

Acronyms

ALE	Arbitrary Lagrangian-Eulerian
BI	Binary image
CCD	Charge-Coupled Device
CPU	Central Processing Unit
DIC	Digital Image Correlation
EFC	External friction coefficient
FBE	Fusion Bonded Epoxy
FC	Friction coefficient
FD	Force-displacement
FEA	Finite element analysis
IFC	Internal friction coefficient
JC	Johnson-Cook
MJC	Modified Johnson-Cook
NFEA	Non-linear finite element analysis
NTNU	Norwegian University of Science and Technology
PEEQ	Equivalent plastic strain
PP	Polypropylene
RAM	Random Access Memory
RD	Relative density
SEM	Scanning Electron Microscope
SIMLab	Structural Impact Laboratory
STD	Standard deviation

Introduction

1.1 Background and motivation

After an inspection of the gas pipeline from Kvitebjørn in the North Sea to the Kollsnes gas plant in November 2007, Statoil discovered that the pipe had been impacted by an anchor and dragged out of its initial position [1] (Fig. 1.1). Production was shut down, but resumed quickly after the pipeline's mechanical integrity was sufficiently evaluated. A permanent repair was planned in 2009, but unfortunately, a small gas leak was found after a routine inspection in 2008 [2]. Obviously, the production was immediately shut down - at a significant cost. At that time, it was clear that damage evaluation method was important and insufficient in the current state. The pipelines are used to transport an enormous amount of oil and gas over vast distances. Therefore, accidents such as the one at Kvitebjørn, and many others [3], could lead to environmental damage and massive economic losses.



Figure 1.1: A pipeline impacted by an anchor [4].

A research collaboration between Structural Impact Laboratory (SIMLab) at NTNU and Statoil was established. The collaboration resulted in many master's theses [5, 6, 7, 8, 9, 10, 11], a PhD thesis by M. Kristoffersen [4], and several ongoing projects [12] at the time of writing this thesis. A lot of the previous work was focused on the impact event and the steel pipe (X65). Characterisation of the steel through material tests, experiments on the impact event and the steel's fracture mechanisms with metallurgical investigations, and successful simulations of these experiments have been conducted, giving a good understanding of the behaviour of steel pipe.

The pipelines used in the offshore oil and gas transportation systems, are coated with a thermal insulator. The coating is a multilayer polymer [13], where at least one layer is a porous polypropylene (PP) called BA202E [14], which is used to keep the oil (or gas) at a high temperature so that it flows fast and clotting of the pipe is avoided. The integrity of the pipeline is measured by the state of the steel - if the steel pipe has a certain amount of damage the production must shut down. So how do the polymer coating help regarding an impact event? How does the porous polypropylene work as an energy absorbent? Since the steel pipe had been sufficiently researched, while inadequate investigation had been done on the coating, it was a natural focus point for this thesis.

1.2 Prior work

In the following, the previously conducted work related to the research on the impact against offshore pipelines is presented. A lot of work have been put into the impact event and how steel pipes behave under such conditions. The PhD thesis [4] offers great material tests of the steel (X65) and calibrated material models, as well as several component (pipe) tests (bending and then stretching, which simulate the impact event), both quasi-static and dynamic. The steel was characterised as isotropic, homogeneous and strain rate sensitive. The temperature was not taken into account (isothermal conditions).

Fracture mechanisms were investigated, and failure criteria were established. It was found that while the strain rate increased, and therefore the flow stress, the fracture strain remained unaltered. However, the fracture strain was sensitive to stress triaxiality. In the three-point bending tests (Fig. 1.2), there were no observations of fracture on the quasi-static tests, but always after the springback (stretching), which indicates that the springback is the critical part. Water-filled pipes were tested as well. It resulted in a stronger response when the pipe was closed off, but no change when the top end was open.



Figure 1.2: Setup of quasi-static three-point bending test conducted by M. Kristofferesen [4].

Metallurgical studies showed that the primary fracture mechanism is ductile, with nucleation, void growth and coalescence in tension. A ductile to brittle transition of fracture can arise. This happens when the material is subjected to high compression before tension. In the simulations, the numerical models were great at simulating the response, but fracture was not sufficiently characterised. The commonly employed fracture criteria do not account for the effect of compression before tension.

In the master's thesis by Holm and Røshol [11], component tests (bending) were conducted on coated steel pipes. Simple material tests on the porous polypropylene coating were done, but the calibrated material models were not sufficient to simulate the experiments. Also, the numerical models had problems with distortion control of the coating. The coating is much thicker and weaker than the steel pipe. This combination leads to large displacements in the coating which causes numerical

errors due to severe distortion of the elements.

Furthermore, there have been conducted several studies on porous polymers in an attempt to characterise the structure and morphology of the pores. In [15], a piece of a coating was cut into very thin slices and photographed. The images were used to find statistics of the morphology. The study showed that the pore structure was quite complex; the morphology is highly anisotropic and inhomogeneous. In [16], further characterization was made. Hegdal et al. defined the porous polymer as a "high-density foam". They reconstructed the coating, and simulated the thermal conductivity. The result was in agreement with their measurements. It was established that thermal conductivity is dependent on morphology.

A study to determine some of the material properties of the porous polypropylene was done in [12]. X-ray computed tomography was used to investigate the interior of a sample column, and several specimens were extracted and subjected to compression tests. The results indicated that the mechanical behaviour is anisotropic (inhomogeneous pore morphology) and strain rate sensitive. Component tests were conducted on the coated steel pipe - both quasi-static and dynamic. Dynamic tests showed little to no difference from the quasi-static tests. The coated pipes were stiffer than the uncoated.

1.3 Objectives and scope

The natural focus of this thesis was the coating solution of the pipeline, with a primary goal to come one step closer to properly simulate the coated steel pipe. To adequately describe the mechanical behaviour of the coating, an extensive investigation must be conducted. In this thesis, the main objective of the research project is broken into smaller pieces, and the following objectives will be considered:

- Perform experimental tests, such as uniaxial compression and X-ray computed tomography, on the porous polymer coating.
- Characterise the porous polypropylene layer of the coating solution for a deeper understanding of the mechanical behaviour of the material.
- Calibrate a material model for the solid polypropylene.
- Create numerical models of the coating using a direct modelling technique, and X-ray computed tomography. Validate the models with the experimental findings.

The following points presents the simplifications made by choosing small and detailed objectives. Also, the limitations of accomplishing these goals are included.

- The experimental work will be compression tests conducted quasi-statically at room temperature in one direction of the coating (radial). Any material model calibrated will therefore exclude temperature, anisotropy or strain rate effects.
- Pressuresensitivity of the material will not be conducted any experiments on, but a Drucker-Prager material model will be calibrated based on the tensile properties found in the litterature.
- Numerical simulations are restricted to what is available at SIMLab. Abaqus and Matlab was chosen to do the simulations and analyses.
- There are several different coating solutions to investigate. In this thesis, the work is limited to Thermotite.
- No analytic estimations of the impact event will be conducted.

1.4 Outline of thesis

The chapters have been set up thematically. Each chapter's background information is presented in the chapters before. They can be read separately, and cross-references are included where needed. What follows is a brief outline of the thesis.

Chapter 2 is the theory used in this thesis. Information about material mechanics, adaptive meshing, cellular solids, computed tomography, and image processing is found here.

Chapter 3 presents the preliminary studies. One study for the uncoated steel pipe and another for the coated steel pipe was conducted. The studies were using pre-calibrated material models to simulate experiments not conducted in this thesis.

Chapter 4 contains the experimental work done in this thesis. X-ray computer tomography (CT) was used to scan the coating solution, and uniaxial compression tests were conducted on solid and porous polypropylene.

Chapter 5 is where the characterisation of the porous PP was performed. The computed tomography image slices was used to generate statistics of the pore morphology and a material model was calibrated.

Chapter 6 presents the numerical studies. CT image slices of specimens were used to build direct models (mesh) of the specimens in Abaqus. A sensitivity study was carried out. The models were compared to the experimental findings.

Chapter 7 is the end of this thesis. Here conclusions and recommendations for further work are presented.

Theory

The theory used in this thesis is presented in this chapter. Basic knowledge of mechanics, materials and finite element analysis (FEA) is assumed known by the reader.

2.1 Material mechanics

Material mechanics is important when studying the impact on coated steel pipes. The following is the basis the reader should know to understand the work done in this thesis. The theory stated here is found in the compendiums by Hopperstad and Børvik [17, 18].

2.1.1 Work hardening

Typically, the material increases in strength when plastically loaded. That is denoted work-hardening. To describe the evolution in yield surface the yield function

$$f(\boldsymbol{\sigma}) = \varphi(\boldsymbol{\sigma}) - \sigma_Y = 0, \quad (2.1)$$

where $\varphi(\boldsymbol{\sigma})$ is equal to the equivalent stress, σ_{eq} , and σ_Y is the yield stress, is added the chosen hardening rule. The most common rules are the isotropic hardening and the kinematic hardening. Isotropic hardening means that the yield surface expands equally in all stress directions. The yield stress is now a variable depending on the equivalent plastic strain, $p = \int \dot{p}$, which is defined as the energy conjugate variable to the equivalent stress. For associated flow rule the equivalent plastic strain rate equals the plastic parameter ($\dot{p} = \dot{\lambda}$).

In the following two isotropic hardening rules will be considered. The power law describes the hardening with a power function, i.e.

$$\sigma_Y(p) = A + Bp^n \quad (2.2)$$

where A, B, n are material constants found from physical tests. This rule is simple but effective at describing the hardening for many different materials. The other rule, Voce hardening rule, is more accurate, but uses more material constants, i.e.

$$\sigma_Y(p) = \sigma_0 + \sum_{i=1}^k Q_{Ri}(1 - \exp(-C_{Ri}p)) \quad (2.3)$$

where σ_0, Q_{Ri}, C_{Ri} are material constants. The accuracy increases as k increases but at the same time the number of constants increases. $k = 2$ is usually sufficient.

2.1.2 Viscoplasticity

Viscoplasticity takes rate-sensitivity into account. Phenomena like creep and stress relaxation can now be described by the material model. Also, elevated strain rate effects which are important in structural impact. In the theory of plasticity the development of plastic strain takes place at the yield surface, but in viscoplasticity, the development happens outside the yield surface. The distance from the surface is equivalent to the strain rate. This way the flow stress increases with increasing plastic strain rate. Two models in the theory of viscoplasticity are presented below. These models also account for temperature (thermo-viscoplastic models).

The Johnson-Cook model is valid for isotropic materials. Here the power law is used as the hardening rule. The equivalent stress is given as

$$\sigma_{eq} = (A + Bp^n)(1 + C \ln \dot{p}^*)(1 - T^{*m}) \quad \text{for } f > 0 \quad (2.4)$$

where $\dot{p}^* = \dot{p}/\dot{p}_0$ and $T^* = (T - T_r)/(T_m - T_r)$. A, B, n are constants describing the isotropic hardening, C, \dot{p}_0 are parameters describing the rate sensitivity, and T_r, T_m, m are parameters describing the temperature effects. T is the temperature, T_m is the melting temperature, and T_r is the reference temperature (room temperature). \dot{p} is the plastic strain rate. This model may cause numerical problems when implemented in a finite element simulation. The strain rate term approaches infinity when the plastic strain rate approaches zero. The modified Johnson-Cook fixes this problem, i.e.

$$\sigma_{eq} = (A + Bp^n)(1 + \dot{p}^*)^C(1 - T^{*m}) \quad \text{for } f > 0 \quad (2.5)$$

Note that these models reduce to basic plasticity when the rate and temperature constants (C and m) are set to zero. If temperature effects are not of interest in the modelling of the material the temperature term should be neglected.

2.1.3 Ductile damage and failure

In the description of the material behaviour, the failure mechanics are important. To simulate fracture in a component a failure model is needed. There are many different types, but ductile damage and failure will be discussed herein.

There are two types of ductile damage; uncoupled and coupled damage models. Coupled models affect the elastic-(visco)plastic response, and if the damage evolution exceeds the hardening, strain softening will occur. Uncoupled models do not affect the response. The failure criteria depend on the damage variable and its associated evolution rule, which is a function of stress and plastic strain.

Ductile damage and fracture are described by three mechanisms: nucleation (the initiation of voids), void growth, and coalescence of voids. Nucleation happens when the stress on a particle is sufficient to induce particle cracking or particle-matrix decohesion (Fig. 2.1). Coalescence occurs by localised plastic deformation of the matrix material between adjacent voids. The ductile damage and failure criteria depend on the stress triaxiality and Lode parameter.

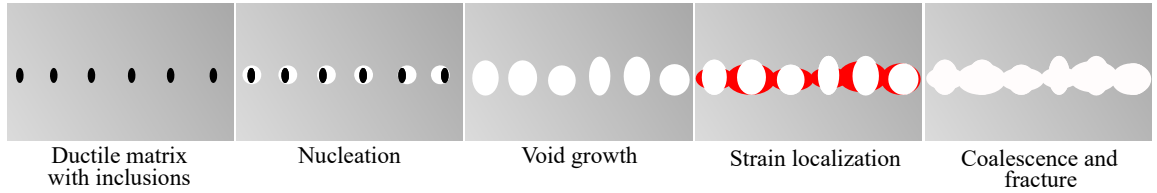


Figure 2.1: Illustration of ductile damage and failure. The ductile material consists of a ductile matrix with inclusions (bigger particles).

In the following, the uncoupled damage evolution rule is considered. Here, a failure surface is assumed to exist. This surface defines the failure strain p_f , and is a function of stress triaxiality σ^* and Lode angle θ_L . The damage variable ω is defined as

$$\omega = \int_0^p \frac{dp}{p_f(\sigma^*, \theta_L)} \quad (2.6)$$

The criteria state that when the damage variable reaches $\omega=1$, fracture occurs. There are several descriptions of the failure surface, resulting in different failure criteria. The simplest is the constant failure strain, i.e.

$$\omega = \frac{1}{p_f} \int_0^p dp \quad (2.7)$$

There exist several ductile damage accumulation rules, one of which is the Johnson-Cook fracture model. Here the Lode angle is neglected. The model is governed by Equation 2.8, where D_1, D_2, D_3, D_4 and D_5 are model constants.

$$p_f(\sigma^*, \dot{p}, T) = [D_1 + D_2 \exp(D_3 \sigma^*)] (1 + D_4 \ln \dot{p}^*) (1 + D_5 T^*) \quad (2.8)$$

Another fracture model is the extended Cockcroft-Latham (CL) criterion where the damage evolution rule is given as

$$\omega = \frac{1}{W_C} \int_0^p \left\langle \phi \frac{\sigma_I}{\sigma_{VM}} + (1 - \phi) \left(\frac{\sigma_I - \sigma_{III}}{\sigma_{VM}} \right) \right\rangle^\gamma \sigma_{VM} dp \quad (2.9)$$

where W_C , ϕ and γ are model constants. Note that the standard CL criterion is obtained by setting $\phi = \gamma = 1$.

2.1.4 Yield criterion

When choosing a yield criterion for a material, there are several things to consider. Is the material behaviour pressure-sensitive? Is it isotropic or anisotropic? There are many different criteria to choose from. Tresca, von Mises and Hershey criteria are very common and assume isotropic and pressure-insensitivity (metals). Hill yield criterion is frequently used for orthotropic (three perpendicular planes of symmetry) materials, and for pressure-sensitive materials (some metals, concrete, polymers) Mohr-Coulomb, Drucker-Prager and Deshpande-Fleck are used. Herein, two of these models are presented. See [17, 18] for more information regarding the yield criteria.

von Mises

The von Mises yield criterion is frequently used in materials such as metals. The assumptions in this criterion are isotropy (same material properties in all directions) and pressure insensitivity. The yield function becomes

$$f(\boldsymbol{\sigma}) = \sqrt{\frac{3}{2} \sigma'_{ij} \sigma'_{ij}} - \sigma_Y \quad (2.10)$$

where σ'_{ij} is the deviatoric stress tensor. To calibrate this criterion only a uniaxial material test is necessary.

Drucker-Prager

A yield criterion for isotropic and pressure-sensitive materials is the Drucker-Prager criterion. It is used with materials such as concrete, soils, rocks and polymers, and is formulated mathematically as

$$f(\boldsymbol{\sigma}) = \frac{\sqrt{\frac{3}{2} \sigma_{ij} \sigma_{kl}} + \alpha I_\sigma}{1 + \alpha} - \sigma_Y \quad (2.11)$$

where α is the pressure sensitivity of the material, and $I_\sigma = \sigma_{kk} = -3P$ is the first invariant, where P is

the pressure. Note that the criterion reduces to the von Mises criterion when the pressure sensitivity is equal to zero.

There are several different versions (modifications) to this criterion, such as the hyperbolic and exponent form, but the one used in this thesis and illustrated by Figure 2.2, is the linear Drucker-Prager criterion.

The curve is linear so only two constants are needed to describe it. These constants are the pressure sensitivity and the yield stress in tension or compression. In Abaqus the friction angle, β , is used instead of the pressure sensitivity constant, α . This value is calculated with the following equation,

$$\tan(\beta) = 3\alpha = 3 \frac{\sigma_{YC} - \sigma_{YT}}{\sigma_{YC} + \sigma_{YT}} \quad (2.12)$$

where subscripts C and T refer to compression and tension, respectively.

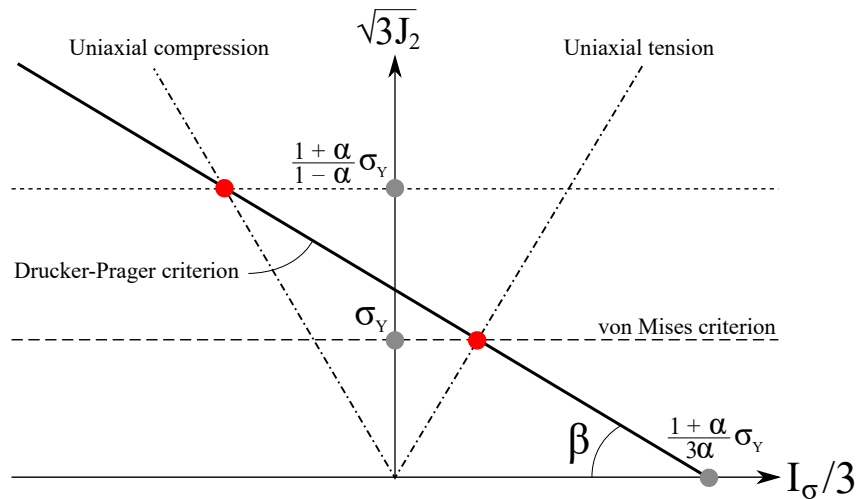


Figure 2.2: Illustration of linear Drucker-Prager yield criterion. β is the friction angle (used in Abaqus). $\sqrt{3J_2}$ is the von Mises stress.

2.2 Arbitrary Lagrangian-Eulerian analysis

Here an important aspect of the finite element method (FEM) theory is presented. However, it is assumed that the reader knows the fundamental equations FEM are built on, as well as non-linear finite element methods. For more information see [19, 20, 21].

In many nonlinear simulations, the material in the structure undergoes large deformations. These deformations may end up in distorting the element mesh, in such a manner that the mesh is unable to provide accurate results, or that the simulation terminates due to too large distortions. In these simulations, there is a need for an adaptive mesh tool to periodically minimise the distortion in the mesh. If the adaptive meshing formulation is restricted to the parts that undergo significant deformation the technique will also be very cost effective as the improved mesh quality will increase increment size, and thereby make up for added cost of the adaptive mesh increments.

An adaptive mesh tool that is applicable in Abaqus is Arbitrary Lagrangian-Eulerian (ALE) analysis. ALE combines the Lagrangian formulation with the Eulerian formulation. In the Lagrangian formulation, each node of the computational domain moves exactly with the material points throughout the simulation. That enables the user to keep track of how the structure deforms during loading and is, therefore, the most used formulation in solid mechanics. In the Eulerian formulation, on the other hand, the nodes stay fixed while the material flows through the mesh. That makes large displacements in the material easier to handle as the mesh is fixed and will therefore not experience mesh distortion. In the ALE, the advantages of both formulations are combined to reduce distortion. The mesh motion will be constrained only by free boundaries, but are otherwise the material nodes, and mesh nodes can be moved arbitrarily from each other to accommodate rezoning needs and avoid mesh enlargement. A simplified illustration of how the different formulation can be seen in Figure 2.3.

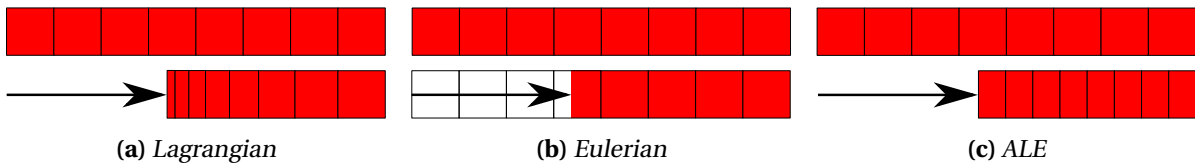


Figure 2.3: Motion of mesh and material with various methods [22].

2.3 Computational tomography

In material science and engineering, the method of computational tomography (CT) is very attractive. What follows is a brief explanation of how it works and how it is used. For more information see [23].

Different kinds of image techniques are popular in material science, such as scanning electron microscope (SEM). These methods often require the object to be cut, i.e. the internal parts of the object cannot be analysed without cutting it open. X-ray tomography, on the other hand, is an excellent way to create a 3D representation of an object - with information about its inner parts, without destroying the object in any way.

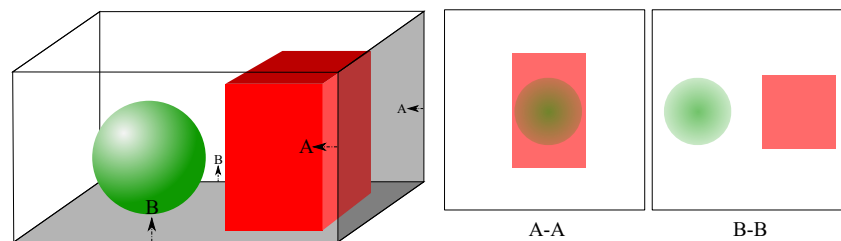


Figure 2.4: A sphere and a rectangular cube (both the same material and density) is scanned at two different sections (A and B) by a penetrating wave. Notice the transparency in the sections; high transparency means little to no matter, and low transparency means much matter. Note that in section A-A the sphere absorbs photons so that the projected circle is present (cube do not absorb all photons).

A 3D model of an object can be constructed using tomography. It means that several images are taken by some penetrating wave (X-rays) in sections. The sectioning happens by rotating the object. The model is then created by a tomography reconstruction algorithm (often called the filtered back-projection algorithm). An example of two sections is illustrated in Figure 2.4.

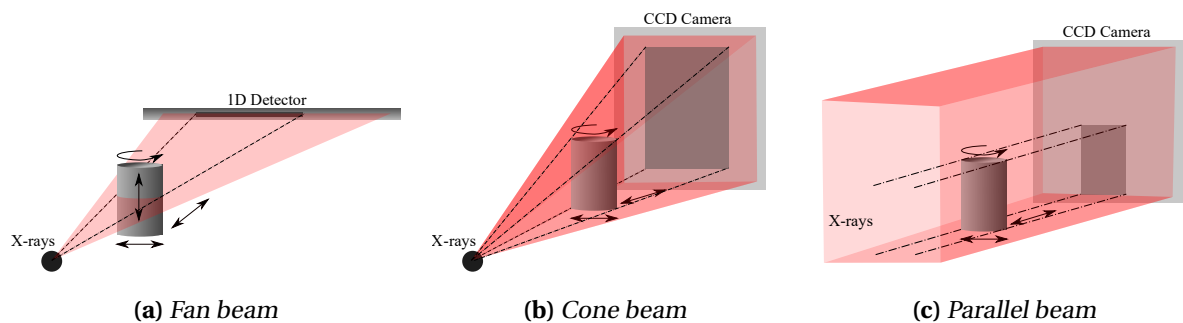


Figure 2.5: Different types of X-ray scanning. The fan beam and 1D detector demand vertical movement of the object to be scanned, while the other two types do not. The object must rotate for every setup so that the CT scan can be complete.

In X-ray tomography the penetrating wave is X-rays. The process of taking each image is called radiography. Here a beam is sent towards an object to be scanned, and the transmitted beam is captured at a detector, often a charge-coupled device (CCD) [24]. It can be shown that the ratio of the number of transmitted to incident photons is related to the density of the material, by the use of Beer-Lambert's law and an empirical law. In general, this means that the higher densities in the object absorb more

photons, resulting in fewer hitting the detector. The detector creates an image (projection) based on the number of transmitted photons, where the brighter parts of the image are the higher densities.

To capture the images used in the computational recreation of the object to be scanned, the X-rays are produced and captured differently depending on the method chosen. Most commonly there are three methods, illustrated in Figure 2.5. Note that the fan and cone beam are results of X-ray tubes, and this gives the enlargement in the detector. With parallel beams, the object is captured at the real size. By moving the sample between the source and detector, the resolution can be adjusted (for fan and cone beams).

The cone beam setup is common in X-ray computed tomography, but there is an issue when reconstructing the object. See Figure 2.6 for an illustration of the problem. The reconstruction algorithm must account for the angle of the X-ray waves hitting the detector, which results in fewer hitting it in the periphery. The digital rebuilding of the object may, therefore, be prone to error at the edges. Today's algorithms are well formulated and handle the issue, but the image slices in those regions may still be affected.

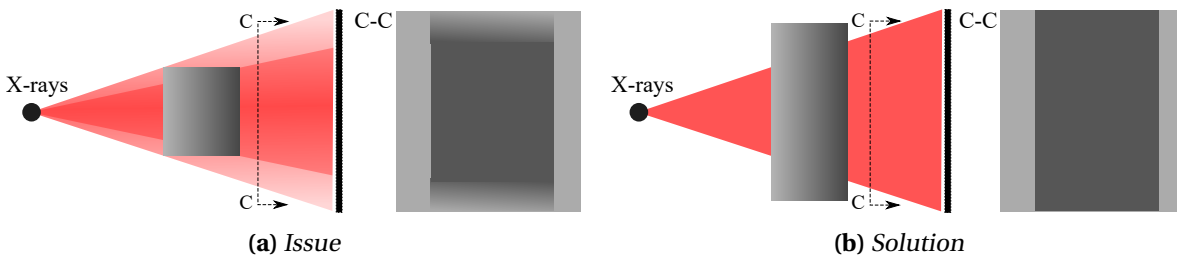


Figure 2.6: Cone beam issue and solution.

When working with computer tomography, there may occur artefacts [25]. They can severely degrade the quality of the images. These bright spots on the images often arise from the image reconstruction process. Artefacts could also be unexpected objects such as metals within the body to be scanned, which results in a higher brightness in that part of the images.

2.4 Cellular solids

A cellular solid is a network of solid struts or plates which form the edges and faces of cells [26]. The relative density (or porosity), ρ^* , of a cellular solid is an important property. It is given as

$$\rho^* = \rho / \rho_s \quad (2.13)$$

where ρ is the foam material density and ρ_s is the density of the walls (matrix material).

Foams are true cellular solids and have a relative density (RD) of less than 0.3 [26]. A porosity larger than this is considered a solid containing isolated pores. Another important characteristic of foam is that the retraction coefficient (Poisson's ratio) is close to zero [27]. The value may be lower than 0.05 - even negative [28]! During compression of foam the ratio is normal (same as matrix material), but in the vicinity of yielding the walls start to buckle, and thus the retraction coefficient reduces to almost zero.

In general, the behaviour of elastic-plastic foams under compression involves linear elasticity, a plateau where the matrix material plastically yields, and densification. The steps are illustrated in Figure 2.7. Densification is the regime where the stress rises steeply.

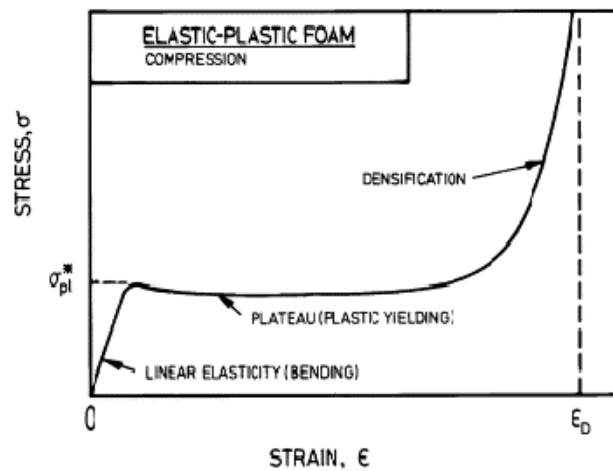


Figure 2.7: Stress-strain relationship for elastic plastic foams in compression [26].

2.5 Image processing

Digital image processing is the processing of images using mathematical operations. The output may be either an image or a set of characteristics or parameters related to the original image. In the following two essential image processing tools are presented - binarization and region properties.

2.5.1 Binary image

A binary image (BI) consists of only two colours - black and white (0 and 1). Here the ones are the on-pixels, and the zeros are the off-pixels. The transformation process from grayscale to a binary image is called binarization. A grayscale image has many different possible pixel values (grey levels), depending on the number of bits to represent the pixel. A threshold level is necessary to determine the line between the on- and off-pixels. Every pixel with the grayscale value below this threshold value is set to 0, and the pixels above the threshold value are set to 1. This threshold value can be adjusted by the user, but an already implemented algorithm in Matlab, called Otsu's method [29], is recommended due to its accuracy of determining the desired binarization.

In Figure 2.8 the binarization process is illustrated. The original image is a grayscale image of some coins (included in Matlab). The histogram shows how many pixels have a certain grey level. The first red line (grey level 100) is the threshold level used to get the binary image shown in Fig. 2.8c, and the other line (grey level 180) resulted in the BI shown in Fig. 2.8d. The first BI is the sought result because with this image the properties of the coins can easily be found by using region properties.

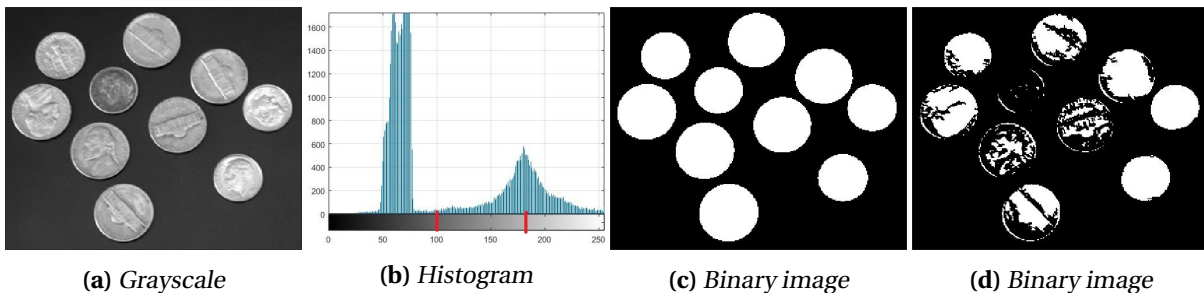


Figure 2.8: The process of binarization. A grayscale image (a) has a histogram (b). A threshold level is chosen (red lines), and the image pixels are set to 0 if below and 1 if over this value. BI (c) used the first threshold level (100), and BI (d) used the other (180).

2.5.2 Region properties

From a binary image, a labelled image can be created in Matlab. The algorithm produces labels at every separate part in the image and counts them. Each part is defined by connecting on-pixels and given a number as the label. See Figure 2.9 for a simple illustration of the process.

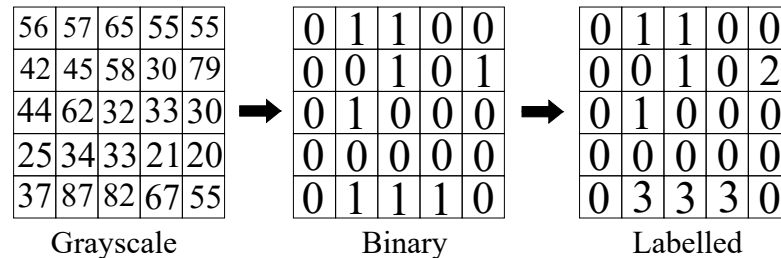


Figure 2.9: Illustration of a 5x5 pixel grayscale image transformed into a binary image with the threshold grayscale value set to 57, and the labelled image.

The labelled image can be used to find many different properties, such as the pixel area, bounding box, major and minor axis length, orientation, etc. of each labelled part in the image. That is called region properties. Matlab has a function to find all these properties [30]. In Figure 2.10 the results of a region properties analysis is shown.

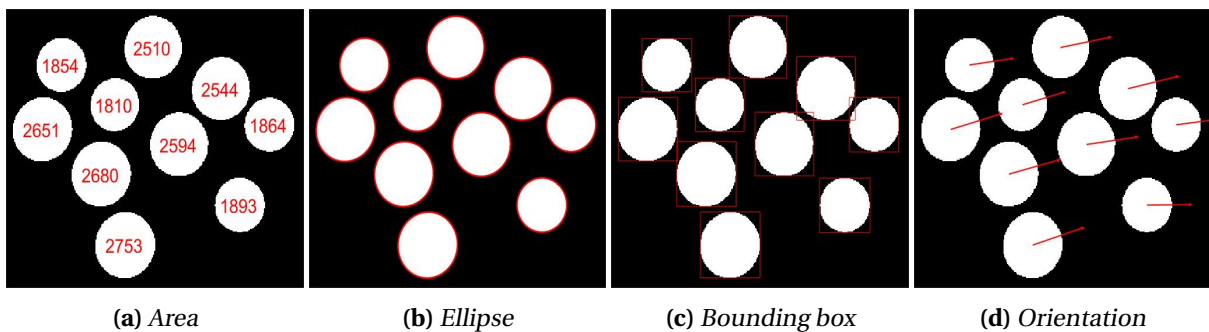


Figure 2.10: Results of a region properties analysis of the binary image from Figure 2.8c. In (a) the numbers represent the amount of on-pixels in the region (area). Figures (b) and (c) show the ellipses and bounding boxes fitted to the regions, respectively. (d) shows the orientation of the region. Note that the horizontal direction in the image is the origin angle (0 degrees).

Preliminary Studies

In the introduction of this thesis, the prior work on the coated and uncoated X65 steel pipe was presented. It was clear that the steel pipe had been significantly more researched than the coating. The research resulted in material models, which was employed to simulate the component (pipe) tests - both coated and uncoated. All experiments and simulations are conducted quasi-statically in this thesis, as the dynamic effects are not within the scope. The preliminary studies were carried out to illustrate that the coating needs further research.

3.1 Steel pipe

As the steel pipe is essential for the mechanical response of the whole pipe, it is important to understand this behaviour before moving on to the combined performance of coating and steel.

3.1.1 Forming of X65 steel pipes

The X65 steel pipe analysed herein are made seamless, i.e. without welding. A rough description of the process to form a smooth pipe is as follows: A heated solid cylinder is placed between two rollers which apply radial compression to the cylinder. The compression gives rise to stresses that cause the centre of the cylinder to fracture and cavity forms along the cylinder's longitudinal axis. This is known as the Mannesmann effect [31]. The cylinder is then pierced by a plug, which forms it into a pipe. The shell is further worked to establish specified diameter and thickness. An illustration of the process is shown in Fig. 3.1.

3.1.2 Material parameters

The doctoral thesis by M. Kristoffersen [4] showed good results when recreating the mechanical behaviour during impacts on steel pipes. To describe the mechanical behaviour numerically, Kristof-

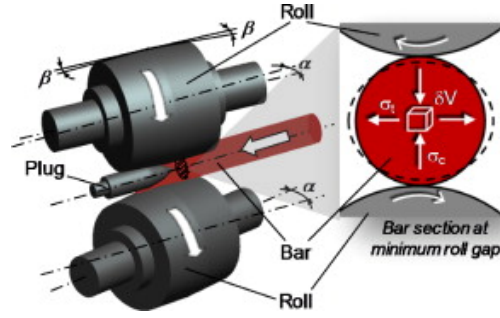


Figure 3.1: Illustration of the Mannesmann process [31].

fersen proposed a material model assuming isotropic hardening, which is described by Johnson-Cook (JC). See Section 2.1.2 for more information about the thermo-viscoplastic models and the associated equations. The parameters for the material model are presented in Table 3.1. Note that as isothermal conditions are assumed, parameters concerning thermal softening is set to zero.

In addition to the elastic and thermo-viscoplastic behaviour, Kristoffersen calibrated fracture criteria for the steel; the Extended Cockcroft-Latham (ECL), and two based on the Johnson-Cook fracture criteria (Sec. 2.1.3). Constants for the three fracture criteria are presented in Table 3.1. Herein, the ECL criterion is adopted in the simulations. However, neither of the experiments on the component forced the steel part of the pipes to fracture (the springback gave rise to fracture and cracks). Also, as Kristoffersen discussed, a very fine mesh is required to describe the local strain field, as fracture initiates at scales much smaller than the size of the elements typically used in global simulations. Therefore, a fracture criterion may not be necessary.

Table 3.1: Constants for material model and fracture criteria, gathered from [4]

Elasticity and density					
E [MPa]		ν [-]	ρ [kg/m ³]		
208 000		0.3	7800		
Johnson-Cook model					
A [MPa]	B [MPa]	n [-]	C [-]	$\dot{\rho}_0$ [1/s]	
465.5	410.8	0.4793	0.0104	$8.06 \cdot 10^{-4}$	
ECL fracture criterion					
W_C [MPa]		ϕ [-]	γ [-]		
1562		1	1		
Johnson-Cook fracture criteria					
CL-based	D_1	D_2	D_3	D_4	$\dot{\rho}_0$
	0.70	1.79	1.21	-0.00239	$8.06 \cdot 10^{-4}$
Test-based	D_1	D_2	D_3	D_4	$\dot{\rho}_0$
	0.42	2.25	1.87	-0.00239	$8.06 \cdot 10^{-4}$

3.1.3 Numerical model

To verify the material model adopted from M. Kristoffersen a numerical model was established to recreate the quasi-static component test conducted in [11] and [32]. Here pipes were placed on a rigid steel base and kept in place by wooden supports. An indenter was set to hit the pipe in the middle, and measurements were taken for both outer and inner displacement. The indenter was loaded and unloaded with increments of 300 kN. In the quasi-static component test, two different pipe dimension were tested, one large and one small. In this thesis, only the small pipe is considered, as the tests conducted herein only have been carried out on samples from the coating on this pipe. The small steel pipe has an internal diameter of 244.50 mm and a wall thickness of 14.30 mm.

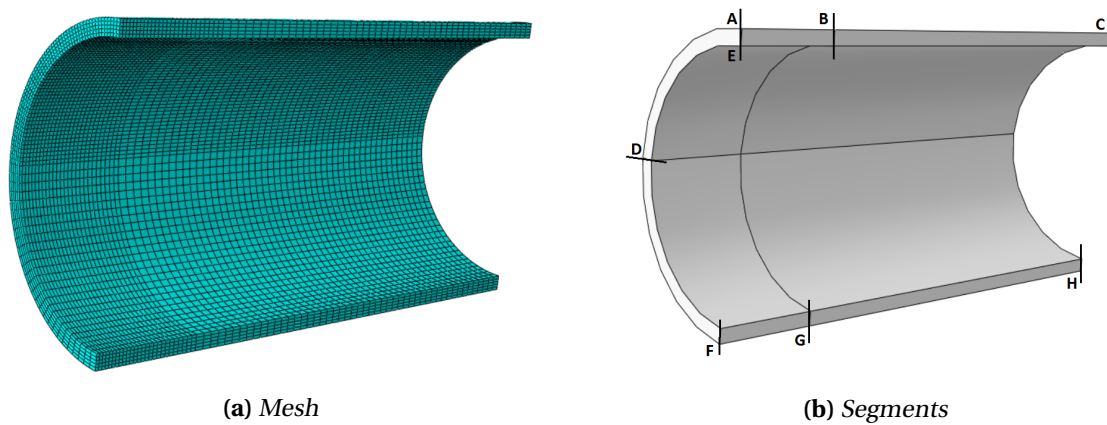


Figure 3.2: Illustration of the model of the pipe in Abaqus.

Table 3.2: Mesh information of the steel pipe.

Segment	Segment size	# of elements	Uniform or bias
AB/FG	100 mm	26	Bais(3mm - 5mm)
BC/GH	400 mm	50	Uniform
AD	90 °	54	Uniform
DF	90 °	27	Uniform
AE	14.3 mm	5	Uniform

The numerical model established in [11] was used as inspiration when creating the model, but some alterations were made when creating the mesh. An assumption of symmetrical deformation was made to reduce computational time by only creating a quarter of the pipe. The pipe was established with standard reduced integration elements (C3D8R) and divided into segments in order to create a diverse mesh throughout the part. The elements close to, or directly in contact to, the indenter will suffer most deformation and are therefore made smaller than other elements. Some deformation will also happen in the bottom of the pipe, but not so large that there was any need for a mesh refinement. Illustration of the meshed steel pipe is presented in Figure 3.2, and more detailed information can be found in Table 3.2.

The indenter and the fixed base (bottom surface to restrain the pipe from moving downwards) was created as analytical rigid. As the pipe experienced large deformations due to contact, Abaqus/Explicit was used [20]. The time step was set to 0.05 seconds with a ramp amplitude of 0.005 seconds to avoid unwanted dynamic effects at impact between the indenter and the steel pipe. The interaction

between the parts was established by general contact, all with self, with default interaction properties for normal and tangential behaviour. The numerical setup can be seen in Fig. 3.3.

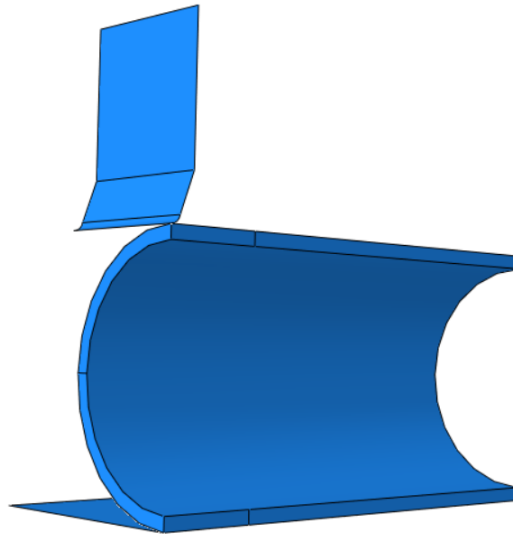


Figure 3.3: Numerical simulation setup.

3.1.4 Results

The results of the quasi-static simulations on the X65 steel pipe is presented in Figure 3.4. The numerical models captured the expected deformation mode of the pipe, and the force-displacement (FD) curves coincide well with the experimental data for both outer and inner displacement. In Figure 3.4b the experimental values stop after a displacement of about 50 mm, this is because the tool used to measure internal displacement needed to be removed to avoid damage by the dent. In Fig. 3.4a the simulation show a slightly reduced force compared to the experiment after 50mm, but the result still gives confidence to the accuracy of the numerical model.

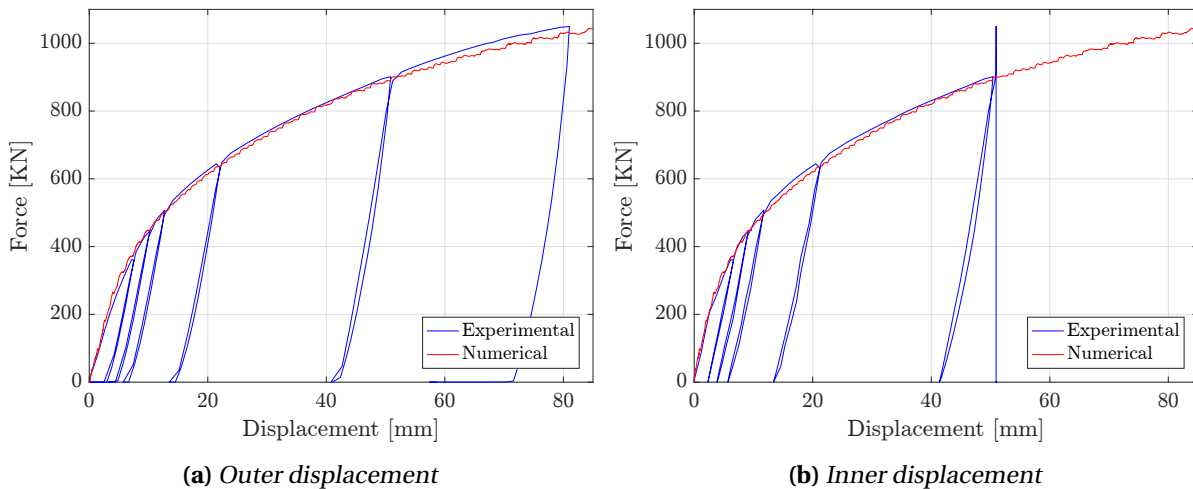


Figure 3.4: Force - displacement curves from the simulation and experiment of the steel pipe.

3.2 Coated steel pipe

Unlike the X65 steel, the coating of the pipes has not been thoroughly investigated. The previous master theses [5, 6, 7, 8, 9, 10] have considered the steel pipe exclusively, and only the thesis by Holm and Røshol [11] have studied the coating. The coating applied to the pipe that is studied herein is created by Shawcor, (formerly Bredero Shaw) and a guided tour of their factory at Orkanger, Norway, was made as an initiation of this master thesis. Senior Development Engineer at Shawcor, Trond Schjelderup, was the guide. He gave valuable insight into the different processes involved. The following information of the coating presented in this section is gathered from their website [33] and the factory visit.

3.2.1 Coating manufacturing process

The coating applied to the pipes is an advanced multi-layer polypropylene insulation solution called Thermotite[®] [13]. The solution may contain repeating layers depending on the use of the pipe. Note that the small pipe with a five-layer coating is the one considered in this thesis. The primary purpose of the coating is to provide thermal insulation for heated liquids to assure flow through the pipe. The coating can withstand temperatures between -37°C and 150°C , and it can operate at a water depth 700m. The coating has also been tested extensively considering physical properties and has performed great when being subjected to external forces.

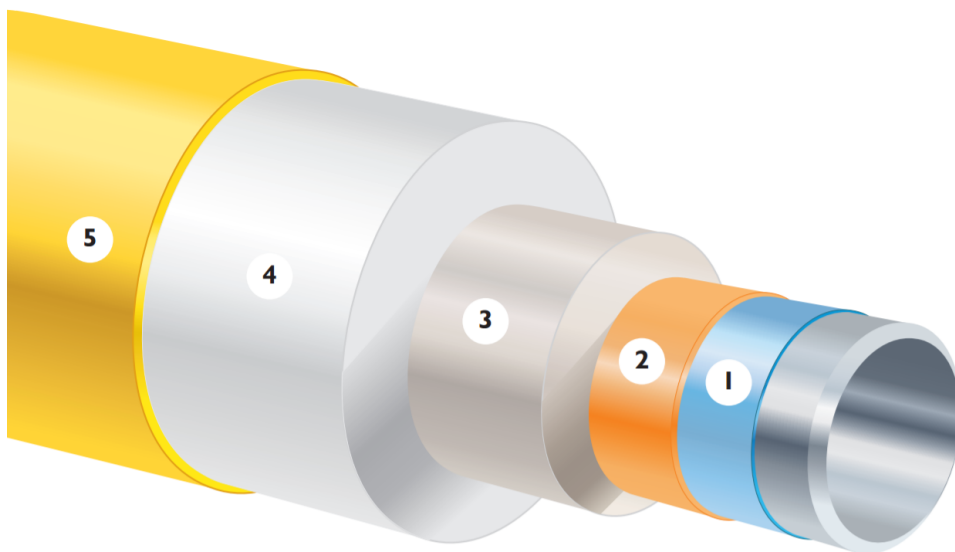


Figure 3.5: Illustration of the multi-layer coating [13]. The layers are fusion bonded epoxy (1), adhesive (2), solid PP (3), porous PP insulation (4), and outer shield (5). Note that the colours may be different in the physical product.

The multi-layer geometry consists of five different layers with specific thermal and mechanical properties which is placed at various locations to optimise the performance of the coating. The composition of the layers is illustrated in Fig. 3.5. As the figure shows, the fourth layer, porous polypropylene, is by far the largest part of the coating. The porosity of this layer is created by introducing gas bubbles into heated polymer. The bubbles are introduced by inserting a chemical blowing agent into the polymer which injects gases into the polymer at high pressure. The gas will expand into bubbles when

lowering the pressure. This introduction of pores gives the polymer excellent thermal characteristics, as seen in Table 5.2. A more thoroughly description of how the pores are induced to the coating can be found in the article by Tofteberg et al. [15]. Note that the manufacturing process may differ, but it was assumed that the method of creating pores was unchanged.

In Figure 3.6, an illustration of the process to apply the coating to the pipe is shown. The manufacturing process consists of three steps, each with an own production line. At the first step, the steel pipes are preheated and cleaned from corrosion by abrasive blasting. Further, the pipe’s surface is fixed for deflections, before the pipe is declared ready for coating by a visual inspection. At the second step, the pipes are heated to 220-230°C to make layer 1, fusion bonded epoxy (FBE) powder, melt as it is sprayed on, such that it cover the whole surface. The adhesive layer and the solid polypropylene layers are then subsequently extruded and side wrapped onto the pipe while it is still heated. The pipes are then cooled down for safe handling during inspection before moving on to the last step. At the last step, the coating surface is reheated to softening point to ensure a good bond with the next layer. Straight after the heating, the pipe enters the cross head extrusion unit where the porous PP and the outer shield layer are applied by extrusion simultaneously. In the end, the pipe is cooled down by water, electrically inspected to ensure that there are no flaws in the coating, trimmed at the ends to get the required cut-back design, and placed in storage. Before deployment, the pipes are welded together, and the joints are covered with a solid polyurethane coating [34].

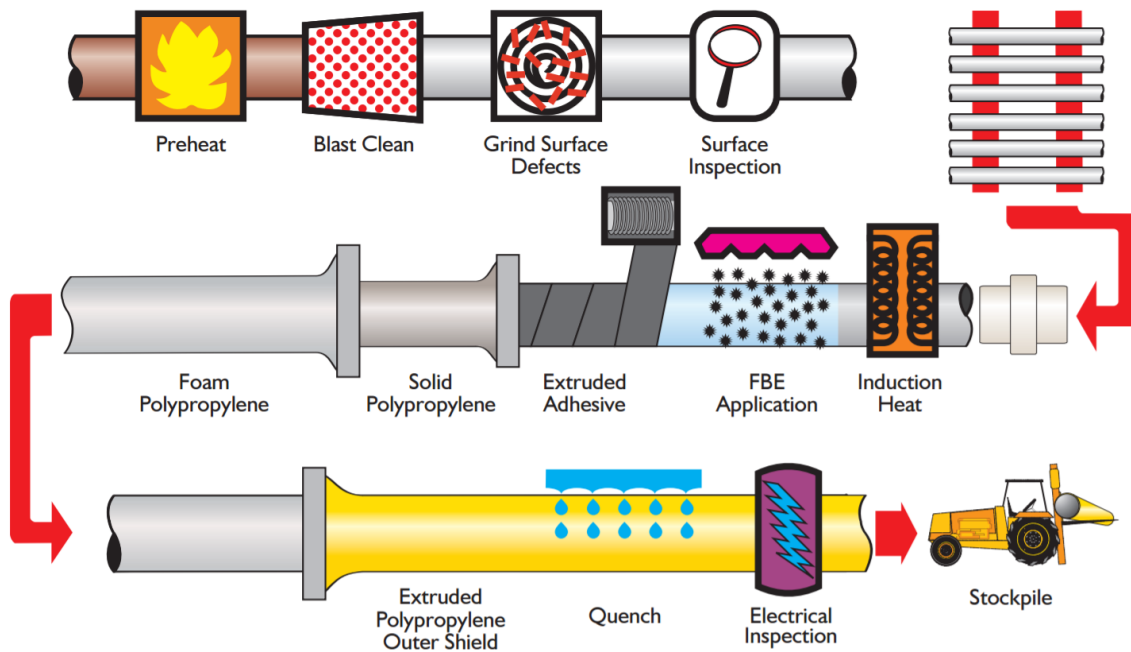


Figure 3.6: Coating manufacturing process [13].

3.2.2 Material parameters

A global axis system should be established. In Figure 3.7, the directions are shown with the pipe and coating measurements. The largest layer of the coating and the most important one is the porous PP layer (ca. 81%). The pores in the polymer create an excellent thermal insulator. At the same time, the energy absorption should be good during impacts. A lot more information was needed to fully

understand the layer and how it affects the impact and loading situation. What follows is a simple preliminary study on the porous polypropylene based on previous work by Holm and Røshol [11]. In their thesis, one model of the porous PP was calibrated. They used an elastic-plastic material model with the von Mises yield criterion (Sec. 2.1). This means that the model assumed isotropic behaviour, as well as pressure-, temperature- and rate-insensitivity. In Table 3.3 the model parameters are shown. Note that the hardening parameters were imported into the numerical model as a table of plastic strain and corresponding yield stress.

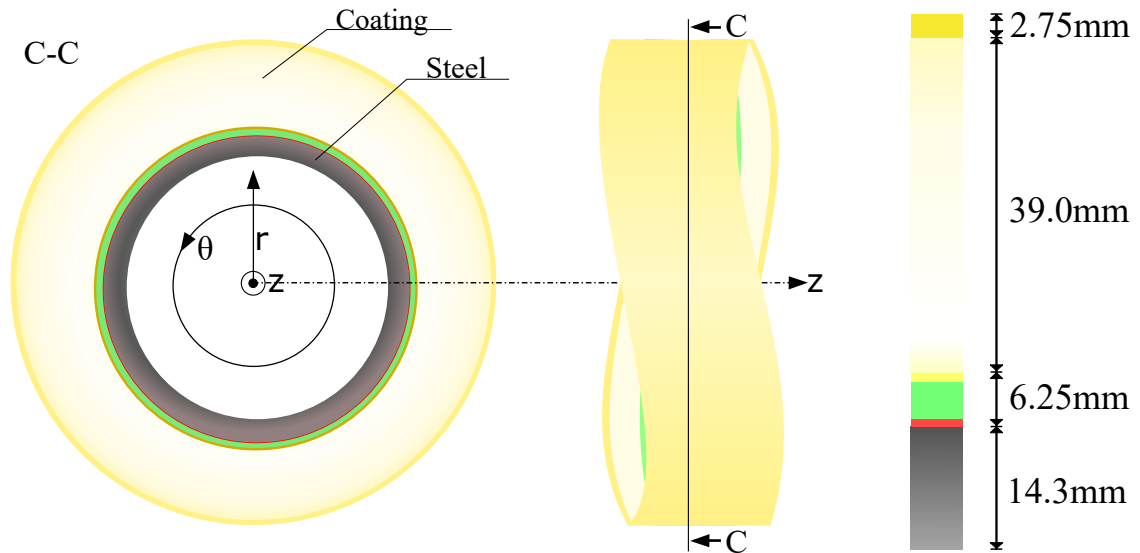


Figure 3.7: Illustration of axis system on the pipe and its measurements. Note that this is the profile cut of the pipe and that the axial direction (along the pipe, Z) comes out of the image. r is the radial direction, and θ is the hoop direction (cylindrical coordinates). The inner pipe radius (radial length to the start of steel pipe) is 122.3mm. The measurements used were taken from [12] and confirmed with a standard ruler.

Table 3.3: Material model parameters of the porous polypropylene. Calibrated by Holm and Røshol [11].

Density	Young's modulus	Yield stress	Poisson's ratio
ρ	E	σ_Y	ν
[kg/m ³]	[MPa]	[MPa]	[-]
730	401	6.8	0.3

3.2.3 Numerical model

The same quasi-static component test, as described in Section 3.1.3, was conducted on pipes with coating by Holm and Røshol [11], and then later recreated numerically. In their attempt to recreate the coated steel pipe they experienced several difficulties. The problems encountered were strongly connected with the ductile behaviour of the coating. As the coating is very ductile compared to steel, and the fact that steel is very much stronger than porous polymer, the numerical model suffers significant element distortions, which lead to numerical problems in the simulation. Running a standard simulation proved to be unlikely without getting extreme distortions in the elements. As a remedy, Arbitrary Lagrangian-Eulerian (ALE) formulation (Sec. 2.2) was applied to the simulation.

The ALE formulation fixed the initial problems with element distortions, but new challenges occurred

when the coating was fully compressed. At this point, the simulation again aborted due to element distortions, as the indenter ends up pushing the coating through the top nodes of the steel pipe. In the experiment, the coating fractured at this deformation. Holm and Røshol introduced a simplified fracture criterion, only based on equivalent plastic strain (PEEQ) to recreate this behaviour. However, this required the interaction to be described by general contact, all with self, while the ALE formulation requires the use of surface-to-surface interaction, so the fracture criterion was considered less important than ALE and excluded from the final simulations.

To get a better understanding of the numerical difficulties encountered in [11], a numerical model was established of the coating. The model was created following the procedure described in Section 3.1.3, but with more elements over the thickness and with the material parameters for the coating. The coating was then applied to the established model for the steel pipe, utilising the tie constraint function, and the interaction properties between the indenter and the coating were set to surface-to-surface, with penalty method constraint formulation, in order to include ALE. ALE formulation was applied to a limited part of the mesh, equal to the corner ABE illustrated in Figure 3.2b.

3.2.4 Results

As experienced by Holm and Røshol, the localised deformation in the coating proved to be a problem. Simulating the impact on the coated pipe the same way as for the steel pipe, resulted in severe element distortions, as can be seen in Fig. 3.8a. By introducing ALE formulation to the simulation, the problem with element distortion is avoided by the re-meshing process, as seen in Fig. 3.8b. However, when the coating was fully compressed, the simulation aborted due to numerical errors.

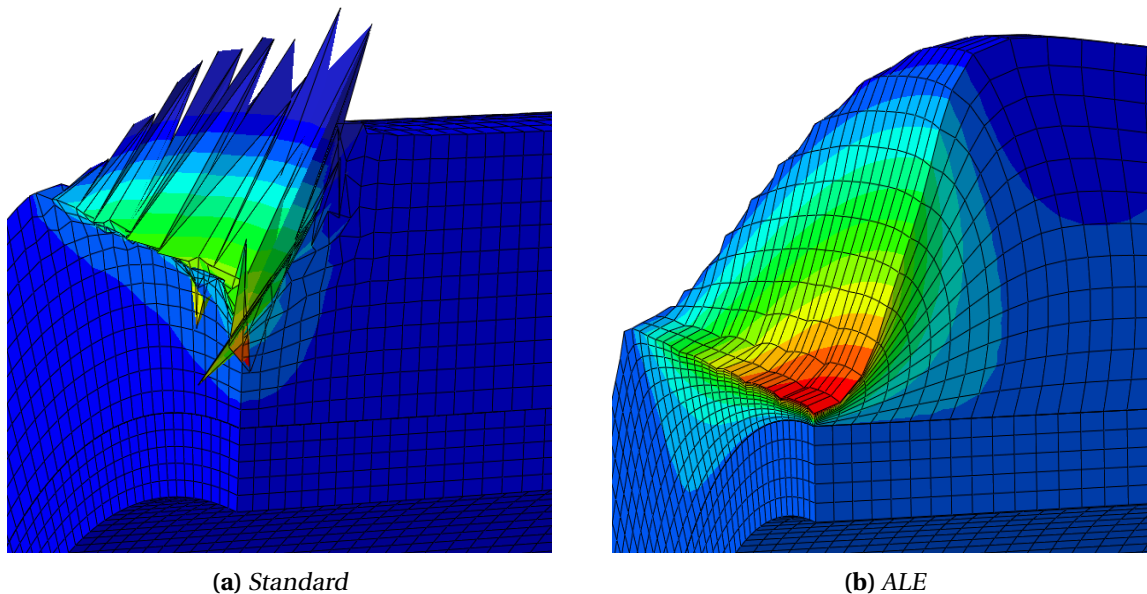


Figure 3.8: Deformed mesh after impact simulation. The contour plot illustrates the deformation in radial direction. Note that the coating is completely compressed while the steel pipe is relatively unaffected.

In Figure 3.9, the force-displacement curves from the experiment and the simulation are illustrated. It is clear to see that the results from the simulation do not recreate the experimental result well. The force needed to compress the coating is far below the values from the experiment, and the simulation

is aborted long before the experiment. Figure 3.9b also shows that the FD curve, from the simulation, for the inner displacement is too weak, however as most of the displacement of the steel pipe happens after the coating is fully compressed, there is not much data to compare the simulation with the experiment for the inner displacement.

By only considering the experimental results, some interesting aspects can be observed. For the outer displacement (Fig. 3.9a) an approximately linear behaviour is given for about the first 50mm. After that, a sharp increase is noted, before it levels out at about 60mm. In this period, the force jumps from about 700kN to about 900kN. This jump indicates that the coating is fully compressed and the steel pipe is utilising the remaining elastic capacity. Looking at the inner displacement (Fig. 3.9b) there is not much movement before about 900 kN. This means that the coating absorbs a lot of the energy from the impact and thereby reducing the deformation of the pipe. A much higher force is needed to attain the same level of deformation on a pipe with a coating, than a pipe without. A more thoroughly investigation of the coating's ability to absorb energy can be found in [32], where results on larger pipes and dynamic impacts are presented.

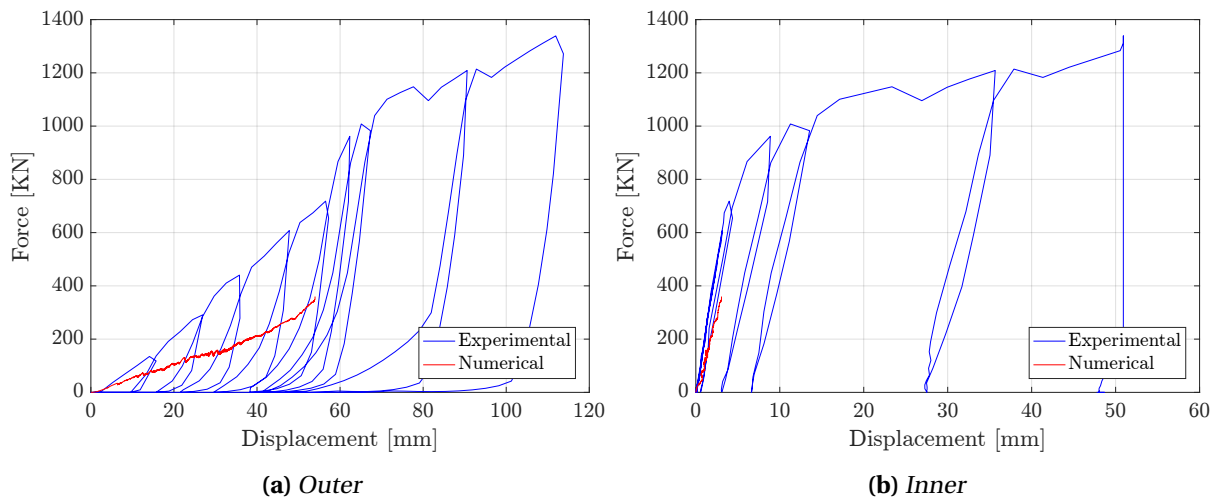


Figure 3.9: Force-displacement curves for numerical and experimental data for the coated pipe.

3.3 Summary and discussion

Much research is available on the steel pipe from previous papers; the material behaviour has been thoroughly investigated and described. There have also been conducted several numerical simulations on the pipe, so creating a good numerical model was pretty straightforward. The model gave satisfying results when recreating the quasi-static component test carried out in [11] and [32].

The simulation of impact on coated steel pipe did not yield a satisfying result. Element distortion was a major problem. The introduction of ALE showed good results when displacing the coating, but it also prevented the indenter to move past the coating and bend the steel. Hence, the possibility to compare the simulation with the experiment was strongly limited. The results that were obtained from the simulation did also highly underestimate the response compared to the physical test. It may be several reasons for this underestimation, linked to both the numerical model and the material model. More work on the porous polypropylene remains. Solving the numerical errors related to the full-scale simulation was put aside.

Experimental work

In the preliminary studies, it became apparent that the coating, particularly the porous polypropylene, needed more research and characterisation. In an attempt to do a thorough study, the experimental work had a focus on characterising the coating through X-ray computed tomography (CT) and uniaxial compression tests of small samples of the porous PP.

The CT scanning was conducted to get a non-destructive look inside the coating. In [16], the pores in the high-density polystyrene were analysed by cutting thin slices of the coating. It was assumed that the process of cutting the slices would interfere with the true pore morphology. With the use of X-ray computed tomography the internal structure of the pores would not be affected. Also, the specimens used in the compression tests could be analysed without being destroyed in the process. The CT image slices were later employed to re-create the specimens numerically (Chap. 6).

Solid polypropylene samples of equal size as the porous ones were subjected to the same procedure: X-ray CT scanning to make sure that they did not contain any pores, and uniaxial compression tests to compare to the porous specimens. The solid PP compression tests were employed at a later stage (Chap. 5) to calibrate a simple material model for the PP.

4.1 Measurements

Both CT scans and uniaxial compression tests were conducted on several specimens. To get a complete look at the insides of the entire coating solution a block was scanned as well. The size, weight and other measurements of the block and specimens are presented in this section. Also, the process of extracting them is explained.

Porous polypropylene

The specimens (samples) were cut from the coating in the form of cylindrical columns consisting of five samples as illustrated in Figures 4.2 and 4.1a. Three columns were extracted giving a total of 15 specimens. Each column, or series of specimens, was given a name (EG, EH and EI), and a number (1-5) specifying the sample. As an example, the specimen EH5 is the bottom cylinder, and EH1 is the top one.

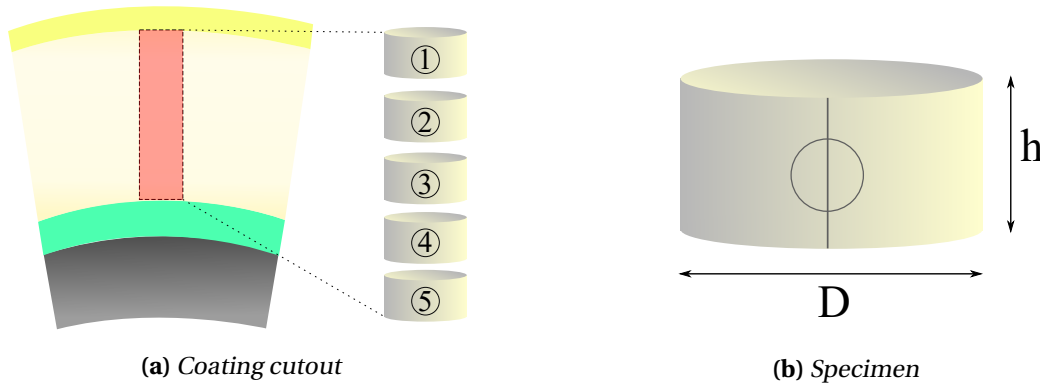


Figure 4.1: Illustration of specimen extraction (a) and specimen measurements (b). The numbers are the sample number, where number one is at the top, and number five is closest to the steel pipe. D is the diameter, and h is the height of the specimen. There is a space between the specimens to illustrate that they do not represent the entire porous coating layer - there was used a saw to cut the column into five small cylinders which were lathed as well.

The specimens were measured with a weighing scale and a micrometer (a measuring tool capable of estimating length as short as a micrometre), the result of which, is stated in Table 4.1. The micrometer was an MDC-25PX Mitutoyo micrometer [35] with a resolution of 0.001mm. The weighing scale was a Shinko DJ-600E [36] with a readability of 0.02g. Note that for each series the specimens of the same number (1-5) have the same weight. Realistically, there should be a difference considering the slight difference in diameter and height, but that was not captured by the scale. See Fig. 3.7 for coated pipe measurements and axis definitions.

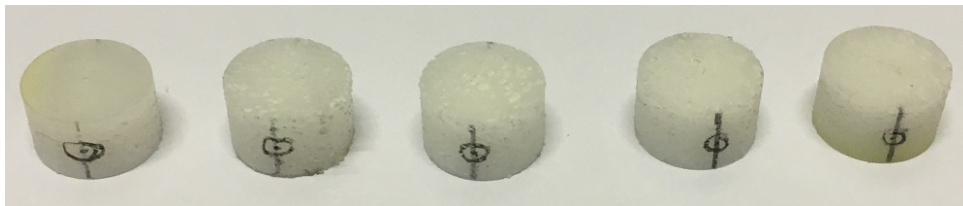


Figure 4.2: Image of the five specimens in column EG. The lines were drawn on the cylinders to tell the direction of the cylinders.

Every specimen had a "similar" diameter and height. The average and the standard deviation (STD) of all measurements are stated in Table 4.2. The STD was small for both height and diameter, which means that the average values could be used as a simplification when modelling the cylinders. It was assumed that the weight of the specimens has an uncertainty of about 0.01g because of the readability of the weighing scale (0.02g), i.e. if the measured value is 0.32g, the object could weigh anything in between 0.31g and 0.33g.

The measurements of the specimens give the column height of about 30.25mm (using the average values). The porous PP layer was measured to be 39mm (Fig. 3.7), which meant that 8.75mm of the layer was not included in the specimen series. It was assumed that the process of extracting the column and making the samples (lathing) resulted in a space between the cylinders. The saw blade used to cut the column into five cylinders have a thickness of about 2mm. Herein it was assumed that area was similar between all samples, and therefore set to 2.1875mm (8.75mm/4).

Table 4.1: Measurements of porous test specimens using a micrometer and weightscale. Note that direction south corresponds to the line going through the circle observed in Fig. 4.1b.

Specimen [ID]	Height Center [mm]	Height North [mm]	Height West [mm]	Height South [mm]	Height East [mm]	Diameter Northsouth [mm]	Diameter Eastwest [mm]	Weight [g]
EG1	6.042	6.044	6.048	6.040	6.042	9.979	9.981	0.38
EG2	6.058	6.056	6.068	6.067	6.068	9.989	9.998	0.34
EG3	6.075	6.079	6.082	6.075	6.069	10.002	10.007	0.32
EG4	6.057	6.063	6.063	6.059	6.057	10.006	10.004	0.36
EG5	6.014	6.011	6.006	6.019	6.013	10.015	9.997	0.40
EH1	6.031	6.025	6.028	6.041	6.036	9.993	10.005	0.38
EH2	6.070	6.064	6.069	6.109	6.063	10.001	10.005	0.34
EH3	6.085	6.081	6.085	6.080	6.074	10.010	10.054	0.32
EH4	6.056	6.059	6.065	6.055	6.053	10.018	10.016	0.36
EH5	6.023	6.032	6.026	6.022	6.027	10.029	10.011	0.40
EI1	6.020	6.022	6.024	6.027	6.027	9.973	9.968	0.38
EI2	6.060	6.060	6.058	6.056	6.061	9.986	9.982	0.34
EI3	6.061	6.068	6.050	6.054	6.067	9.994	10.020	0.32
EI4	6.067	6.070	6.049	6.069	6.071	10.007	10.003	0.36
EI5	6.012	6.008	6.010	6.035	6.010	10.017	10.005	0.40

Table 4.2: Average values and standard deviation of the height and diameter data in Table 4.1.

Height h [mm]	STD – [mm]	Diameter D [mm]	STD – [mm]
6.050	0.023	10.0025	0.0174

The block containing the entire coating solution was measured as well, but not as accurately. The measuring tool was a standard ruler. The measurements of the block are shown in Fig. 4.3. Note that the height of the porous polypropylene layer is confirmed by the measurements in [12].

Solid polypropylene

Some compression tests were necessary for solid polypropylene to compare to the porous specimens. For this reason, the solid samples were shaped to have the same measurements as the porous ones. To get specimens of solid PP a block of the material was made by Shawcorp at their factory in Orkanger, Norway. Nine cylinders were extracted from the block as illustrated in Fig. 4.4. Remember that D

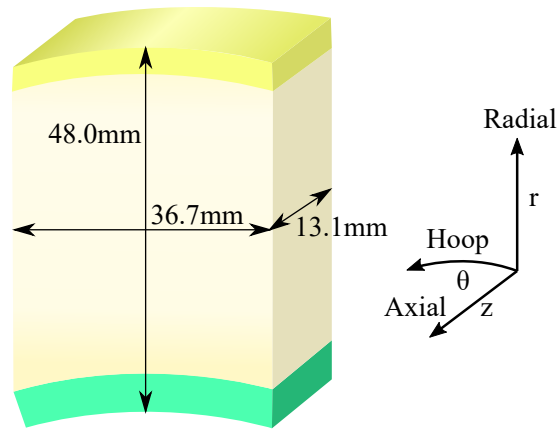


Figure 4.3: Measurements of the block containing all coating layers.

and h corresponds to the same variables as shown in Fig. 4.1b. First, a slice of the block was made at a distance $a = 10\text{mm}$ from the edge. Then the cylinders were extracted as illustrated. Note the identification name given the samples. K, L and M correspond to a column, and the numbers 1, 2 and 3 correspond to a row.

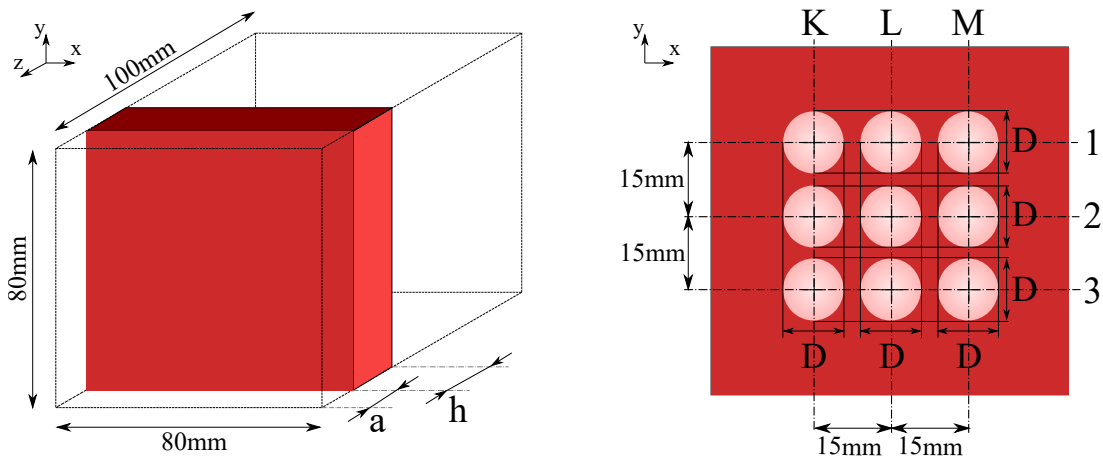


Figure 4.4: Extraction of pure PP specimens. A large slice with thickness h was cut from the block at a distance a from the edge. Nine cylindrical specimens were then cut out as illustrated, where D is the diameter.

The solid specimens were then measured as the porous ones. The same micrometer and weighing scale were used. The result of which is found in Table 4.3. Note that the measurements are quite similar to the porous specimen measurements, all but the weight. Also, the height was only measured at the centre of the sample.

Table 4.3: *Measurements of solid test specimens using a micrometer and weightscale.*

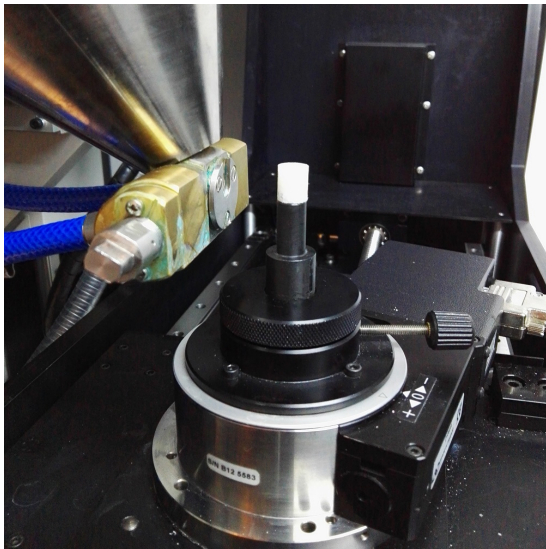
Specimen [ID]	Height Center [mm]	Diameter Northsouth [mm]	Diameter Eastwest [mm]	Weight [g]
K1	6.022	10.028	10.023	0.42
K2	6.043	10.030	10.031	0.42
K3	6.025	10.030	10.028	0.42
L1	6.031	10.028	10.028	0.42
L2	6.026	10.021	10.021	0.42
L3	6.027	10.027	10.023	0.42
M1	6.028	10.029	10.027	0.42
M2	6.031	10.026	10.028	0.42
M3	6.028	10.031	10.032	0.42

4.2 Computer tomography

The pore structure and morphology of the porous polypropylene layer was investigated using X-ray computer tomography (see Section 2.3 for more information). CT image slices were captured of every specimen (both solid and porous) and the block.

4.2.1 Test setup

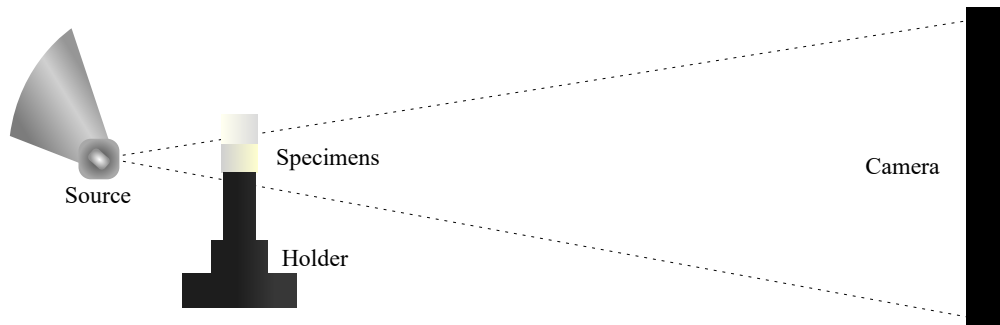
The machine used to do the X-ray scanning was an industrial Nikon XT H 225 ST CT-scanner [37]. According to the manufacturer, this system works well with a wide range of materials and sample sizes. The machine has three interchangeable sources: reflection target, transmission target and optional rotating target. The system offers a little focal spot size of 3 microns, a 225kV microfocus X-ray source, and it can hold samples up to 50kg with a diameter of about 50cm.



(a) Source, rotating holder and specimens



(b) Back plate (camera)



(c) Illustration

Figure 4.5: X-ray CT scanning setup.

The XT H 225 ST machine produces high-resolution raw image data. These images are then used to reconstruct the volumes with software capable of said operation (such as the XT software). The source material, on which a high energy beam hits, produces the X-rays. A choice between wolfram (W),

silver (Ag), molybdenum (Mo) and copper (Cu) as the source material must be made. The material could be changed by turning a handle. Filters could also be added.

Each specimen was placed in the machine on the rotating holder as shown in Figure 4.5 with the line and circle pointing at the source (for the solid specimens the direction was not relevant because they were assumed to be homogeneous). For the EH series, a tape was placed at the top to indicate the direction of the specimen in the scan results so that the direction was correct and equal among all EH samples.

In this setup, the X-rays travel in a cone shape (cone beam), and as discussed in Section 2.3, this results in a reduction in matter for the X-rays to penetrate at the top of the specimen, thus altering the results. A simple fix was to put a second specimen at the upper part with the non-porous side down (typically EI1 was used). At the bottom the holder fixes this issue. Note that specimen EI1 was not scanned with another one on top. The samples were placed close to the source so that the specimen covered almost all of the screen (to get the highest resolution). The source material used was wolfram.

The scanner was calibrated correctly for each specimen. The number of angles of rotation and how many frames per angle was chosen. It was assumed that more pictures per angle were better than more angles, because using the average of the pictures taken at each angle resulted in less noise in the images. Next, the image histogram was checked. The grayscale values should be between 62000 and 12000 (16-bit grayscale values), and as close to the white level as possible (about 60000). A small rectangle was digitally put on both sides of the sample (on the screen). If there are any changes of the grayscale values in the rectangle the scanner will reposition itself so that the specimen is always on-screen. The process is called flux normalisation.

In Table 4.4 the test parameters are stated. Note that the value of the power varies a bit. The reason for this was the calibration of the histogram. For the solid specimens, the same values as the porous ones were used, with the exception of power which was set a bit lower at $89\mu\text{A}$.

Table 4.4: *CT scanning parameters for the porous specimens.*

Exposure time	Frames per angle	Angles	Source material	Voltage	Power	Noise reduction	Filter
[ms]	[-]	[-]	[-]	[kV]	[μA]	[dB]	[-]
1000	2	1571	W	150	92-98	24	No filter

The raw image data was then processed by a computer with a high memory capacity (48Gb RAM). That was important because the processing software must have the entire raw data and the complete reconstruction of the sample in the memory (about 25Gb). The specimens were reconstructed, and slices were made in the radial direction of the pipe (top-down) and two perpendicular directions (side-to-side). See Figure 4.6 for an illustration of the slice reconstruction planes. 3D models of the specimens were not exported, as the files would be too large to work with on a personal computer.

A block of the entire coating solution was also scanned. This block was larger than the specimens. Therefore the block was placed further away from the source, resulting in a bit lower resolution of the pores. Different parameter values of the scan were needed, which is reasonable since the block is thicker than the specimens. The difference was the exposure time (2000ms) and the power ($46\mu\text{A}$).

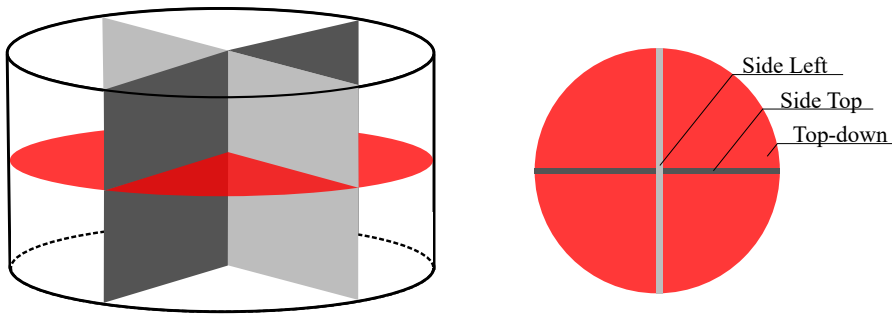


Figure 4.6: Illustration of 2D slice reconstruction planes on the specimens.

4.2.2 Results

The CT-scanning of the specimens were all successful and resulted in over 800Gb of image data. The block was successfully scanned as well. In the following, the results of the scanning are presented. Note that each scan completed after about 53 minutes.

Porous specimens

There were many images, and to save some space in the thesis the EH series is the only one considered further herein. The EG and EI series were very similar to the EH series, and the results of their scans are found in Appendix A. The EH series was also the only series where the specimen was added a tape piece on top to determine the direction. This way the EH specimen CT images are easy to determine the correct orientation. Note that the pores are oriented differently in the EI series (compared to the other sets; see App. A.1). The reason for this was unknown, but it was assumed that the specimens were scanned at a different orientation (no tape was added so the direction could not be determined).

In Figure 4.8a, a raw image of every specimen is shown for the EH series. Note that in this figure there is chosen only one image per specimen, while the total number of images per specimen was 1572. The angle of rotation was about the same for all of them. In each image, there are three separate parts. At the bottom, in almost pure black, is the rotating holder. Above, in the middle, the specimen is visible, and at the top another specimen with the pore-free side down.

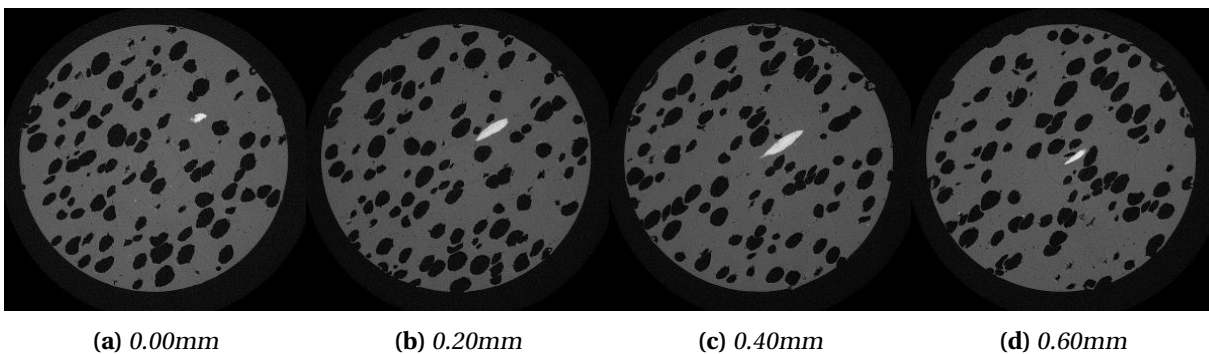


Figure 4.7: Artefact found in specimen EG3 at a distance of 5.26mm from the bottom. The white and brightest spot is the artefact. It is unclear what this is. The corresponding values measures the distance of the slice relative to the first one (a).

Several properties of the porous PP specimens could be observed in the raw images. Varying pore properties were present. EH1 has no pores at the top, and EH5 has no pores at the bottom. The pore size and the orientation (angle) of the pores changes throughout the coating. Note the middle part of EH3 where there is an impression of a transition from one pore structure to another. It is hard to tell from these images, but the orientation of the pores changes significantly at this transition zone. At this stage, the reason for this was unknown and needed further investigation.

2D slices were made from every specimen with the use of the software ImageJ [38], in the radial direction and two perpendicular directions (Fig. 4.6). In Figure 4.8d a top down slice in the middle of every specimen is shown, and the Figures 4.8b and 4.8c show the side slices. The bright part of each image is the matrix material, i.e. pure polypropylene, and the dark parts are non-solids. The dark spots inside the PP are the pores.

The transition between two pore structures is present in Figure 4.8. Specimens EH1 and EH2 show round and clear pores with few small ones, while specimens EH4 and EH5 have more elongated pores, as well as many small ones. A change in the pore orientation was observed as well. In the middle of EH3, the transition zone is noticeable.

Artefacts (Sec. 2.3) was present in the CT scan results. In Figure 4.7 a large artefact was observed on the top-down slices of EG3. The origin of the object was unknown. Artefacts can arise in CT images due to beam hardening and numerical errors in the reconstruction process [23]. Those type of artefacts usually presents themselves on the pictures at random. The artefact in EG3 is connected in 116 images and is shaped like a pore. The fact that the artefact is a lot brighter than the rest indicates a much higher density. Maybe a metal piece was somehow introduced when the coating was sprayed on the pipe. Many artefacts were observed in every specimen, but not as large as the one in Fig. 4.7. Nonetheless, these spots were assumed to be of no importance and therefore interpreted as polypropylene.

Block

The block of the entire coating solution was successfully scanned. In Figure 4.9 the results are shown. Here a transition zone was clearly observed in the middle, where the pore structure changes. The different layers in the coating solution have various brightness. That implies that the layers have different densities, but the difference is small. It was also noted that the porous PP layer was the only layer containing pores. The pore structure clearly varies with the radial direction. The hoop and axial direction do not seem to affect the structure (investigated in Chap. 5).

There was a hint of an irregularity in the lower half of the block, which is visible in Figures 4.9a and 4.9b. From the middle left to the bottom right, there is a line of solid PP. The line was quite thin and was assumed not to affect the pore morphology.

Solid specimens

The solid polypropylene specimens were scanned only to make sure that there were no pores in them. For this reason and the limited time on the CT scanner, only four of the nine specimens were scanned.

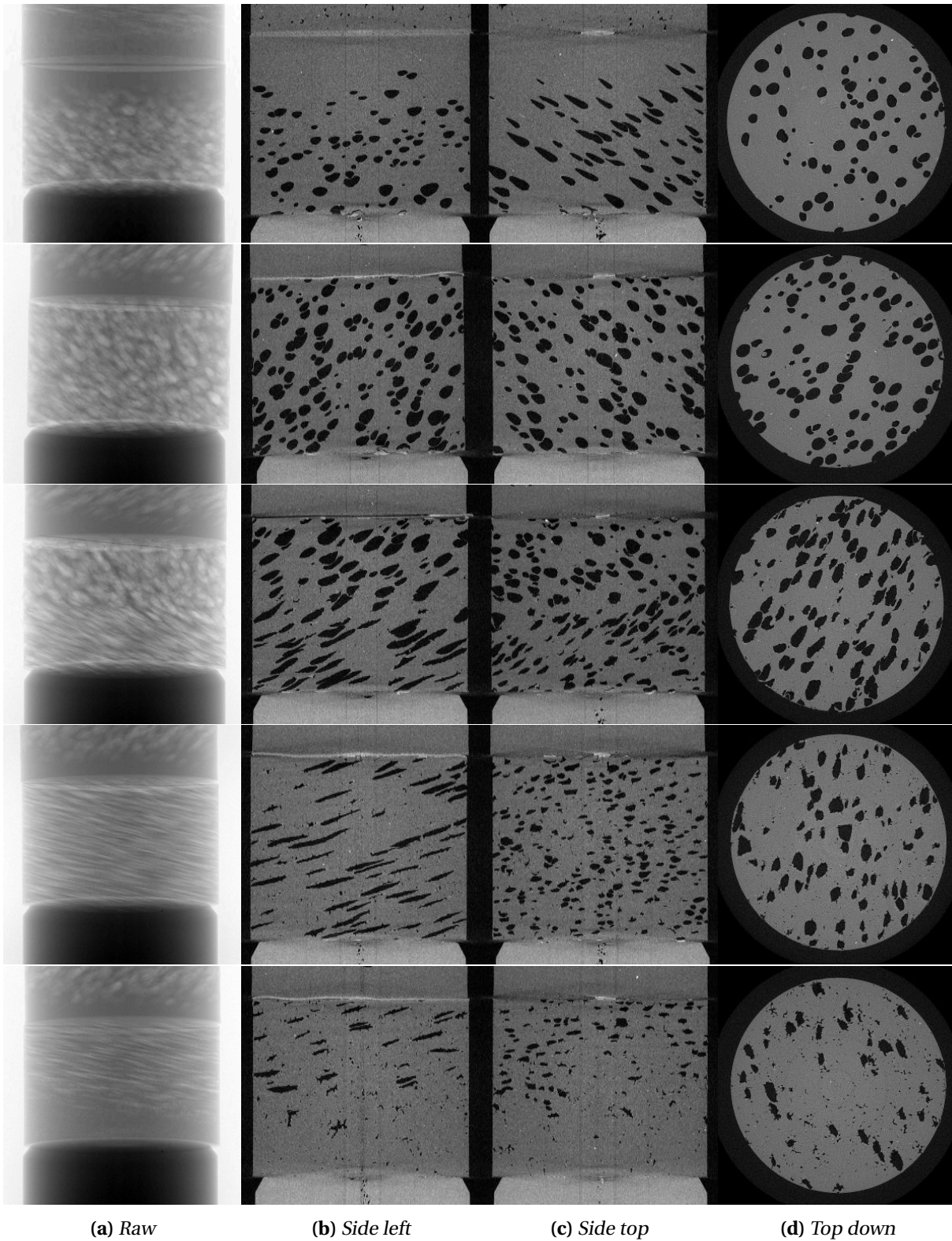


Figure 4.8: CT scan results of column EH. The image row at the top is EH1, next is EH2 and so on. The bottom row is EH5. Note that the side left, side top and top down slices are in the middle of their respective specimens (Fig. 4.6).

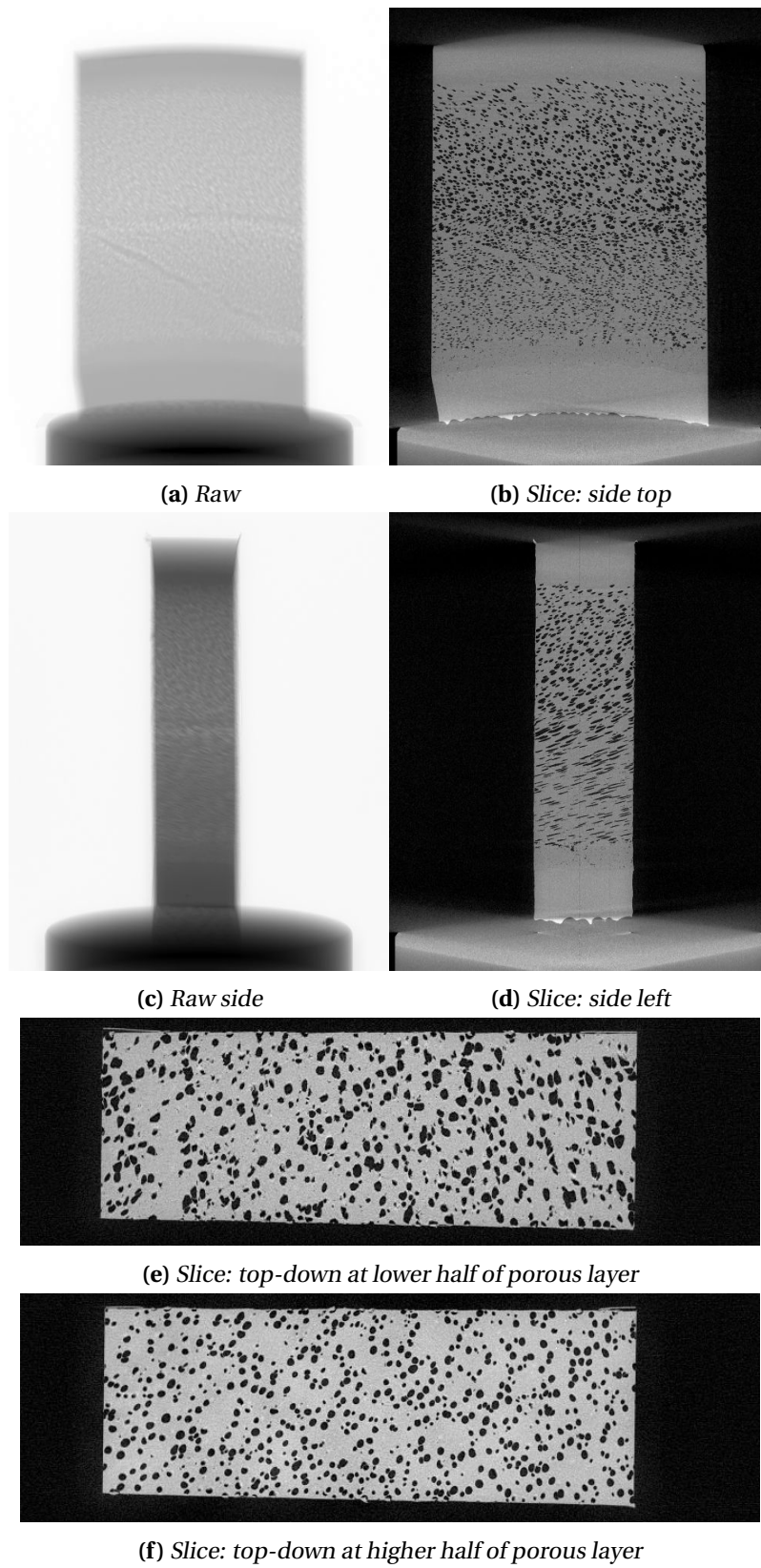


Figure 4.9: CT scan of the block. The slices (b) and (d) were taken in the centre.

The results of the scanning are shown in Figure 4.10. Three of the specimens did not contain any pores. They were completely solid. The L2 scan showed some pores at the left side at about 1mm from the bottom. These pores were quite small, and there were very few of them. Considering that the weight of each sample is the same, at least there are no significant pores inside.

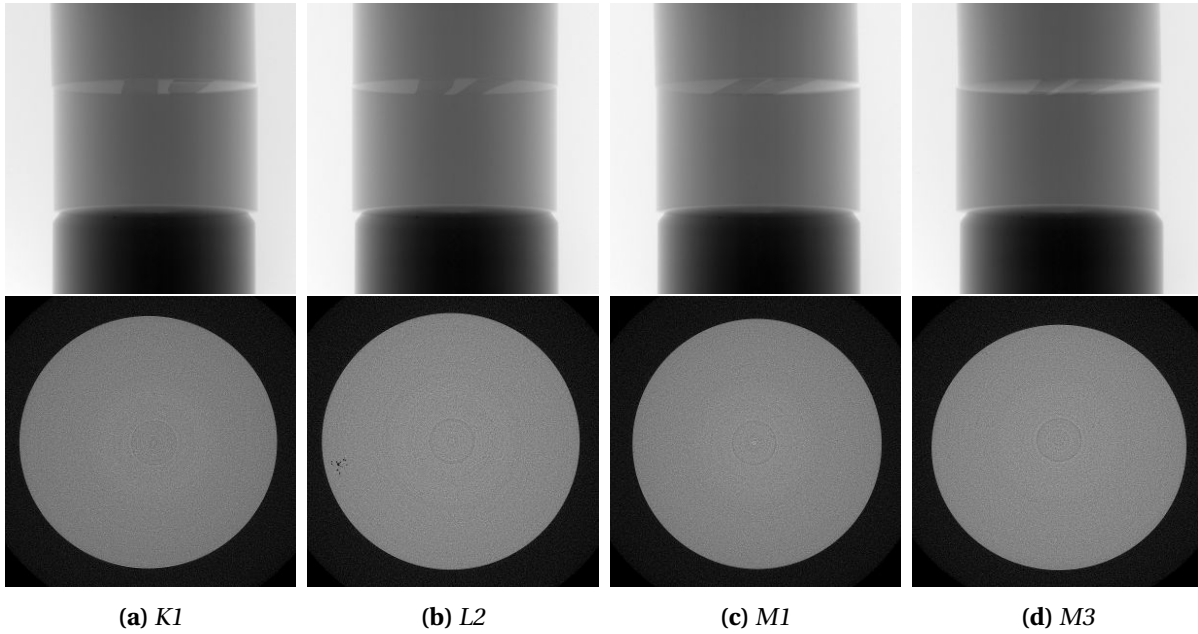


Figure 4.10: Solid CT scan results. The images in the top row are the raw images, and bottom row is the top-down slices taken at 1mm from the bottom. Note the pores in specimen L2 at the left in the slice.

4.3 Uniaxial compression

As the coating is most likely to be subjected to compression, uniaxial compression tests were a necessary experiment and were conducted on specimens - both porous and solid. In this section, the test setup and results of the compression tests are shown and discussed. The porous specimen compression results are then compared to the solid ones.

4.3.1 Test setup

The uniaxial compression tests were performed using an Instron 5982 [39] system. The test machine uses a static load cell with capacity up to 100 kN. The specimens were placed between a steel cone and a compression cylinder as illustrated in Figures 4.11 and 4.14. Every specimen was given an additional line on the top, perpendicular to the vertical one, to orientate the specimen before initialising the compression. The specimens were compressed to a displacement of about 4mm.

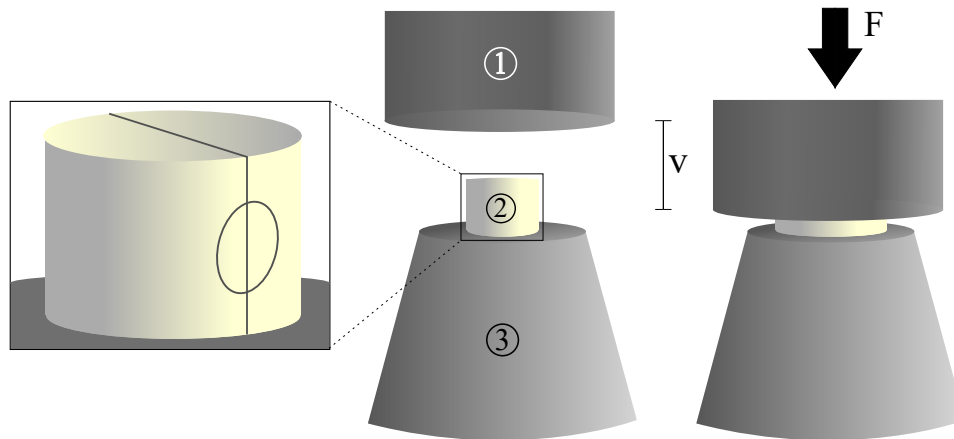


Figure 4.11: Experimental setup for uniaxial compression tests. 1 is the compression cylinder (load cell), 2 is the specimen, and 3 is the holder (steel cone). The load cell measures the force (F) and the displacement (v).

The compression process was recorded with two cameras, synchronised with the load cell, to post-process the deformation of the specimen with digital image correlation (DIC) [40]. Three different camera setups were employed, as illustrated in Figure 4.12 and depicted in Figure 4.14. For the two sample columns EG and EH, the two cameras were aligned to capture images for 3D DIC analysis, while for EI the cameras were aligned at a 90-degree angle to capture most of the deformation suffered by the specimen. Setup 3 was used during the solid specimen compression tests. Here camera 1 captured the specimen and the speckle pattern, while camera 2 captured the compression cylinder and holder (both were added a checkerboard pattern to make the DIC tracking easier). The cameras were a Prosilica GC2450 [41] with a 100mm F2.8 Samyang telephoto macro lens [42]. In all setups, two direct lights were used to get a clear view of the speckle pattern for the cameras.

Before the compression, all of the specimens were applied a layer of speckle pattern, necessary for DIC to capture the deformation. The speckle pattern was a black paint sprayed on a white painted specimen surface, creating a pattern resembling a checkerboard (Fig. 4.13). A layer of Molykote G-n metal assembly paste [43] was applied at the top and bottom of the specimen to reduce the effect of friction during contact. The paste is a high-pressure resistance and low friction paste according to the

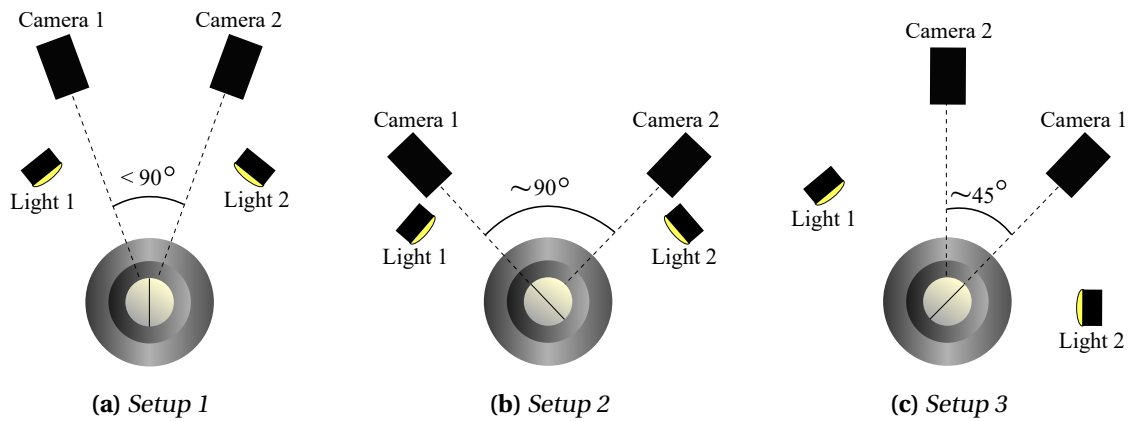


Figure 4.12: Camera setups for compression tests. Setup 1 (a) was used for EG and EH series, while setup 2 (b) was used for EI. Note that for setup 1 the specimens point at the middle of the cameras, and for setup 2 the specimens point directly at camera 1. Setup 3 (c) was used for the solid samples.

manufacturer. In similar tests conducted in [11] a slick tape was applied to the ends of the specimen in order to reduce the effect of friction. However, as this also will somewhat limit the specimen from expanding because one side was adhesive, the tape was not used.

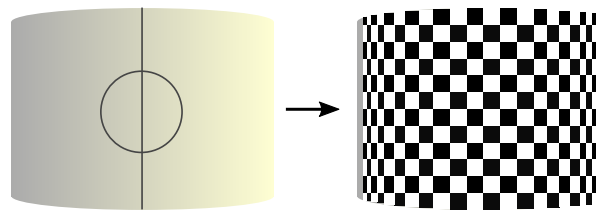


Figure 4.13: Speckle pattern applied to a specimen.

All porous specimen were subjected to compression at a strain rate of 0.001s^{-1} , which means that the compression cylinder moved at a velocity of 0.006mm/s . The cameras were adjusted so that the image capture frequency was 1Hz (one frame per second). At the same rate (and time) the information from the compression cylinder (force and displacement) was extracted. The test lasted for about 670 seconds, which then means that there were 670 data points. For the solid specimens, the same values were used, but the M-series' compression velocity was increased by one decade. The load cell then moved at a speed of 0.06mm/s , and the camera frequency was set to 10Hz . That way, the same amount of data points was achieved. It was assumed that the K- and L-series was enough to get data for the solid PP compression tests. Therefore, as a simple study, the strain rate was increased.

4.3.2 Results

The compression tests were all successful and resulted in raw force-displacement data found by the Instron machine and many images taken during the deformation of the specimens. What follows is a presentation of the results - first the porous samples, then the solid ones with a comparison of the two.

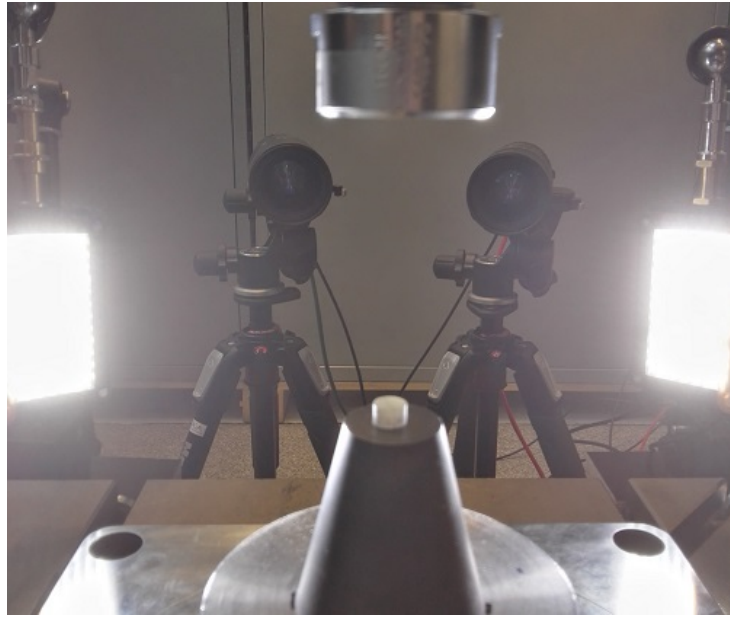


Figure 4.14: Experimental compression setup. Note that this is camera setup 1. The speckle pattern and grease had not been applied yet. The compression cylinder (load cell) is located at the top.

Porous specimens

All three columns (series) of the porous PP was compressed to about 4mm displacement. Figure 4.15 shows the results of all of them in the form of force-displacement curves. The data used in this plot was the raw data obtained by the Instron machine. Note that each subfigure represents a specimen number and that the vertical axis is shared. It was easily observed that the FD curves were relatively equal when considering the same specimen number. Therefore, same as the CT results, the EH series are considered in the following.

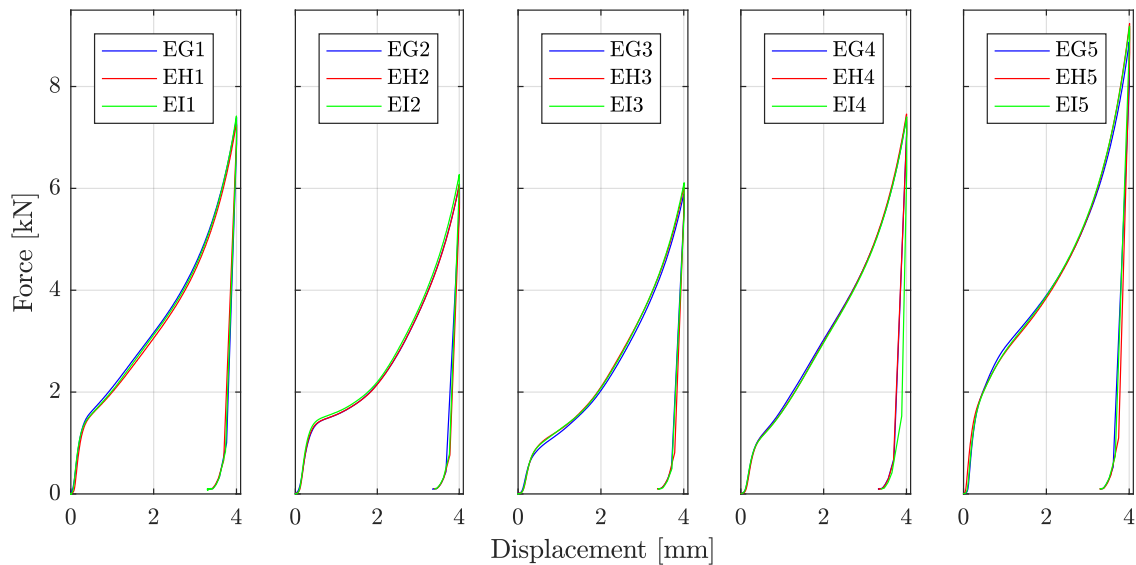


Figure 4.15: Results from compression tests in the form of force-displacement curves.

In Figures 4.17 and 4.16 the force-displacement curves and the images of the EH series compression tests are shown, respectively. The slow rise in the curves was expected to be wrong. In reality the specimen itself should experience a linear increase in force at the start. The slow rise was assumed to be because of the grease being pushed in and outside of the specimen, and the fact that the compression cylinder was placed slightly above the specimen before the test began. Figure 4.18 illustrates the grease being pushed. Note that in this figure the specimen does not experience any significant deformation while the grease is pushed. Another important reason for the slow rise is the nonuniform height of the specimen (Tab. 4.1), which suggests that a specific displacement was needed before the cylinder was uniformly compressed.

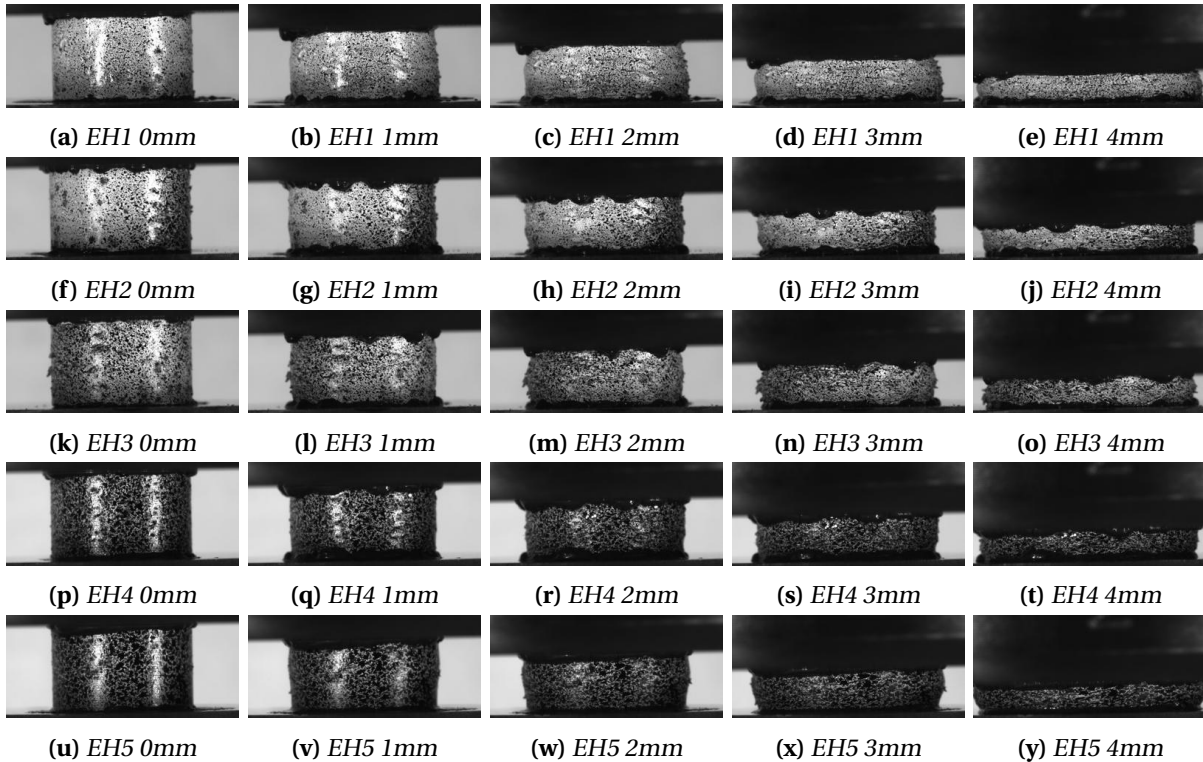


Figure 4.16: Results of EH compression tests.

There was some concern about the accuracy of the displacement measurement gathered from the Instron system. It was suspected that the machine stiffness or the elastic bending of the Instron machine during compression could affect the measured displacement values. The potential error was investigated. One of the cameras from the test with solid PP was adjusted to capture the movement of the load cell. The chessboard pattern applied to the lower cross head allowed DIC to track its movement by applying a subset to one of the intersections of the pattern, as illustrated in Figure 4.19a. The movement in DIC was converted from pixels to a physical length (in millimetres) by utilising the known height of a square (1.2956mm), and the resulting movement was compared to the displacement logged by the testing machine, as seen in Figure 4.19b. The figure clearly illustrates that there is a negligible difference between the two curves. This result shows that the machine stiffness or the elastic bending of the Instron machine during compression do not affect the measured displacement values within the test range.

In Figure 4.17 the FD curves are not corrected; the curves should be optimised to account for the wrongfully slow rise at the start. The actual displacement of the specimens was desired, and assumed

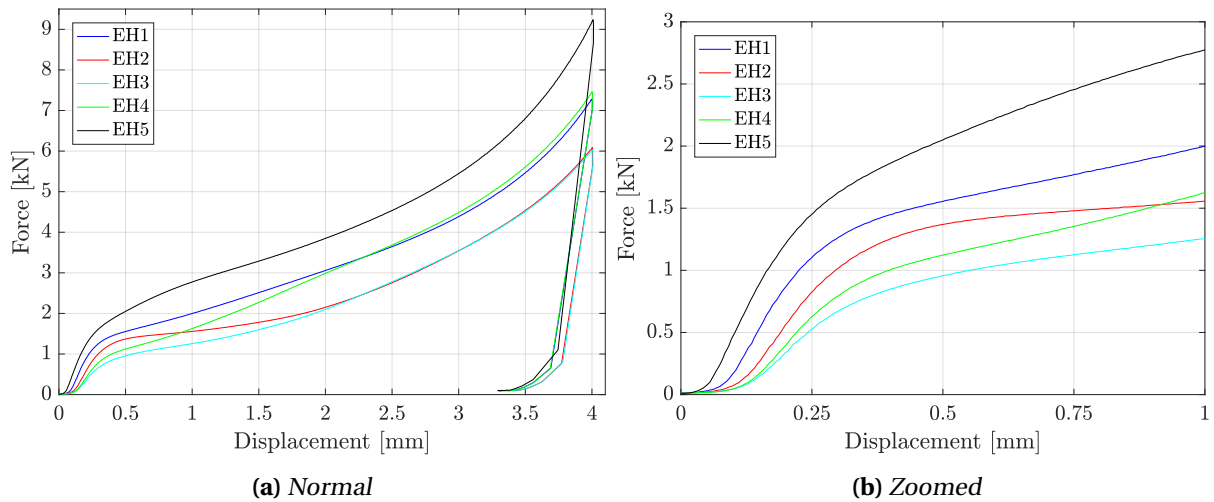


Figure 4.17: Force-displacement curves of the EH series. In (b) the curves are zoomed in on.

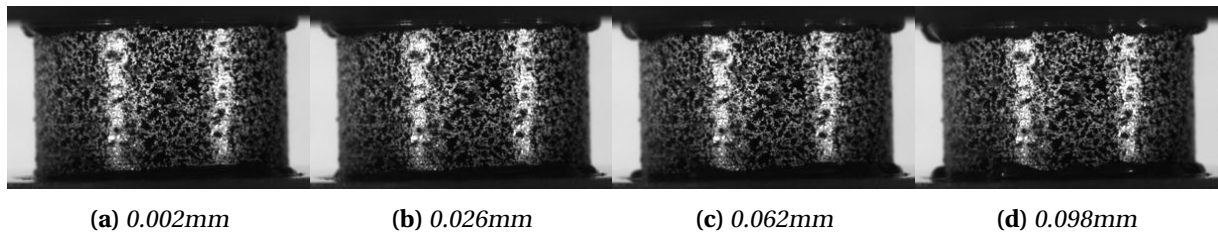


Figure 4.18: Images of EH4 at the start of the compression test. Each image is taken at the respective displacement of the compression cylinder. Note that the grease (black fluid at the top and bottom) is squished out.

to correct the slow rise. DIC was supposed to take care of this problem, but that proved difficult. First of all, the grease was quite thick, and when compressed it was pushed out to the sides of the specimens, and it started to flow downwards, hiding the speckle pattern at the top (bottom as well, but not as much). The desired displacement is measured from top to bottom, but the grease covered the edges, making it impossible to find with the use of DIC. The displacement measurements could be taken in between the grease, but since the samples are inhomogeneous (pores) the values would be incorrect. Second, the lighting setup rendered two white lines on the specimens' images (Fig. 4.18). They originated because of the direct light sources and the fact that the specimens are cylinder shaped. A flat surface could easily avoid the bright shine. The bright lines figuratively remove part of the speckle pattern causing the images harder to track with DIC. The problem could be evaded by the use of ambient light instead of direct lights.

The white lines provoked a bigger problem when working on 3D DIC, as illustrated in Figure 4.20. The images were taken at a displacement of 0.1mm from the compression test on specimen EH5. Both camera views show the usable part (red rectangles) for 3D DIC. The reason for this small area is the white lines that are located at different material points for both cameras i.e. the left line in the camera 1 image does not cover the same physical spot as the left line in the camera 2 image. The DIC mesh must be representing the same material points on the specimen, so the software uses a grayscale optimisation technique. This technique changes the position of the mesh at image 2 (camera 2) so that the grayscale values in the mesh on image 1 and image 2 are relatively equal. Since the bright lines do not cover the same spot, this optimisation does not work, and as a consequence, the mesh does not link up correctly. The measurements obtained from 3D DIC would then be incorrect.

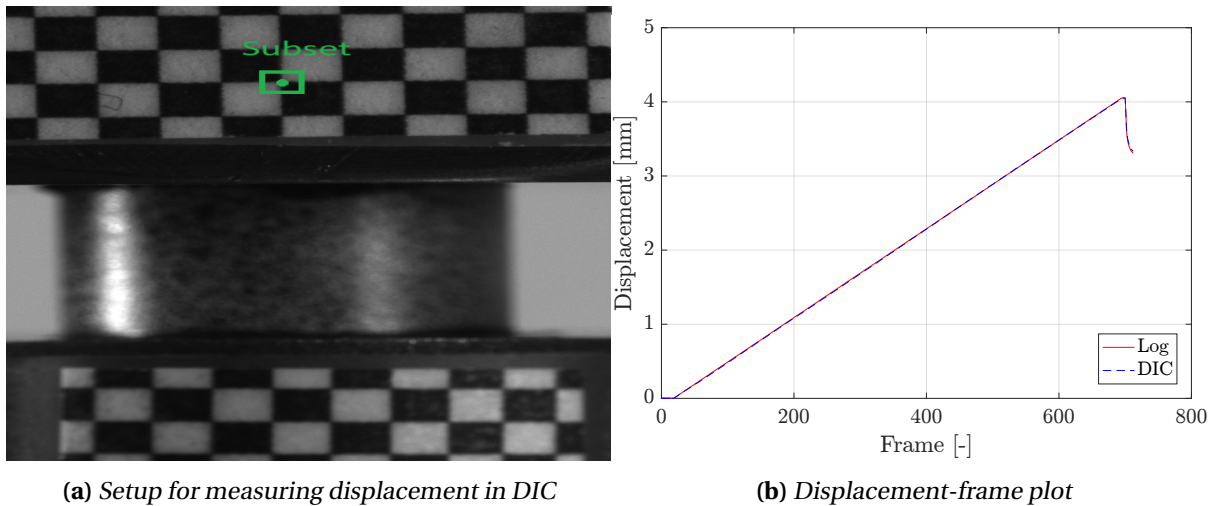


Figure 4.19: DIC was employed to find the true displacement of the compression cylinder, and compare the result to the Instron machine’s measurements. No difference was observed, i.e. the machine stiffness does not affect the displacement measurements.

Digital image correlation in 2D proved difficult as well. The cylinder shape of the specimen demands 3D DIC to get accurate stress and strain measurements. With the 3D setup, the in-plane direction (in the images) could be accounted for. The remaining DIC possibilities were quite few. So the wrongfully slow rise in the force-displacement curves (non-linear) was corrected with a simple linear backwards extrapolation. It was assumed that the curves should start with a linear behaviour, so a linearisation of the curves was conducted as illustrated in Figure 4.21. The curves were then translated to the origin so that the compression test starts with zero displacements. The resulting curves are presented in Figure 4.22. Note that the correction of the curves was not only conducted to get a more realistic result but to check the numerical models developed later. The models will be linear at the start because of an elastic material model, and no grease in the simulations.

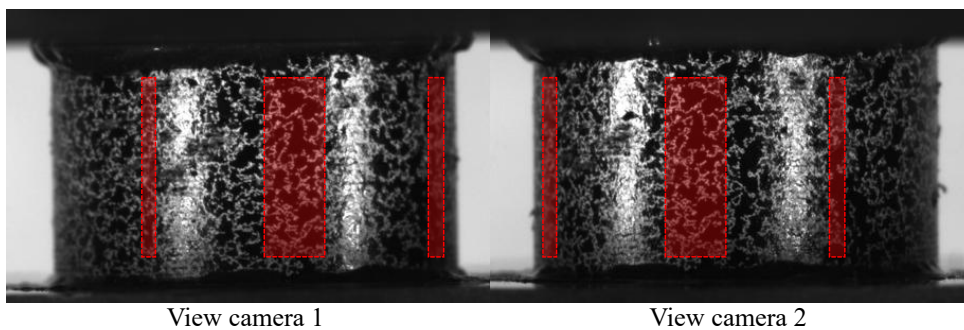


Figure 4.20: 3D DIC mesh optimisation. The red rectangles represent the mesh. The mesh was removed where the white lines interfere. The remaining mesh is very small and can not be used for accurate measurements.

The different curves in Figure 4.22 showed some interesting results. First of all, every specimen had a different curve, which may indicate that the pore structure affects the curves. Next, there seems to be three groups in the end; EH5 in the top (9.2kN), EH1 and EH4 below (7.4kN), and EH2 and EH3 at the bottom (6.0kN). In Figure 4.21b the yield points for the specimens are presented; the point is recognised by the sudden curvature after the linear start. The yield point is also different for the samples. Furthermore, the shape of the curves varies; EH2 and EH3 have an interval after yielding where the force do not increase as rapidly (about 0.5mm to 1.5mm displacement), EH1 and EH4 have

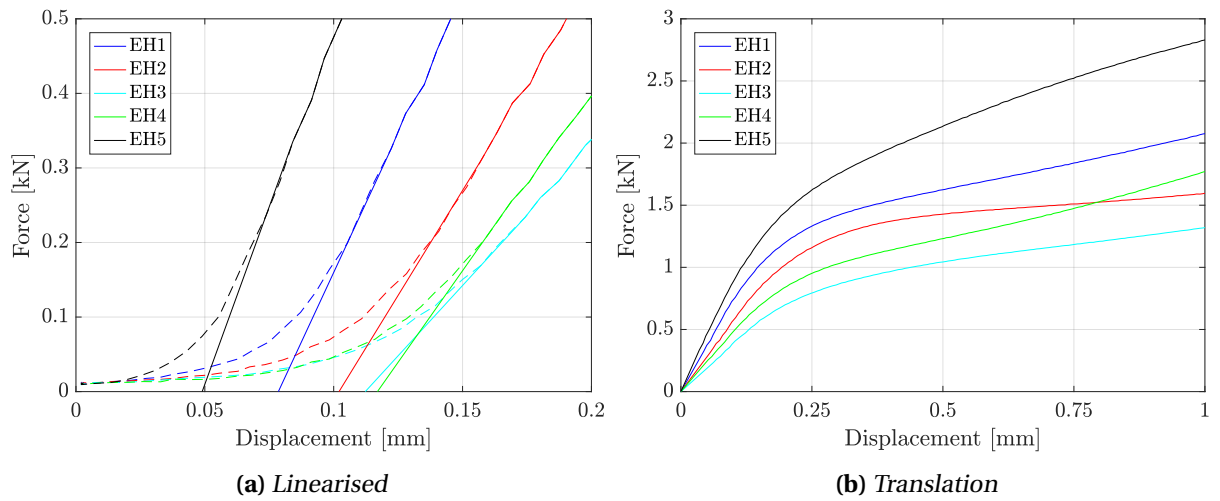


Figure 4.21: Force-displacement curves of the EH series showing the correction steps. In (a) the whole lines are the new linearized curves. In (b) the new curves were translated so that the curves started in the origin (0,0).

a steeper one, and EH5 show an even more rapid rise in force. Also, EH4 has a low yield, but the highest increase of force. Furthermore, note the deformation shape of the specimens (Fig. 4.16).

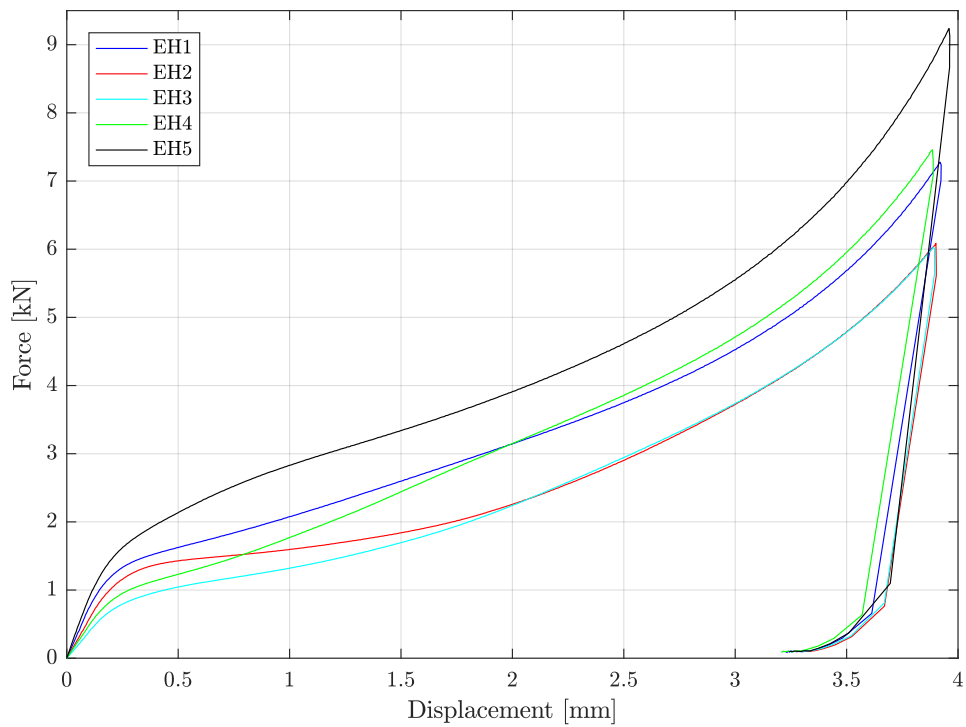


Figure 4.22: Corrected FD curves of the EH series.

Solid specimens

The results of the solid PP compression tests were successful. The results are shown in Figures 4.23 and 4.24. Remark that the force-displacement curves were corrected the same way as the porous specimens' curves. It was immediately observed that there was relatively no difference in the curves (M-series is separate). In the CT scan the specimen was completely solid, except L2, which had a few small pores (Fig. 4.10). In the FD curves, these pores had no effect. Because of the successful CT scan and high contrast in the images (necessary for image processing), the force-displacement curve of K1 was chosen to represent the solid PP tests.

The solid polypropylene FD curves show a difference in strain rate. The M-series was compressed at a different rate of 0.01s^{-1} , resulting in a stiffer response. As stated in previous research on the porous polypropylene (Sec. 1.2), strain rate sensitivity was expected, but with this test, it is evident, even with the small increase in rate. This result was not used further in this thesis, but it illustrates that this effect is present and should be included in a final study of the coating.

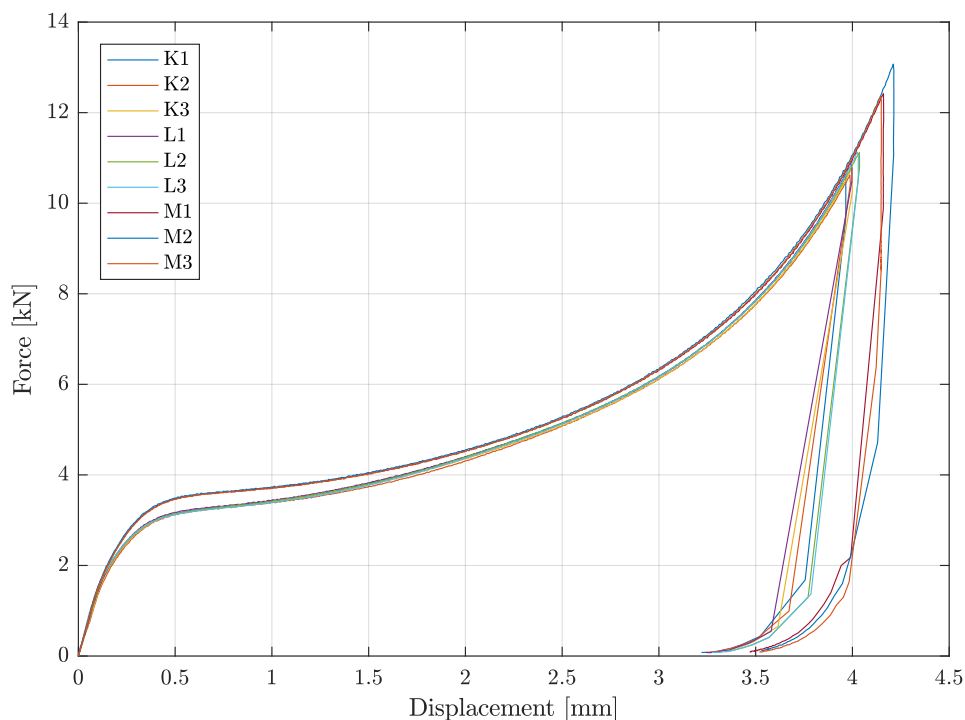


Figure 4.23: Corrected force-displacement curves of the solid PP specimens. Note that the curves group together in two groups. The M-series is the one with the slightly higher force due to the increased strain rate.

In Figure 4.25 the solid specimen K1 is compared to the porous specimens in the EH series. The FD curve of K1 is quite a bit above all the other ones. That implies that the pores produce a significantly drop in resistance - as expected considering the difference in mass. Furthermore, the shape of the curve is similar in the end (from about 2mm), but not before. EH2 is quite similar, but the level of force is much lower. The pore structure seems to have an effect on the yielding and shape of the curves in the start.

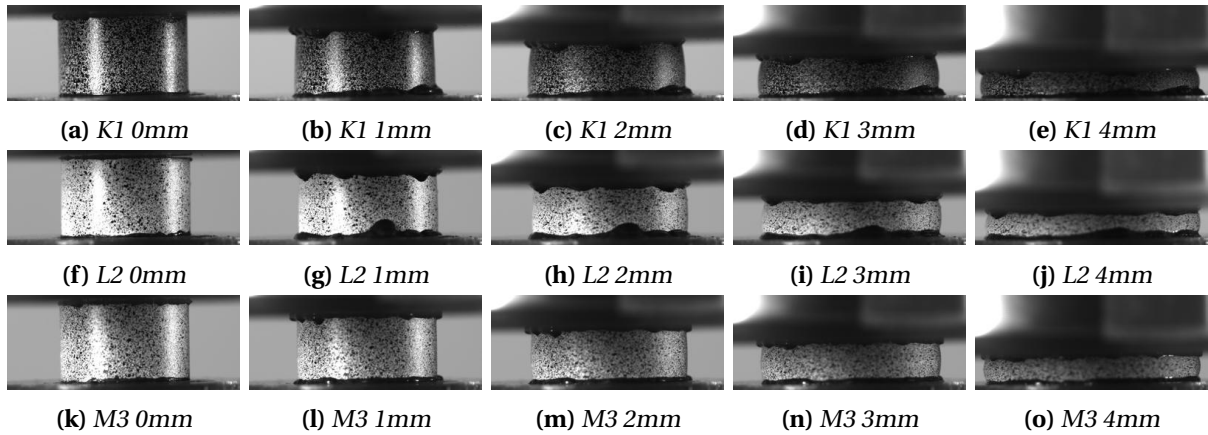


Figure 4.24: Results of solid PP compression tests. The specimens K1, L2, and M3 was selected to be representing the solid PP test images. These specimen were scanned, and all tests were relatively equal. Note the darker speckle pattern on K1, which may prove difficult for a possible DIC analysis, but is great for image processing (higher contrast to the background).

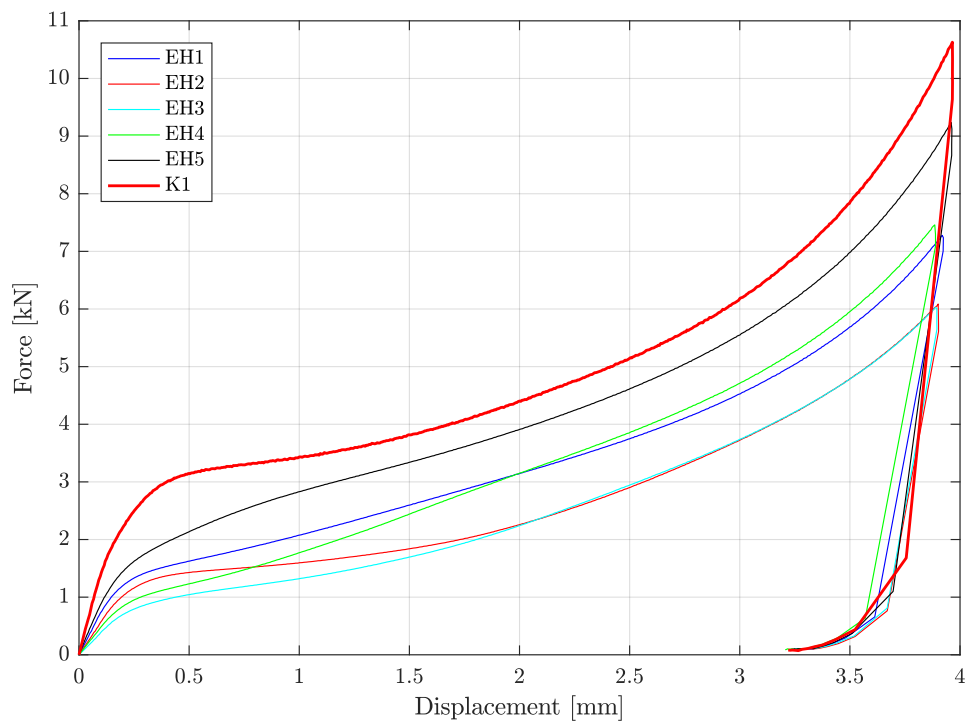


Figure 4.25: Corrected force-displacement curves of the solid K1 specimen and the porous EH series. The solid PP specimen is the thick red curve.

4.4 Summary and discussion

The goal of the experiments was to get a closer look inside the porous coating layer and investigate how the layer behave when subjected to uniaxial compression. The X-ray computer tomography revealed the pore morphology. The scanning of the solid specimens showed some pores in L2, but they seemed to have no effect on the FD curves. Not every solid specimen was scanned, but considering that the force-displacement curves were equal for all of them, they were assumed poreless. Since DIC proved difficult to employ, the FD curves were corrected by backwards linear extrapolation.

The results of the compression tests showed that the specimens had different deformation modes and strengths. All the porous specimens were weaker than the solid ones. The machine stiffness of the Instron system was determined to be negligible. The uniaxial compression tests on solid polypropylene with a higher velocity resulted in an increased force, which suggests that polypropylene is strain rate sensitive. Further investigation will not be conducted in this thesis.

Note that the solid polypropylene block was manufactured differently than the porous polypropylene used in the coating; the block was not extruded, which may affect the material properties. The potential difference was assumed to be negligible and was not further investigated.

Further discussions and analyses of the experimental results will be conducted in Chapter 5 with the aim of characterisation of the porous polypropylene.

Porous Polypropylene Characterisation

The preliminary studies (Chap. 3) resulted in a great numerical model of the steel, but a poor model for the coating. It was necessary to do a thorough study of the porous polypropylene layer because of the complex and varying pore structure. The experimental results were employed to characterise the coating.

5.1 Initial assumptions and simplifications

Because of the complexity of the porous polypropylene, several simplifications were made. In this section, an overview of initial assumptions, simplifications and choices about the coating are explained. The coating consists of a five-layer system of polymers (Fig. 3.5), where the porous polypropylene layer is the largest (ca. 80%) and most complex part. For this reason, the main focus was to characterise this layer. The other layers will not be considered herein.

To get a better understanding of the material behaviour of the porous polypropylene, the matrix material, pure polypropylene, must be investigated. It is a thermoplastic polymer with a high molecular weight [44]. In the coating solution [13] studied in this thesis, the PP is of the type BA202E [14]. This polymer type has a high impact strength according to the manufacturer. Some important material parameters (found in the literature) are shown in Tables 5.1 and 5.2. Note that temperature effects are not included in the scope of this thesis, but the thermal properties are useful to understand the reason why this polymer was chosen to be the thermal insulator. The low melt flow rate is ideal when applying the polymer coating to the pipe. Furthermore, the thermal conductivity is relatively low, resulting in a greater insulator.

The material behaviour of polymers is quite complicated as discussed at length in [44]. In general, polymers behave visco-elastically and visco-plastically. Phenomena like creep and stress relaxation are usually observed. Furthermore, polymers are pressure sensitive, and anisotropy is common. These material properties are not within the scope of this thesis, so they will not be accounted for. Although the experiments were uniaxial compression tests (not tension), a simple material model including pressure-sensitivity could be established with the use of the manufacturer's data (Tab. 5.1).

Table 5.1: Mechanical properties of solid polypropylene (BA202E) according to [26, 14, 27].

Density	Young's modulus	Tensile yield stress	Yield strain	Tensile fracture stress	Poisson's ratio
ρ	E	σ_Y	ε_Y	σ_f	ν
[kg/m ³]	[MPa]	[MPa]	[-]	[MPa]	[-]
900	1300	28	6%	30-40	0.30-0.35

It was assumed that the inhomogeneous morphology depended mainly on the radial coordinate [15]. However, there will be conducted analyses to investigate the anisotropy.

Table 5.2: Thermal properties of solid polypropylene (BA202E) according to [26, 14].

Thermal conductivity	Specific heat	Melt temp.	Melt flow rate
λ	c_p	-	-
[W/mK]	[J/kgK]	[K]	[g/10min]
0.2	1900	485-505	0.3

In the experiments (Chap. 4) the density of polypropylene was not measured. The value stated in Table 5.1 was assumed correct. A simple validation could be conducted to assure the number (900kg/m³). In Table 4.3 the solid specimen's measurements are stated. All cylinders were weighted to be 0.42g (+/- 0.01g). The mass can be calculated using the well-known equation

$$M = \rho V, \quad (5.1)$$

where M is the mass, and V is the volume of the specimen. The volume of an oval cylinder is $V = \frac{\pi}{4} D_a D_b h$, where D_a and D_b are perpendicular diameter measurements. With the use of these equations, the calculated mass and the density based on the measured data was found. The results are displayed in Table 5.3. All calculated masses are within the error space of the measured values, but very close to the edge (where the weight scale would measure 0.44g). The calculated densities are all a bit lower than the original value (about 17.8kg/m³ lower at average). This result strengthens the validity of the manufacturer's value of the density of the BA202E polypropylene, and it (900kg/m³) was used herein.

Table 5.3: Calculated mass and density for each solid specimen using Eq. 5.1 and the values from Tables 4.3 and 5.1.

Specimen	K1	K2	K3	L1	L2	L3	M1	M2	M3
Mass [g]	0.4278	0.4298	0.4283	0.4287	0.4277	0.4282	0.4285	0.4286	0.4288
Density [kg/m ³]	883.5	879.5	882.4	881.7	883.7	882.9	882.2	881.9	881.6

In the characterisation process, Matlab was utilised as the tool to do the image analyses of the CT slices. The slices were 2D images of the coating. It was assumed that the porous polypropylene could be characterised by analysing the slices. However, analysing the morphology of the pores in 3D could yield more accurate data.

The curvature of the coating was not accounted for in the image analyses. The porous specimens (1-5) are quite small (Tab. 4.1), so the effect of the curvature on the results of the analysis was assumed to be negligible. The block, however, is a lot larger, and should, therefore, account for this. As a remedy, the analysis was conducted on a small extracted part of the slices of the block.

5.2 Pore morphology

The X-ray computed tomography image slices were used to get a better understanding of the pore morphology and to characterise the porous polypropylene layer. Image-processing in Matlab R2016b [30] was employed to extract information from the slices. Matlab was also used to plot the pores in 3D so that the reader can get a better understanding of the pore structure. The CT image slices of the block and specimens were analysed with Matlab's binary image and region properties functions. See Section 2.5 for more information about the image processing tools used in this thesis.

5.2.1 Realitive density

When characterising something that is porous, an important statistic is the relative density (Sec. 2.4). The RD of the coating solution varies in the porous polypropylene layer [12, 15]. A more accurate characterisation of the layer was attempted with Matlab's image processing toolbox. The block was ideal for this purpose. Here the entire coating solution is present and continuous in the CT images, while the specimens were quite small and did not represent all of the coating layers. The RD curve (as a function of the radial coordinate) was established by finding the reduction in area in each top-down (Fig. 4.6) image slice. The matrix material (PP) was assumed have a constant density. The relative density was then equal the area reduction.

The top-down slices of the block are not at the same radial coordinate in the entire image, because of the curvature of the coating. See Figure 5.1 for more details. The pore statistics should depend on the radial direction only for simplicity and the assumption that the pore structure varies little in the other orientations. The entire slice could therefore not be used. The remedy for this problem would be a re-slicing so that all pixels in the image were taken from the same radial coordinate. Another, more straightforward, approach was adopted; only a small part (square) in the middle (Fig. 5.1) was used in the image processing. The result would be rougher, but still an accurate measurement of the area reduction.

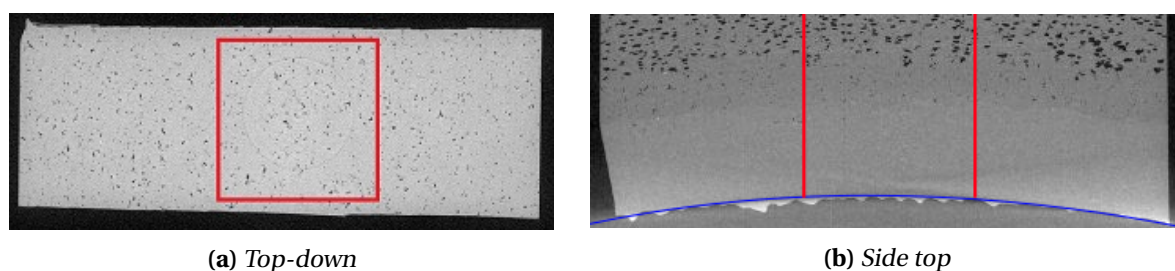


Figure 5.1: The top-down CT image slices were cropped at the centre, and a square image were extracted (inside red lines). The curvature of the block is clearly visible in (blue line).

The CT image slices were uncompressed raw image data on the "tif" file format. A method to distinguish the pure polypropylene material from the pores and air was essential. There were only two possibilities, either polypropylene or nothing (air), so a binary image representation (Sec. 2.5.1) was ideal. When working with binarization of many images, a problem arises. Because of the different grayscale intensities (the grayscale histogram shifts), a constant threshold level would produce a wrong binary representation. The problem was avoided with the use of an already implemented algorithm in Matlab, called Otsu's method [29]. This approach automatically finds the threshold level based on the

histogram. However, another problem presented itself; the noise in the CT images caused the part with very few pores (almost pure PP) to be wrongly binarized. That happened because of small differences in the grayscale values causing Otsu's algorithm to set the threshold value too high because there were too few dark pixels. See Figure 5.2 for an illustration of the problem. In the figure the threshold values are normalised; 1.0 is the grayscale value of white, and 0.0 is the grayscale value of black. The issue was avoided by setting a max value of the threshold level.

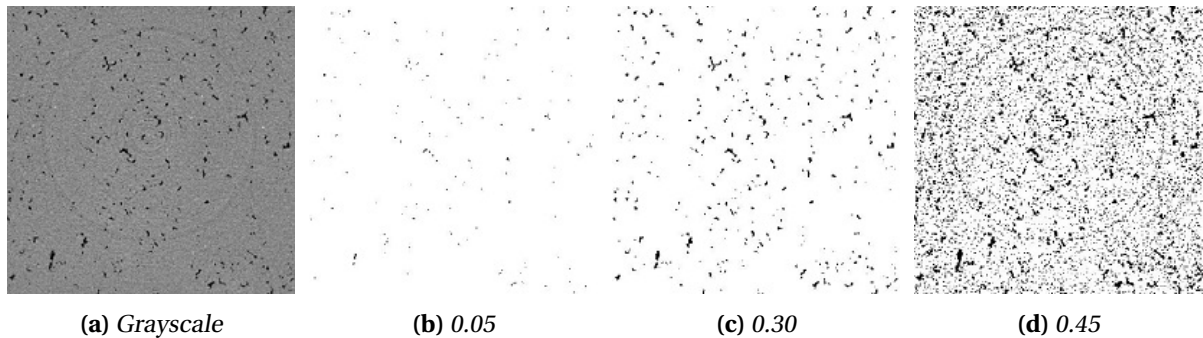


Figure 5.2: Binary images (b, c and d) created by the respective threshold value from the grayscale image (a). The image is cropped from the block CT top-down slice. Note that the threshold value of 0.30 works quite well at capturing the pores, but the other two do not.

The cropped image slices (Fig. 5.1) were processed with Matlab, and binary images were made. The relative density was then easily calculated by summing the on-pixels (in this case the on-pixels represent the matrix material) and dividing by the filled area in the form of pixels. The filled area was simply, because of the square form of the image, the number of pixels at the sides squared. Note that the term relative density must be used correctly. The coating solution has several layers of different materials (densities), and the RD measures the density compared to that material (not one matrix material density in the entire coating solution). Another way to characterise the coating the same way is porosity, which is simply $1 - RD$ (Fig. 5.3b). This term may be more suitable since it states where there are pores, and the matrix material is irrelevant. In previous work on the coating the RD term was used [15, 16], and it will be used herein as well.

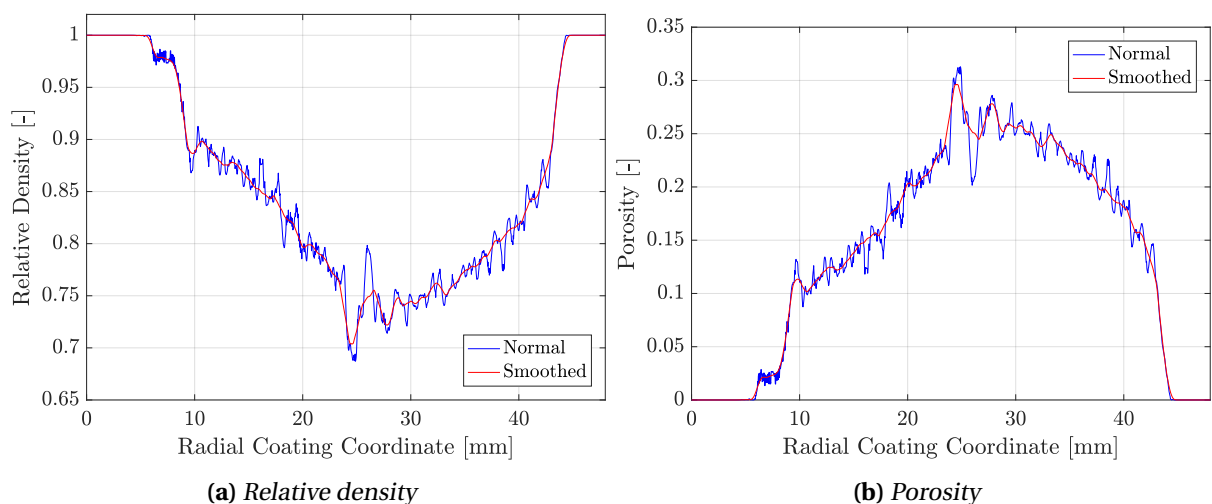


Figure 5.3: Coating relative density (a) and porosity (b) with smoothed curves. Note that the radial coordinates here have the origin at the edge of the steel pipe.

Figures 5.3a and 5.4 show the calculated RD curve of the coating solution. First of all, notice that the non-porous layers have a relative density of one, which was expected (no visible pores in the CT images). Second, the transition zone (Sec. 4.2.2) is present. In this zone, the RD is at its lowest. At either side the curve is different, i.e. the relative density is not symmetric about the middle. The left side seems to curve the other way. Third, the ends of the porous PP layer have different RDs. The start of the layer (lowest radial coordinate) has an RD of about 0.98, and at the other end, it is 1.0. The reason for this is the many small pores at the start.

When comparing the curve in Figure 5.3 to the curves in [12, 15], the similarities seem to be relatively good. Another validation of the RD was to compare the curve with a representative CT image slice. One such comparison is shown in Figure 5.4, and the correlation appears to be great. Remember that the method of finding the RD was a cropping of the block, which is a source of error. Also, the cropped image represents quite a small portion of the coating. With a larger area, the error of random differences would likely be reduced. This error is present in the RD curve; in Fig. 5.3a there are oscillations due to the small area of the cropped slice. The smoothed curve resembles the true relative density because the oscillations were assumed to be incorrect.

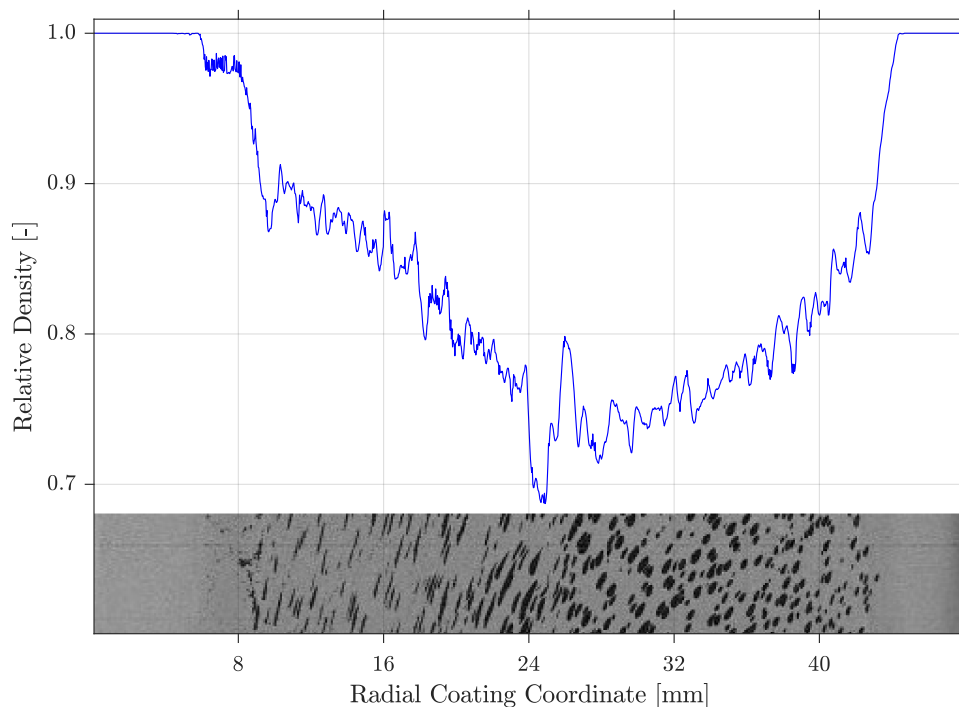


Figure 5.4: Coating relative density with corresponding CT side left slice. The curve correlates well with the image.

5.2.2 Other characteristics

The relative density curve had been found in the radial direction, but what about the other ones? As done with the top-down slices, cropped images in the side left (axial-radial plane) and side top (hoop-radial plane) directions were used to get the RD and other statistics depending on the hoop and axial direction, respectively (see Fig. 4.3 for an illustration of the directions). Note that the cropped part covered the entire porous layer. Several properties were extracted from the block, including relative

density, the number of pores, pore size and pore orientation, all as a function of the coordinate of the respective direction. The statistics were found by the use of Matlab's region properties function (Sec. 2.5.2). The images in the hoop direction did not take into account the curvature of the coating. Since the block was small, the error because of the curvature was assumed to be minimal. The results of the analyses are shown in Figure 5.5. Note that the length of the block in the other directions are lower than the radial, so the curves are not equal in length.

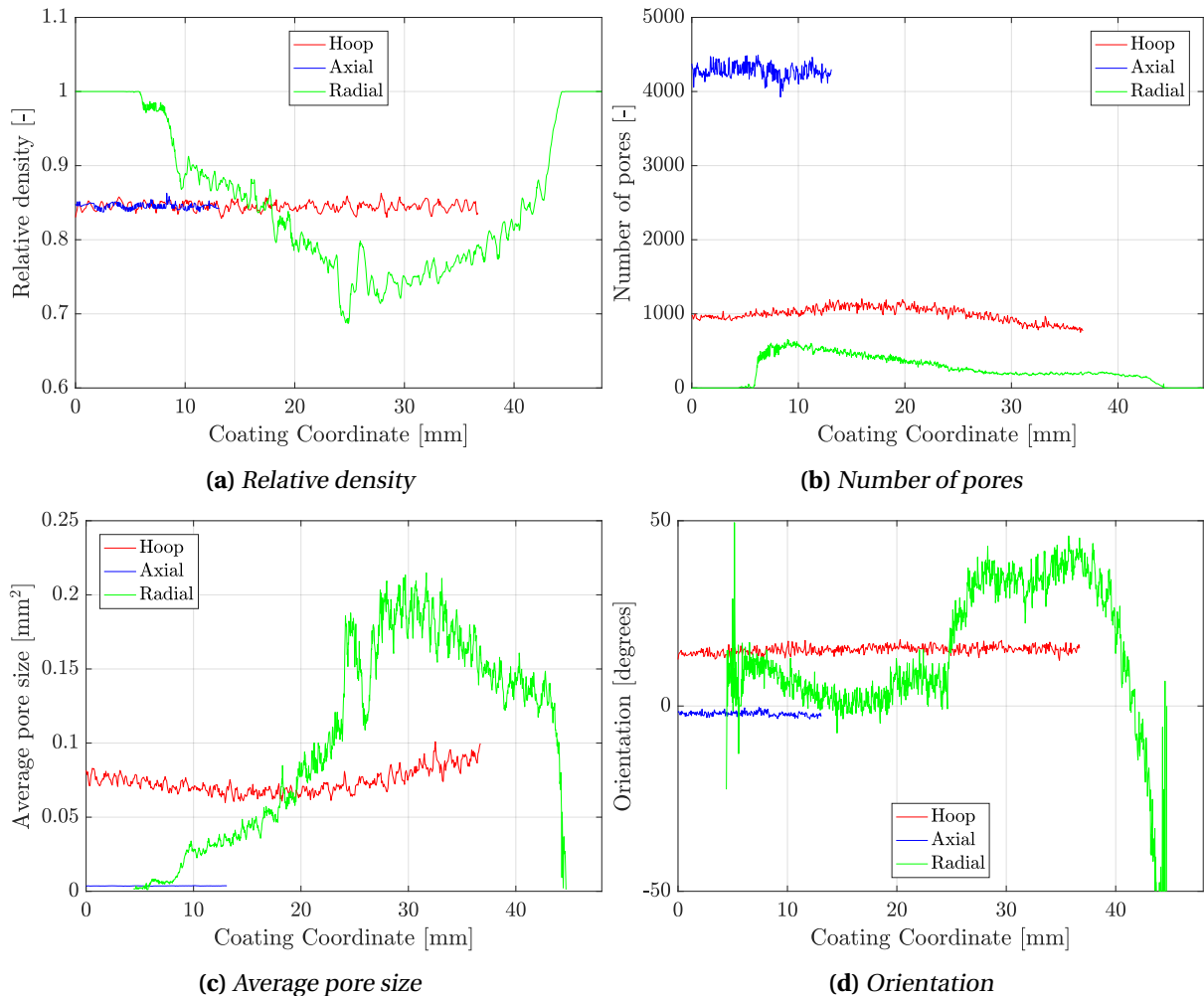


Figure 5.5: Results of the analyses of the block in all three directions. The coating coordinate is relative to its direction. See Figure 4.3 for measurements and directions. Note the slight curvature in the hoop direction. Also, the orientation is the average angle of orientation of the pores.

The plots in Figure 5.5 show several interesting properties, but first, the error of the results must be discussed. Note the curvature in the red curves (hoop). That was assumed to be because of the images not taking into account the curvature of the coating. If so, the curve would be horizontal (like the axial direction's curves). Strictly speaking, the images followed the horizontal axis, not the hoop, but the difference would be small, because of the short length. Also, the number of pores statistics are not comparable to each other. The axial direction used an image a lot larger than the other two. The curves still illustrate change or no change along the respective axis. Note that this analysis was in 2D space, meaning that the number of pores corresponds to a 2D image. The number does not reflect the actual number of pores (one would need to analyse in 3D to do that, which was not conducted in this thesis).

In Figure 5.5 there was observed an important characteristic of the coating. The pore morphology in the axial and hoop directions show little variance, i.e. the pore structure seems to depend on the radial coordinate only. The curves of the other directions are relatively horizontal and flat, meaning that there was no significant change as one moved in that direction. Furthermore, the radial direction shows a lot of varying properties. The curves representing relative density, number of pores (in 2D), average pore size, and orientation are highly non-linear and change significantly depending on the radial coordinate.

The average pore size is larger in the hoop direction than the axial. That made sense because the pores clearly look different in the two directions (Fig. 4.9); the pores are not shaped like a circle, but an ellipse pointing in the hoop direction. Looking at the pores in 3D in Figure 5.7, the shape is apparent. The average orientation (in degrees) of the pores are different in the three directions as well. Notice the difference in the relatively constant orientation in the axial and hoop directions. When looking at the coating axially, the pores are shaped like horizontal ellipses (at average), while in the hoop direction the pores are at a slight angle (about 20 degrees).

To further analyse the porous coating layer, one image was chosen for the hoop and axial direction (in the middle of the block), and the pores in said images were colour-coded to represent a certain characteristic. The colour map used was chosen because of the high contrast and few colours. This way possible patterns could be observed due to the distinct differences representation of the respective property. In Figure 5.6 the pores are colour-coded after pore area, orientation and major axis length. Note that major axis length is the length of major (longest) axis of a fitted ellipse. It is not just horizontal length, but the longest length of a pore.

The colour-coded images illustrate some interesting facts about the coating. The first, and most important, is the transition zone, observable in both directions. The colours are different at the top and bottom half. Another observation was that in the hoop-radial plane the largest pores (area) are found in the top half, but in the axial-radial plane it is the other way around. That means that the long and flat pores have a high area (in this plane). The long and flat shape of the pores is highlighted in Figure 5.6h.

In Figure 5.6g, the orientation of the pores is colour-coded in the axial-radial plane. The pores are "stretched" in the axial direction, and the orientation angle increases as the one moves upwards (radial direction), while the major axis length decreases. The reason for the noticeable transition zone is hard to determine, but it was assumed to be caused by the extrusion process during manufacturing (Sec. 3.2.1).

5.2.3 Three dimensional representation of the pores

A complete study of the pore morphology in 3D space was not conducted in this thesis but is recommended for further work. On the other hand, a simple method in Matlab was used to render a 3D model of the pores. This way the reader can understand the complexity of the morphology and observe the actual form of the pores. In Figure 5.7 a square column of the block (in the radial direction) was extracted and plotted alongside five pores found in different radial coordinates. These pores are displayed at various viewing angles. The method used to plot this was to make a patch of isosurfaces built from the binary images of the top-down slices [30].

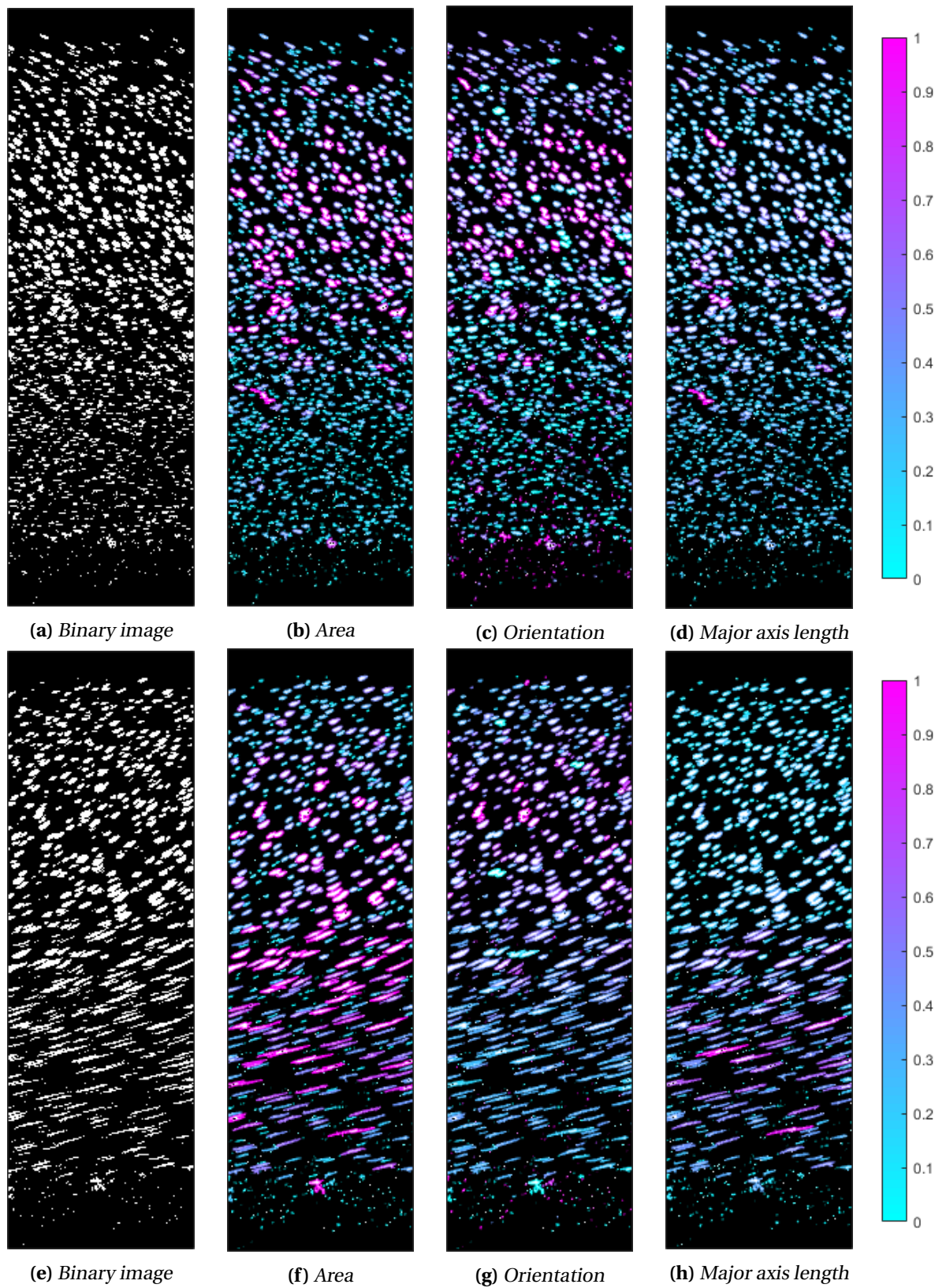


Figure 5.6: Image analysis of a side top slice (hoop-radial plane) at the top row and image analysis of a side left slice (axial-radial plane) at the bottom row. The colours correspond to the values in the colour map displayed to the right side. A value of 1 means that the respective characteristic is at the max value, and 0 means lowest.

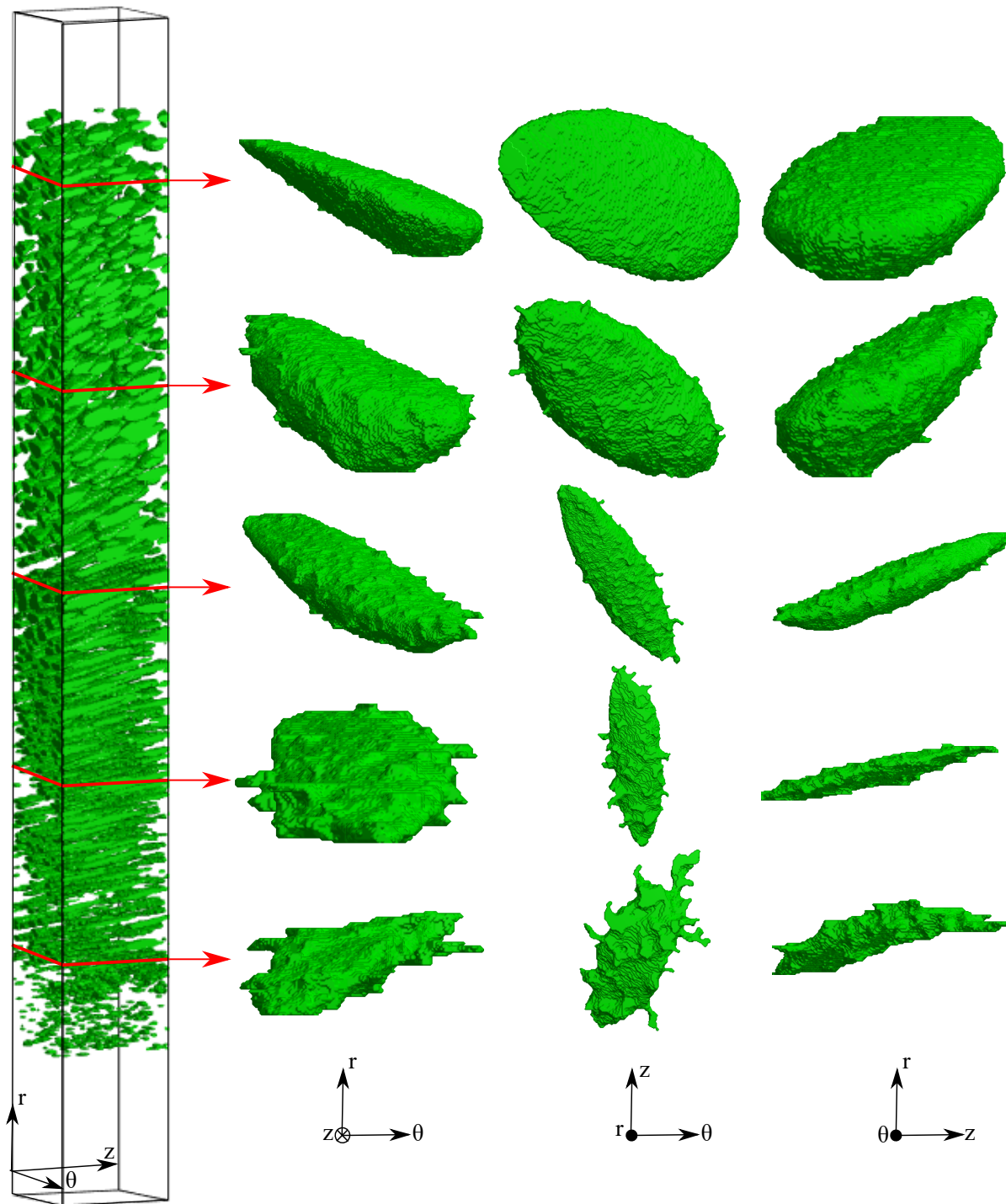


Figure 5.7: 3D representation of the pores in the coating. To the left, a thin and tall tower of the coating is extracted. The black frame illustrates the entire coating solution (all layers), and the green bubbles are the pores. The red line illustrates where the pore was extracted. Each row shows the same pore but at different angles. Notice the significant change in the shape of the pores; as one moves down in the radial direction, the pores vary in size and orientation and become flat and veinier.

Although the Figure 5.7 was for illustrative purposes, some useful information could be extracted from it. The actual shape of the pores are hard to determine from 2D slices, but in 3D the true shape reveals itself. The pores start as large droplets but are transformed into long and flat pores with veins. Notice the veins are gradually more observable as the lower one moves in the radial direction (down in the figure). Also, note the change in orientation, not only in the axial-radial plane (as found in Fig. 5.6), but in the axial-hoop plane as well (middle column of pores).

5.3 Characterisation of the specimens

Now that several properties about the porous polypropylene have been established through 2D image analysis of the block, the specimens could be characterised to investigate a potential difference between the sample series (EG, EH and EI) and find a more accurate measurement of the weight of the specimens. At the same time, the characterisation of the specimens could prove useful when analysing the uniaxial compression tests.

An immediate problem was encountered when analysing the specimens; the same technique used to analyse the block by cropping out a square could not be used because of the round ellipse form of the top down slices of the samples. A large part of the rectangular image was just air. Therefore, when the binary image was created so that the pores are represented as the on-pixels (ones), the large part of surrounding air was also set to on. A cropping was necessary. To crop out a circle of the same size in every image slice would be wrong, because the specimen did not have its centre at the same spot in the slices. Another method was employed as demonstrated in Figure 5.8. Note that an algorithm was developed to crop an ellipse with the dimension corresponding the bounding box.

The area reduction was still simple to calculate (count the pixels that represent polypropylene and divide by the filled area of the ellipse), but the other statistics (number of pores, pore size, etc.) required that the pores alone be the on-pixels. The reason was so that the region properties method in Matlab would include the open pores at the edge. The binary image in Figure 5.8c would not work, because the edge pores are not included, but the cropped version does (Fig. 5.8d).

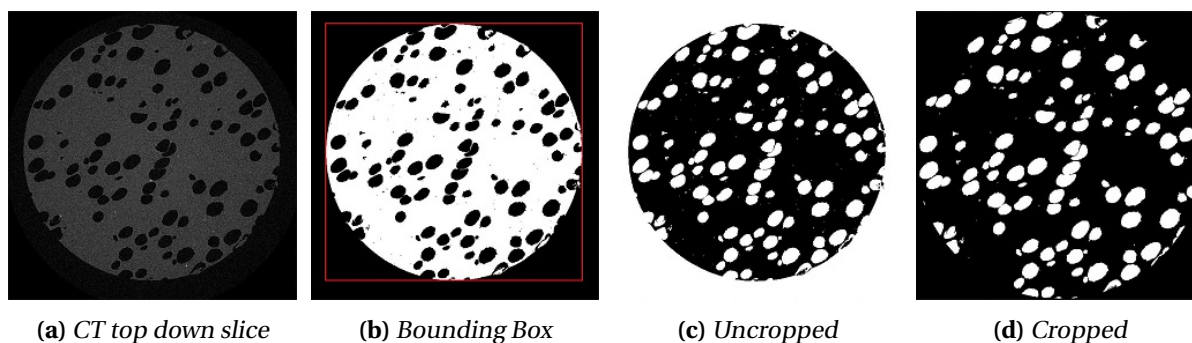


Figure 5.8: Top down image slice in the middle of EH2. The CT image (a) was transformed into a binary image (b), and the bounding box was found. Then the binary image was inverted (c) and cropped according to the bounding box (d). The white pixels are the on-pixels.

Several properties were extracted from the specimens, including relative density, the number of pores, pore size and pore orientation, all depending on the radial coordinate. That was conducted by running the analysis on 500 images for each specimen (originally about 1000 images). The results are shown in Figures 5.9 and 5.11.

As discussed in Section 4.1 the missing part of the porous PP between the specimen were assumed equal. The end specimens (1 and 5) were cut at the end of the foam layer, so the missing space is between the middle specimens. In Figure 5.9 it was observed that specimens 1 and 5 fitted great, and specimens 2, 3 and 4 fitted relatively well. Furthermore, it was noticed that the specimens' RD curve is more varied - the peaks are higher. That is reasonable since the area of the slice in the samples (ca. 78mm^2) are smaller than the cropped square slices in the block (ca. 141mm^2). Therefore the large

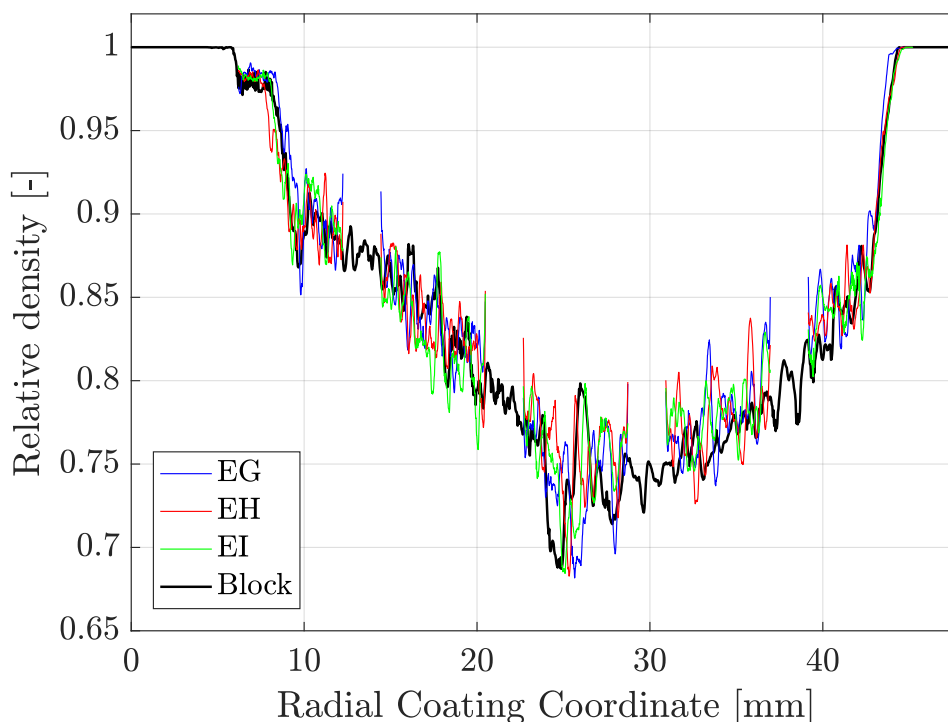


Figure 5.9: Relative density of the coating where the specimens are compared to the block. Note the separation in the specimen curves. A value of 2.1875mm was used as the separation length.

pores in the specimen will play a much larger role in the resulting RD curve. The results of the relative density curves are satisfactory.

The RD curves could be used to calculate the mass of the specimens. Remember that the measured weights of the cylinders were quite inaccurate, because of the readability of the weighing scale (0.02g), but they can validate the calculated masses to a certain degree, which would then verify the RD curves. By using many of the CT images and assuming that the matrix density is uniform and equal to 900kg/m^3 , an accurate estimation of the mass of the specimens could be established. The mass was calculated by Eq. 5.2 (see App. B where the equation is derived) where ρ_s is the matrix density, ρ^* is the relative density, M is the specimen mass, A is the cylinder surface area (constant), dh is the slice height (constant), i is the increment (slice) index, and n is the total number of increments.

$$M = \sum_{i=1}^n \rho_s \rho_i^* A dh \quad (5.2)$$

There were 500 slices per specimen used to find the relative density curve, so $n = 500$ and $dh = 0.0121\text{mm}$. The polypropylene density was set to $\rho_s = 0.0009\text{g/mm}^3$, and the cylinder surface area was 78.54mm^2 . By the use of these values in Equation 5.2, the mass of every specimen was calculated and plotted as shown in Figure 5.10. It was observed that the mass of each specimen number (1-5) was very similar and close to the measured values, all except number 2, where the specimen weights were a bit lower, but still within the error space. The measured values were quite poor in accuracy, as illustrated by the red rectangles in the figure.

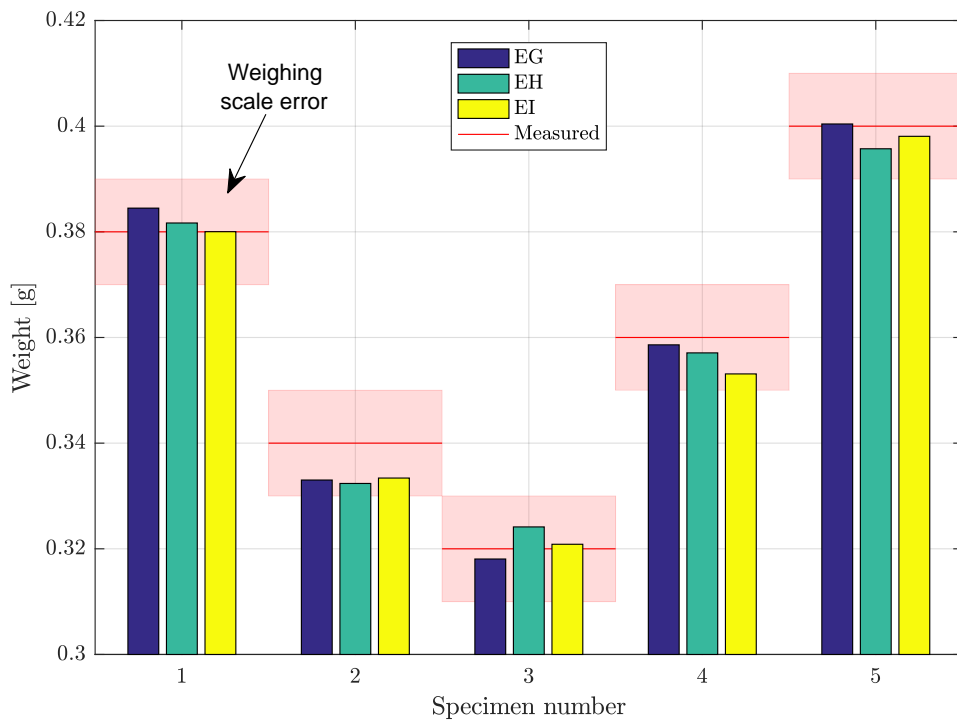


Figure 5.10: Calculated and measured specimen weights. The weights were calculated from the respective RD curve for each sample. The red lines are the measured weights with its error space (rectangles). Measured values were taken from Table 4.1.

What follows is the results of the rest of the statistics. The accuracy of these results was assumed reliable, due to the satisfactory RD results. In Figure 5.11 the statistics of relative density, the number of pores, pore size and orientation are shown. It was observed that the curves of EG and EH match quite well, but EI varies a bit, especially the orientation of the pores. As discussed before, the EI series seemed to be placed differently in the CT scanner (there was no tape to determine the orientation of the slices), which explains the significant difference. The curves support each other when validating the results. When the number of pores is getting higher, the relative density is becoming higher as well. For this to make sense, the pore size must reduce significantly, which it does. Also, note that the number of pores of EI1 (right side) is enlarged compared to EG1 and EH1, but the average pore size is reduced to account for this, resulting in a similar RD curve.

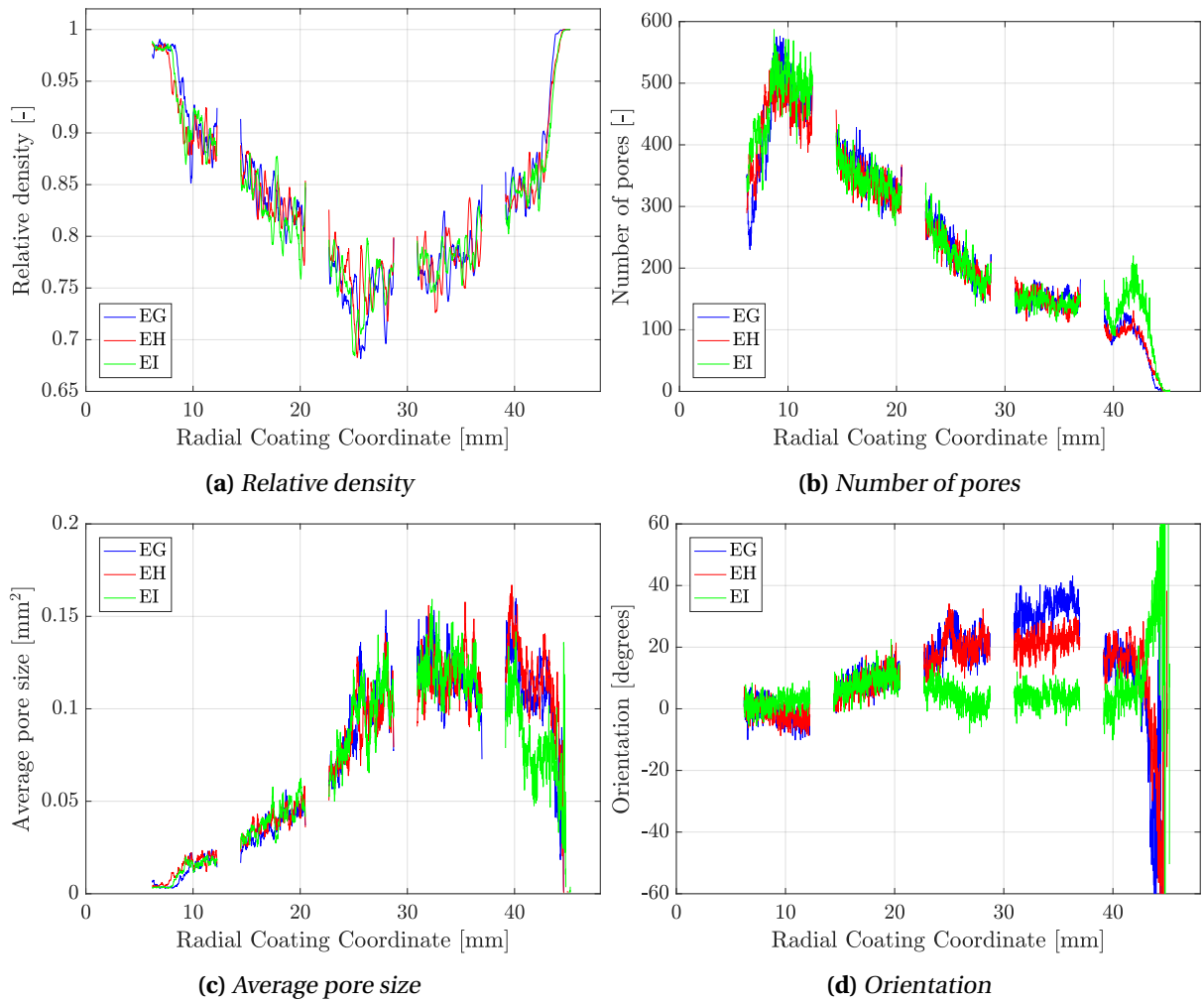


Figure 5.11: Statistics on all specimens found by Matlab image processing on the 2D top down slices. Space between specimens is 2.1875mm. Recall that specimen 1 is to the right. Note that the orientation is the average value of the orientation of all pores at that coordinate and that 0 degrees are the horizontal direction of the image.

5.4 Mechanical properties

The several properties of the porous polypropylene layer had been identified by analysing the CT image slices. The next step is the mechanical properties. In the following, the results of the compression tests will be interpreted and employed to characterise the coating further. A material model will be calibrated for the solid PP as well.

5.4.1 Polypropylene material model

To characterise the mechanical properties of the porous coating layer, the matrix material (solid polypropylene) should be investigated. The solid specimen compression tests were conducted to compare to the porous ones, but in addition, a simple material model could be calibrated. The material model is the stress-strain relationship. This model was necessary for the later numerical studies as well as an important part of the characterisation.

From the experiments on the solid polypropylene specimens, the force-displacement curve is given, as well as images during deformation of the specimens. This data need to be processed correctly to get a material model. The engineering data could be found by using the Equation 5.3 where F is the force and A_0 is the initial area. However, it will be incorrect as the deformation is large. Therefore, the true stress and strain should be found; the values depend on the true area, A , i.e. Equation 5.4.

$$\sigma_e = \frac{F}{A_0}, \quad \varepsilon_e = \frac{\Delta L}{L_0} \quad (5.3)$$

$$\sigma = \frac{F}{A}, \quad \varepsilon = \ln\left(\frac{A}{A_0}\right) \quad (5.4)$$

DIC proved difficult because of the poor focus (blurry) of the specimen in the edges, so image processing and edge tracing were conducted with the use of Matlab to determine the true area. The simple assumption of a perfectly circular cross section was made, because of the camera setup (setup 1). With two cameras at a 90-degree angle, it would be sufficient for an elliptical cross section (such as setup 2 in Fig. 4.12).

The method used to determine the diameter was binary imaging (Sec. 2.5.1), with a threshold level sufficient for distinguishing the specimen from the background. To make the process of finding that level easier, the contrast between the background and the specimen should be as high as possible. For this reason, the specimen K1 was chosen (in Figure 4.24 the contrast advantage of K1 is evident). As mentioned, the transition between the background and the specimen in the images was blurry, because of the focus of the camera. The threshold level must be chosen carefully to get the correct diameter measurements. See Figure 5.12 for an example of a row in an image of K1. Here the row is illustrated by the cyan stapled line while the grayscale variation of the image row is the blue one. Note that two different threshold levels were chosen; one value at each side of the specimen was set, because of the slight difference in the grayscale value of the background. The entire edge of the specimen was traced by moving the image row vertically so that the horizontal image coordinates

would be tracked and the longest diameter could be extracted. That yields the highest true area, and therefore the lowest stress. Note that because the grease covered the specimens at the top and bottom, the diameter could not be measured there. However, the longest diameter was found around the middle because of the barrelling effect caused by friction.

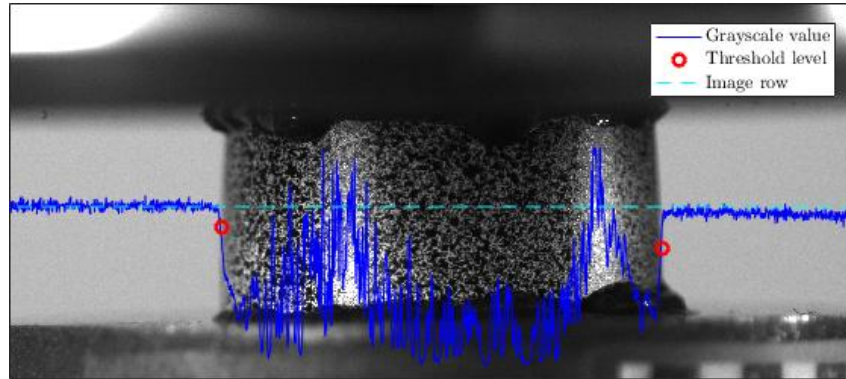


Figure 5.12: Method for determining the diameter of a specimen during compression. The grayscale variation (whole line) in an image row (stapled line). The threshold levels on either side of the specimen are illustrated by the red circles.

The true stress and strain were calculated by the use of the true area (Eq. 5.4). The resulting curve was quite rough; the strain was going back and fourth. The reason for that was assumed to be the varying brightness of the images while the threshold level was constant. A smoothing operation fixed that issue. Based on the force-displacement curve of K1, the engineering values was also calculated with Equation 5.3. Both curves are presented in Figure 5.13, with the plastic strain curve as well. The plastic strain was found by subtracting the elastic strain, i.e.

$$\varepsilon^{pl} = \varepsilon - \frac{\sigma}{E} \quad (5.5)$$

where ε^{pl} is the plastic strain, and E is Young's modulus. The modulus was determined to be 1125MPa. At yielding (first peak), the true stress is 37.3MPa. There is non-linear (inelastic) behaviour before this point, so for an accurate description of the material behaviour, the yield point was set to 14.2MPa when used in the numerical models.

A major problem when calibrating a material model based on compression tests on cylindrical specimens is the friction. Friction forces were present (barrelling of the specimens), so a correction was needed. However, there was no way of determining the actual effect of friction on the true stress-strain relationship. To solve this inverse modelling was employed, which means that the final material model was calibrated by optimising it so that the force-displacement curve of the simulation was equal to that of K1's. First, the true stress-strain curve was extrapolated. The plastic strain only reached a little over 1.0, but in the numerical studies on the porous specimens, the plastic strain was assumed to approach a higher value. Therefore, the curve was extrapolated with a third degree polynomial fitted to the end. Then, five material models were created by reducing the stress to account for the friction. Each of these models was used in a simulation of the compression test of specimen K1 (with Young's modulus equal to 1125MPa), with friction coefficients (FC) 0.000, 0.025, 0.050 and 0.100.

To simulate the compression test an axisymmetric numerical model was established in Abaqus. The

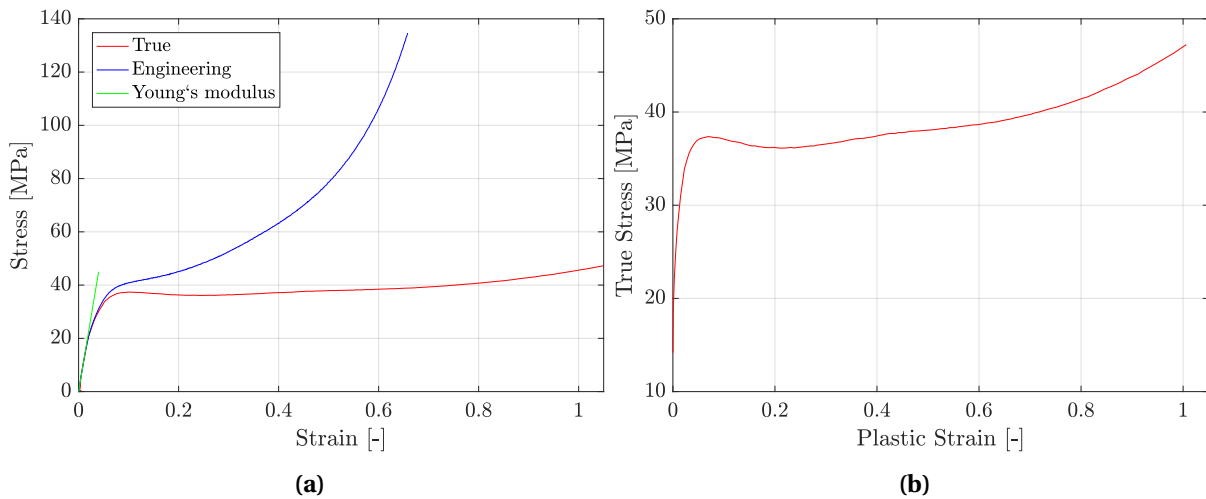


Figure 5.13: Engineering and true strain-stress curves for polypropylene. Young's modulus was found to be 1125MPa. The engineering values are too high because they do not take into account the change in the area. The true stress-plastic strain curve shows the yielding at 37.3MPa, but non-linearity start before.

model was created with 4-node bilinear axisymmetric quadrilateral (CAX4) elements. The elements had an approximate size of 0.25mm, giving a total of 480. The model was created with the exact measurements of specimen K1 found in Table 4.3. The material parameters were set to 9×10^{-6} tonne/mm³ for the mass density, 1125MPa for Young's modulus and 0.3 for Poisson's ratio, while. The plastic parameters (table of yield stress and corresponding plastic strain) were set as the different material models. Two rigid plates were included to represent the indenter and the support, where the indenter was configured to move a length of 4mm, while the support was fixed. For the interaction, the surface-to-surface algorithm was used with the indenter and the support as the master surface. The friction parameter was altered to determine the correct value. The simulation was executed with a static general step, with the non-linear geometric option applied.

The results of the material model calibration and inverse modelling is presented in Figures 5.14 and 5.15. The results are satisfactory, and a material model was created for the polypropylene. The final model used a friction coefficient of 0.025.

Polymers are in general anisotropic, pressure-, temperature- and rate-sensitive, with inelastic tendencies (Sec. 5.1). The material model calibrated here is an isotropic elastic-plastic material insensitive to temperature, strain rate and pressure. Because the material model was found to characterise the polypropylene and to be used in simulations of the porous specimens under compression, the model was sufficient. The temperature and strain rate was the same for the solid and the porous samples during compression tests and is therefore not needed in the material model.

The final calibrated material model (true stress - plastic strain curve) was found by inverse modelling, image processing and extrapolation. The curve has the properties of general polymers [44]. The inelastic part before the yield at the peak, and then a small softening, followed by a slow constant increase in stress. After about 0.8 plastic strain the material hardens as shown by the rapid increase in stress. It was also noted that the stress-strain relationship shows similarities to elastic-plastic foams under compression (Sec. 2.4).

A simulation confirmed the validity of the model, but only to about 1.0 in plastic strain; the extrap-

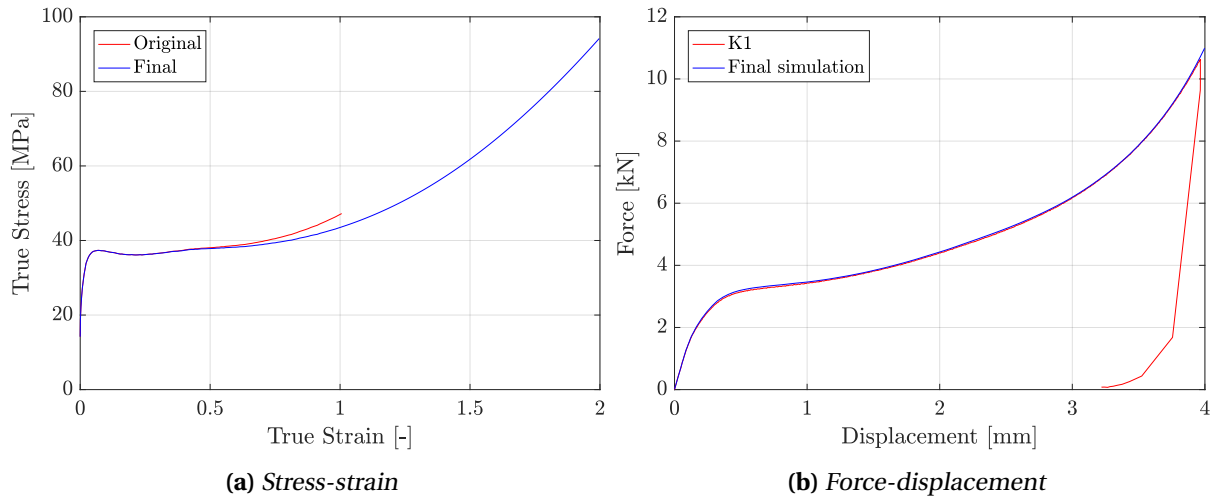


Figure 5.14: Final material model compared to the original (a) and the simulation results of the model compared to K1 (b). The difference in the final model is present at the end, where the friction forces are large. The simulation gave a very satisfactory result.

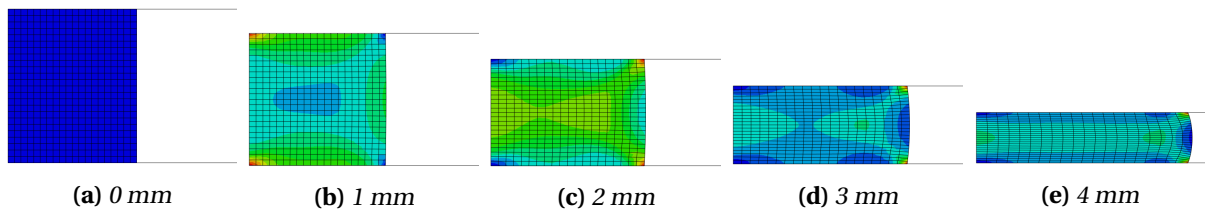


Figure 5.15: Deformation of the numerical simulations of K1 at different stages. Note that only the right half of the axisymmetric model is illustrated. The colour-map correspond to the von Mises stress.

olated part was impossible to validate. However, in the numerical studies, the importance of the extrapolated segment is investigated.

In Table 5.4 the calibrated material properties of polypropylene are stated. The values found here somewhat correlates with the values found in the literature and the information provided by the manufacturer (Tab. 5.1). These are not the same as the model calibrated here, but remember that the values are from tension tests. A difference in tension and compression was expected [44]. The compressive yield stress is 1.33 times larger than the tensile strength (tension yield stress). The difference is substantial, but within reason when considering polymers [45].

Table 5.4: Mechanical properties of solid polypropylene (BA202E) for compression.

Density	Young's modulus	Yield stress	Yield strain	Poisson's ratio
ρ [kg/m ³]	E [MPa]	σ_Y [MPa]	ε_Y [%]	ν [-]
900	1125	37.3	6.8	0.3

The test setup and identification procedure the manufacturer used was according to the ISO standards (527-2 for the yield stress and strain). The rate of deformation was larger for the tensile tests

(50mm/min) than the compression tests (0.36mm/min), which means a higher strain rate. Polypropylene was assumed to be affected by strain rate (Sec. 4.4), which may explain the difference in Young's modulus and yield stress. The temperature difference during each test could also affect the results, but the temperature was assumed to be room temperature (23°C) for both compression and tension tests.

By assuming that the strain rate and temperature effects were negligible, the difference in yield stress in tension and compression could be used to calibrate a second material model that include pressure sensitivity i.e. linear Drucker-Prager (Sec. 2.1.4). The assumption is perhaps too great to make, but this model was considered to be more representative when conducting tension simulations on the re-created porous specimens.

The Drucker-Prager yield criterion was calibrated by the use of Equation 2.12 which resulted in a friction angle (β) of 23.135 degrees and a pressure sensitivity (α) of 0.14242. The criterion was used in the same axisymmetric models as the first material model, but with different tabulated hardening parameters in Abaqus. The yield data was adjusted down in the end (Fig. 5.16a), because of the friction. The force was too high with the original material model; the friction resulted in a higher hydrostatic stress state, giving an elevated force. The new model still used 0.025 as the friction coefficient. Inverse modelling was employed so that the FD data matched the experiment (Fig. 5.16b). Note that Abaqus uses extended Drucker-Prager yield criterion, but by setting the flow stress ratio equal to 1, and the dilation angle equal to 0, the pure Drucker-Prager model is achieved. This means that the yield surface is the same as the von Mises yield surface in the Π -plane, and that the material is incompressible (no volume changes).

The axisymmetric model was also modified to simulate a tension test. The rigid plates were removed, and a velocity was added to the top surface to deform the model 4mm, while the bottom surface was fixed. The results of the compression and tension simulation are plotted and compared to the experimental data of K1 in Figure 5.16b. Note that the fracture properties was not calibrated in this thesis.

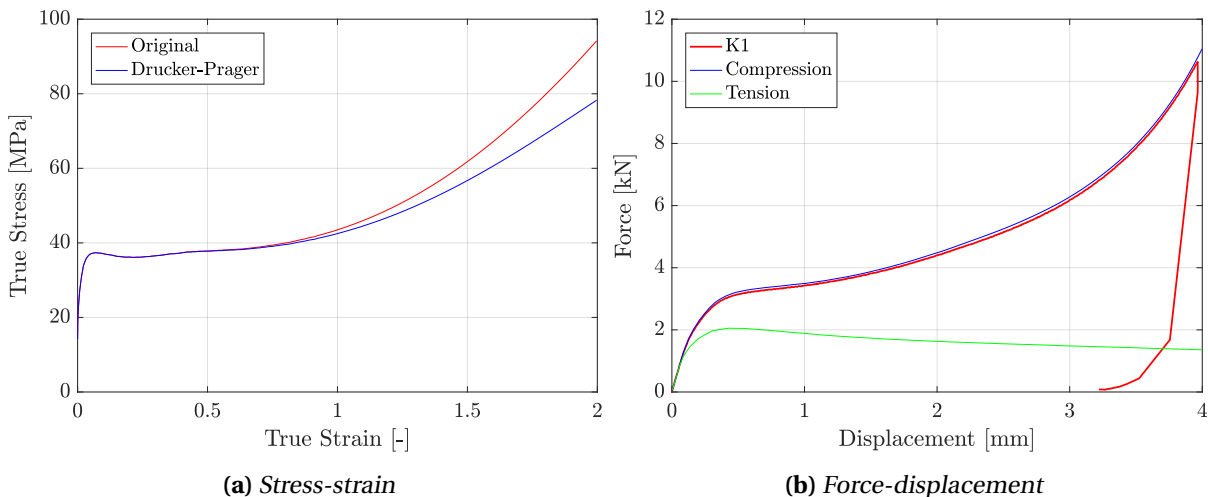


Figure 5.16: Drucker-Prager material model results.

5.4.2 Transverse expansion

The inspection of the coating has revealed significant variations in the underlying pore structure. To further investigate how the pore structure impacts the mechanical behaviour, the pictures captured during the uniaxial compression were post processed with Digital Image Correlation [40]. Note that running a complete DIC analysis of the whole specimen proved impossible due to a bad light setup and grease interfering with the speckle pattern. However, by limiting the analysed part and the length of the analysis (stop the study before 3mm displacement of the specimen), some observations were made.

The transverse expansion was investigated by applying five horizontal vectors in the meshed part, as illustrated in Figure 5.17. The elongation gathered from the vectors were averaged, and the resulting elongation was compared to the vertical displacement of the specimen, as illustrated in Figure 5.18. The curves show that there is a significant difference between the different samples. By comparing the curves to the results found in Figure 5.11 it can be observed that the specimens with the lowest relative density (EH3) also has the lowest horizontal elongation, while the solid specimen K1 has the highest elongation. In other words, a low RD means that the horizontal elongation of the specimen during compression is minimal due to the change in volume (crushing of pores).

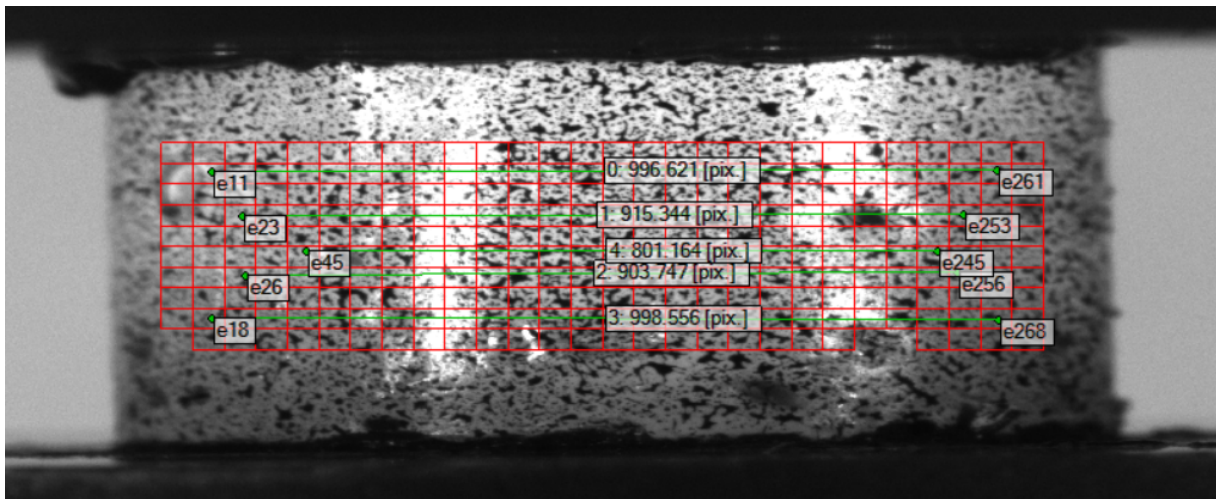


Figure 5.17: Horizontal elongation vectors on EH1.

Although the specimens with a high relative density have a large transverse expansion, it is the parts of those specimens with the lowest RD that gets the biggest expansion of the sample. That is observed in the specimen at the top (EH1) and bottom (EH5), where there is a sharp decrease in relative density from the one side to the other, as seen in Figure 5.11. Figure 5.19 shows a deformed state of these two specimens. By only considering the vertical edges it is clear that EH1 expand more at the bottom, while EH5 expand more at the top, which is where they have the lowest relative density. The reason for this behaviour was unclear but assumed to be because of strain localisation among the pores.

The transverse expansion (or contraction) is described by Poisson's ratio. It was previously assumed a value between 0.30 and 0.35 for the solid polypropylene (Tab. 5.1). Equation 5.6 [27] was employed to find an approximation of the ratio. Here, D and L is the specimen diameter and the length (height), respectively. ΔD , ΔL are the change in diameter and length. Note that this equation is meant for small deformations. The diameter and displacement data of K1 was used in the equation, and the result was

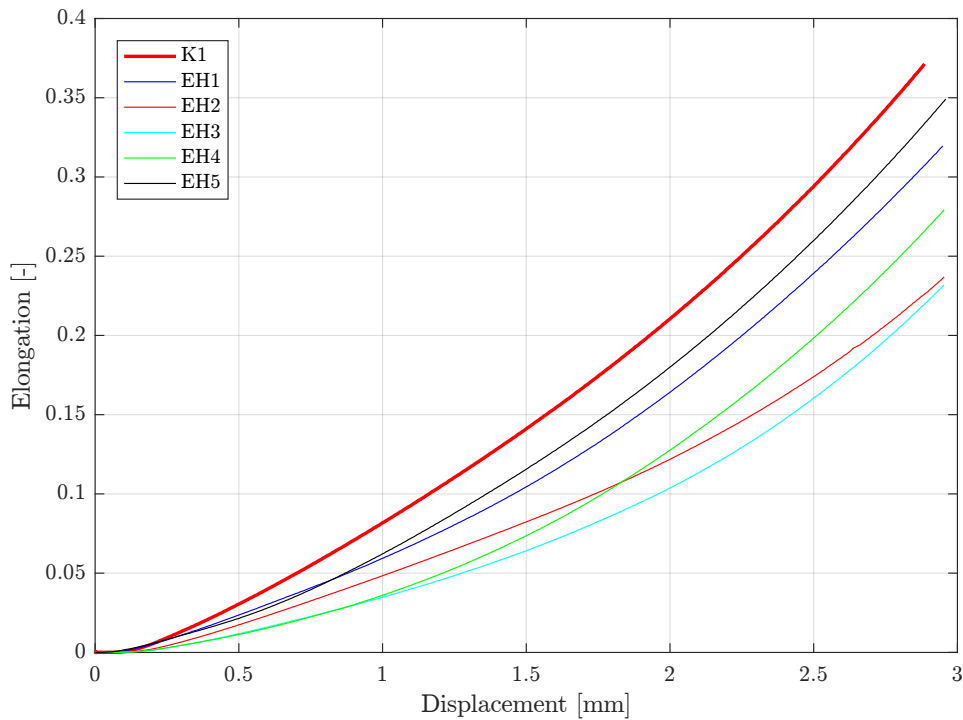


Figure 5.18: Horizontal elongation-displacement curve for the porous specimens and the solid specimen K1. Note that the displacement is the vertical translation of the indenter.

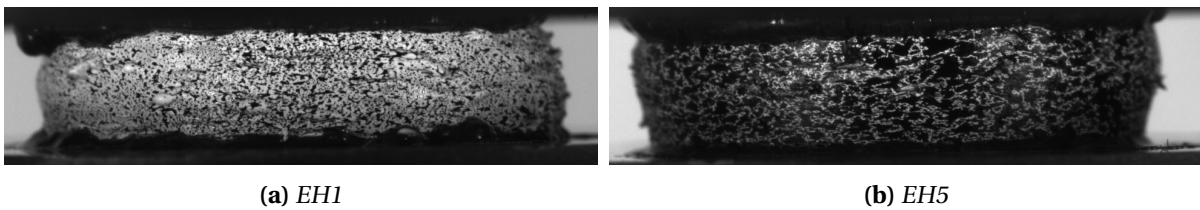


Figure 5.19: Deformation of specimens at approximate 2.5mm displacement. Notice the curvature of the edges.

a Poisson's ratio varying in between 0.20 to 0.38. The data were from compression tests, so friction is an error in the calculations that is hard to dissolve. Poisson's ratio was assumed to be 0.3 (as is most common for solid materials), and used herein.

The ratio was not determined for each specimen, because of the difficulty of finding the true diameter due to "spikes" (see right side of the specimen in Fig. 5.19a), and the unknown effect of friction. However, do note that the value is not zero (as a foam) since the transverse expansion is present and quite large. Nevertheless, Poisson's ratio will be smaller for the porous samples than the solid PP.

$$\nu = -\frac{\epsilon_{lateral}}{\epsilon_{axial}} \approx -\frac{\frac{\Delta D}{D}}{\frac{\Delta L}{L}} \quad (5.6)$$

5.4.3 Compression

The results of the compression tests are plotted in Figure 5.20 with the relative density next to it. The first thing to notice is that the solid PP is stronger than the porous material. Also, the pore structure seems to affect the shape of the curves; the yield point, plateau, densification (the process where pores are being crushed, the volume changes and the RD rises), and grouping are different for each specimen. These features will be discussed in the following. See Section 2.4 for more information about the features for cellular solids.

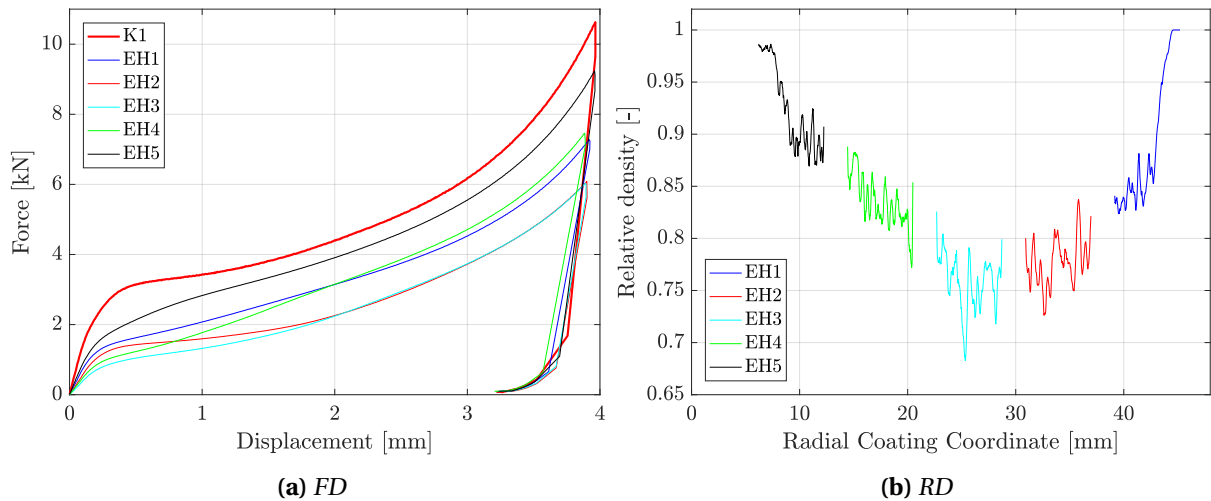


Figure 5.20: Experimental results of EH compression tests compared to K1 (a) and the RD curves of the EH series (b).

The yielding in the force-displacement curves is indicated by the sudden curvature after the elastic (linear) part in the start. That point is different for all specimens. These differences may be seen in relation to the observations made in the CT scan. The RD curves are believed to be important for the behaviour. However, they do not exclusively explain the order at which the samples yield; EH4 has a higher relative density than EH2, yet EH4 yields first. As found in the analysis of the block (Fig. 5.7), the pores are very different depending on the radial coordinate. In EH4 the pores are flat but long, and there are many of them, while in EH2 they are bigger and more round. Apparently, will this pore structure result in a low yield point. EH3 yields first, because of the low RD and the fact that the flat and long pores are present here as well. EH5, on the other hand, yields with the highest force, although the same pore structure is present. However, remember that the RD is the highest, and the pores are quite small. The effects of the pore structure on the yielding will be further investigated in the numerical studies.

The part of the FD curves after yielding is the plateau. Here, an increase in displacement results in a growth of plastic strain and work hardening (or softening). However, the force does not increase as much as before yielding or in the densification, resulting in a flattening of the curves (thereby the term "plateau"). Each specimen has their individual slope of the plateau. In the FD curve of EH2, the flat part is the most apparent. Then come EH3 and EH1 with a slightly increased slope. For EH4 the slope is quite high; it yields with a low force but quickly joins EH1. EH5 has an even higher slope, but unlike the other specimens, the curve softens (rate of force is reduced at about 1mm). There seems to be a correlation between the plateau and the RD; If the relative density is high, then the slope is high. The softening of EH5 may be caused by the many small pores that undergo a separate densification

process before the larger pores in the specimen are compressed, and the specimen fully densifies.

The next important property to discuss is the densification of the porous polypropylene. This process starts at the plateau but is strongly affecting the force-displacement curves as the displacement increases. Note that external and internal friction was assumed to be a part of this process, but it was not known how much it affects the results. The pores are compressed together to a point where the volume of the specimen is at its lowest so that what remains is solid polypropylene. After about 2mm displacement, the FD curves mimic the shape of the solid PP curve of K1.

As stated in Chapter 4, the force of each specimen seemed to distribute into three groups (K1 not included) at the end of the compression tests: EH5 at the top, EH1 and EH4 in the middle, and EH2 and EH3 with the lowest force. The grouping was assumed to happen because of the samples' relative density and the densification. A low relative density leads to a higher volume reduction during compression, and therefore the horizontal expansion is lowered (Sec. 5.4.2). That results in a lower cross-section area of the specimen which implies a lower force ($F = \sigma A$). EH5 had the highest RD, and therefore the highest grouping. EH1 and EH4 had similar RD, as well as EH2 and EH3, so they were grouped together. Note that the RD does not explain the grouping alone, other factors such as friction (both external and internal friction between the pore walls) may affect the resulting groups. The affects of internal pore friction will be investigated in the numerical studies.

5.5 Summary and discussion

The computed tomography images of the coating were employed to characterise the porous polypropylene layer. The analyses were conducted in 2D, and relevant statistics were extracted. A selection of pores was plotted in 3D to get a better understanding of the shape and orientation of them. The results suggested that the morphology is highly inhomogeneous and anisotropic. The pore structure seemed to depend on the radial direction only; in the other orientations (axial and hoop) the pore structure showed no significant change.

The analysis of the polymer block indicated that the coating had a varying relative density (0.7-1.0) where the lowest was found in the middle of the porous polypropylene layer (EH3). The RD was not symmetric about this point. The specimens showed the same trend as the block, and the values were employed to calculate their mass. The calculated mass was within the error space of the measured values, validating the method with which the RD was extracted.

The coating revealed a transition zone in the middle where the RD was at its lowest. At either side of this point, the pore structures seem to be different. That was observed in the curves of relative density, the number of pores, pore size and orientation, and the images in Figure 5.6. The extrusion process during the manufacturing of the coating was assumed to be the cause.

The mechanical response of the coating was investigated by finding a correlation between the characterisation of the coating and the uniaxial compression tests. First, a material model (stress-strain relationship) was calibrated for the solid polypropylene. The model assumed an isotropic elastic-plastic material insensitive to temperature, pressure and strain rate. By assuming the manufacturer's data on the tension tests could be combined with the compression data, the linear Drucker-Prager criterion was calibrated so that pressure sensitivity was included. Next, the transverse expansion was investigated. The porous specimens expanded less than the solid ones (EH3 showed about a 50% decrease in the transverse expansion). Note that the expansion seemed to be dependent on the relative density; a low value resulted in lower transverse enlargement. Furthermore, the investigation indicated that the pore structure affected the mechanical response. Each specimen had different pore morphology and force-displacement curves.

There were several sources of error in the results of the analyses. The simplifications and assumptions made may have an effect on the quality of the results. The CT scanning and the reconstruction process could produce errors; there were artefacts present in the image slices which were interpreted as matrix material (PP). The binarization of the slices may also produce errors due to the noise and blurriness of the CT slices. The cropped images at which the analysis was run were quite small and did not take into account the true radial coordinate (curvature of the block). The results of the uniaxial compression tests may include some error as well. The force measured by the load cell was assumed to be sufficient, but the displacement values were affected by the grease and other factors. The linear backwards extrapolation of the FD curves was assumed to be correct. The polypropylene material models were calibrated by making many assumptions, but the simulation results of the solid specimens were great. The DP criterion calibrated based on the tension data from the manufacturer should be used with care, because of the assumptions and simplifications made.

According to [26] and [27], foams have a relative density below 0.3 and Poisson's ratio (transverse expansion/contraction) in the vicinity of zero. The porous coating solution, Thermotite [13], did not meet those criteria, and will therefore not be characterised as a foam, but rather a solid material with

isolated pores.

The results found in this chapter has been in compliance with prior work [15, 16, 45, 12], and further characterised. However, there is still much to be investigated. The material and mechanical properties described herein will be further investigated by numerical studies.

Numerical studies

The main objective of the research project is to determine how coated steel pipes behave under impact loading, and validate to which extent this can be predicted using computational tools. Anticipating the probability of fracture after an impact event with accurate numerical models was assumed to be of great value to the industry. Considering the highly inhomogeneous and anisotropic pore morphology of the coating (Chap. 5), a constitutive relation representing the entire behaviour of the polymeric insulator was assumed to be difficult to calibrate.

Instead, a direct modelling technique was employed to create numerical models containing the actual pores. The method was inspired by a research article by Hegdal et al. [16], where they analysed the thermal conductivity of a porous polymer with reconstructed models. The intention was to re-create the coating from X-ray computed tomography images and simulate the mechanical behaviour, by utilising the material model of the matrix material. Given that the models are able to produce accurate results, they can become a valuable aid to determine the mechanical properties of the coating and to optimise the pore structure further.

In this chapter, the numerical simulations of the re-created specimens are presented. A sensitivity study was conducted, and the models were validated by comparing them to the experimental results. Furthermore, the direct models were employed to characterise the porous polypropylene and demonstrate its capabilities and limitations.

6.1 Numerical model

To re-create the specimens accurately, the X-ray computed tomography image slices were employed. The basic idea was that each pixel that is polypropylene should be meshed. The binary images (Sec. 5.3) already indicates which pixels. See Figure 6.2a for an illustration of the meshing process. Here the off-pixels (0) represented the solid material. Note that the elements are 3D cuboid elements. That means that the pixels were interpreted as voxels (Fig. 6.2b) so the cross section of the pixel was extruded up to the next layer. Since the slices' resolution were large, it had to be reduced so that the number of elements was not too big. A certain amount of images were employed (i) and scaled down

to a lower resolution (p), as illustrated in Figure 6.1.

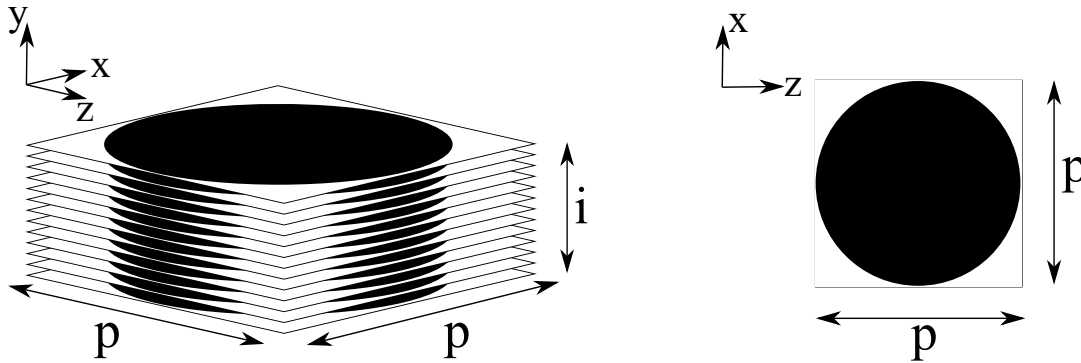


Figure 6.1: Illustration of the numerical replication. p is the number of pixels and i is the number of images used.

A voxel (see Fig. 6.2b for dimensions) was established and meshed as an eight node cube with reduced integration and hourglass control, C3D8R. Multiple instances of this voxel were then imported and translated into the correct place in the assembly where the image showed polymer (off-pixels). For each image slice, the imported and meshed voxels were joined by merging the connecting nodes. The process was repeated for all of the selected slices, which were eventually merged into a final re-creation of the specimen. In Figure 6.4a a finished specimen re-creation is depicted.

In Figure 6.3 a layer from Abaqus is put on top on the corresponding CT-image. As the figure illustrates, the reduced resolution of the image slices is significant for the accuracy of the replication. A too coarse mesh will lead to a poor replication, but a too fine will give rise to an extreme amount of elements in the mesh. The original image slices (unscaled) had a resolution of about 1600x1600 giving over two million off-pixels per slice. That amount of elements per slice is too many (simulation run-time would be too great). A reduction was necessary. Finding a suitable element size will be investigated in Section 6.2.1.

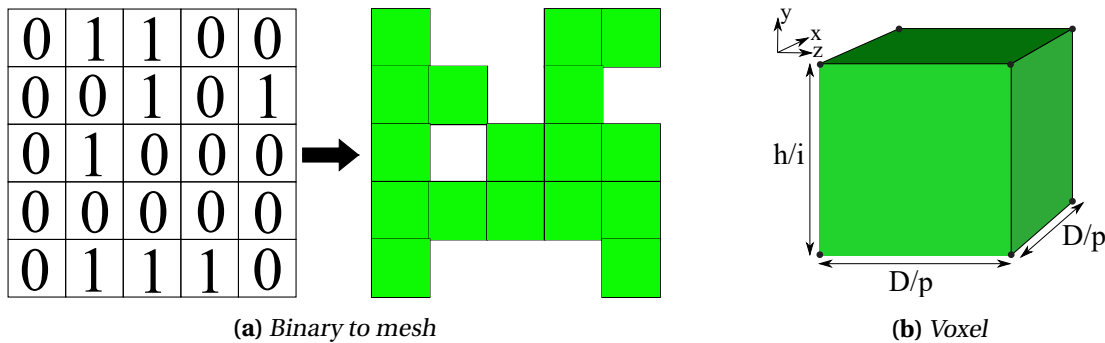


Figure 6.2: The mesh was built from textfiles containing ones and zeros. Here, the zeros represent the matrix material and the ones represent the pores. In (b) the element is shown. The element is an 8-node cube element of the lower order. Note the length of the sides. Remember that D are the specimen diameter and h is its height. p and i is defined as in Fig. 6.1.

The technique to establish the direct model of the specimen involves many thousand interactions (create an instance of every voxel, translate it and merge with others) in the Abaqus GUI. However, as the process is highly repeatable, the python scripting option where utilised, with guidance from the scripting manual provided by Abaqus [46]. Without scripting, this method to replicate the specimens

could probably not be conducted as it would take too much time. Nevertheless, it shall be mentioned that the script used a considerable amount of time to finish the re-creation. As an example, to create the specimen EH4 based on 60 images with a resolution 80x80 pixels (80p60i) the script ran for about 45 minutes.

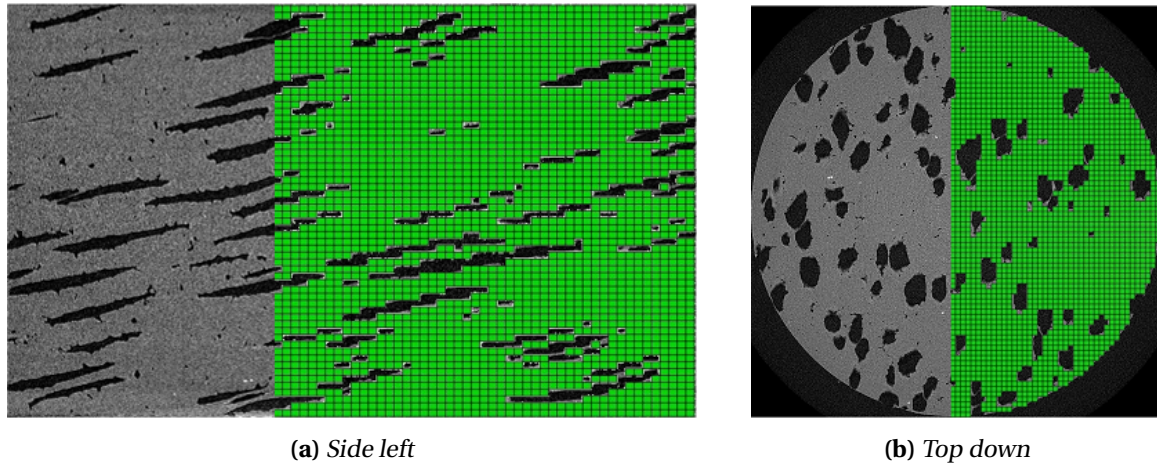


Figure 6.3: Recreation of specimen EH4, on top of the corresponding CT-image, where the green part is the mesh. Here, 60 images (i) where each image has a resolution of 80 pixels (p) is used. Note that about half of the mesh is left out for illustrative purposes.

To replicate the experimental setup discussed in Section 4.3.1 two analytical rigid plates were inserted into the assembly to represent the support and the indenter. The support was fixed, while the indenter was given a velocity down towards the specimen, which was ramped up from zero to maximum velocity in the first ten percentages of the simulation time. That would reduce the dynamic effects, which was desired due to the quasi-static conditions of the physical tests. The velocity of the indenter was set according to the simulation time so that the specimen would be compressed about 4mm. The simulation was done in Abaqus/Explicit, with a step time of 0.005s, giving a velocity of 840mm/s. Note that this deformation rate is greater than the one used during the physical tests (0.36mm/s), but since the material model do not account for strain rate effects, the speed would not affect the response of the simulation. Figure 6.4b shows the assembly setup.

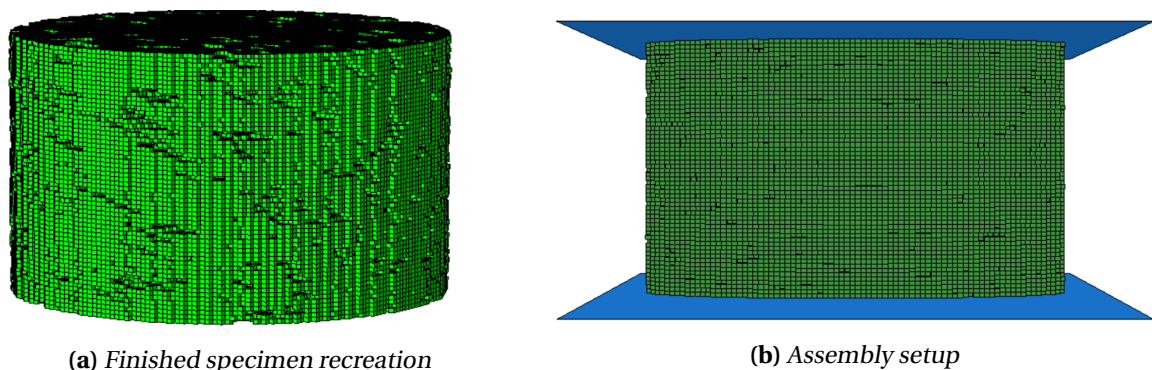
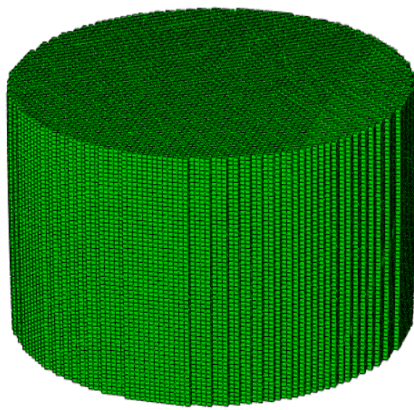


Figure 6.4: 80p60i re-creation of specimen EH4. In (b) the blue plates are the rigid surfaces, where the top one is the indenter, and the bottom one is the fixed support.

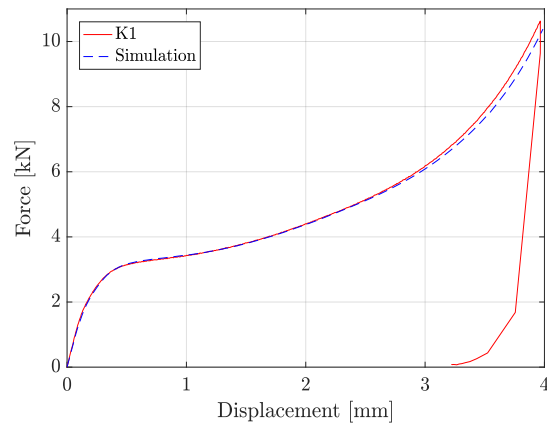
For the interaction, both external contact between the rigid plates and the specimen, and self-contact within the sample (pores) needed to be considered. Initially, it was assumed that the internal friction

was of little importance and that it would be sufficient to describe it together with the external friction. As a result, the interaction was described by the general contact formulation with default values for normal behaviour and tangential behaviour with a friction coefficient of 0.025, as was found in Section 5.4.1. A later study in Sec. 6.2.4, shows that the internal friction affects the result a lot and should be treated separately from the external friction.

The material parameters applied to the re-creations is the same as calibrated in Section 5.4.1, which showed accurate results when re-creating the compression test on K1 with an axisymmetric model. To confirm that the direct modelling technique performs sufficiently, the material model was applied to the replication of K1 (80p60i). Figure 6.5a shows the final re-creation of K1 and in Figure 6.5b the resulting force-displacement curve from the simulation and experiment are plotted and compared. The curves match at the beginning, but the simulation gives a marginal weaker response in the end. Despite the difference towards the end, the result gives confidence to the numerical model.



(a) Recreation of K1



(b) Force-displacement plot

Figure 6.5: 80p60i replication of K1 and the results of the simulation compared to the experiment.

The numerical model was entirely created by a Python script; re-creation of the specimen, assembly setup, interaction, material properties, etc. was set by code. In Appendix C, the script to create EH4 80p60i is shown.

6.2 Sensitivity study

In this section, the sensitivity study conducted on the re-creation of EH4 subjected to uniaxial compression is presented. Optimally the study should be carried out on all the specimens. However, since the simulations were time-consuming, it was decided to conduct the study on one specimen only. EH4 was chosen due to its peculiar behaviour during compression (Sec. 5.4.3) and therefore assumed to be more sensitive to changes than the rest.

6.2.1 Mesh size

As mentioned, the size of the original CT image slices needs to be scaled down (reduce resolution) to make an executable Abaqus model. To determine how much the images can be scaled, while still give an acceptable replication, a sensitivity study was necessary. To investigate the sensitivity of the mesh size (the size and number of elements), a visual verification, and a consideration of the resulting force-displacement and relative density curves of the numerical model were conducted. The element size is determined by the number of pixels in the scaled image, and how many images used (Fig. 6.2b). An increase in the resolution of an image will lead to more pixels, which reduces the width of the elements. An increase in the number of images leads to a lower element height.

Visual inspection

Both vertical and horizontal directions were inspected as the quality of the scaled image and how many images needed has to be considered. The investigation showed that the resolution of a slice had to be at least 50x50 pixels (50p), to resemble the true pore structure adequately. The same minimum amount was found for the number of images in height. In Figure 6.6 the visual improvement achieved by increasing the resolution of the picture is illustrated. The figure shows that there is a substantial refinement from 50p to 80p, and the pores in the 100p replication seem to be fairly accurate. However, while increasing the resolution, the number of elements in the model will grow equally, and thereby actively increase the computational time.

Figure 6.7 and 6.8 illustrates the effect of changing the amount of images used in the re-creation. It was observed some improvement in quality by increasing the number of image slices. However, it is not as significant as changing the resolution. Do note that the resolution will also affect the quality when considering the vertical sides; the number of elements in the horizontal direction depends on the resolution. At the same time, it is important to use enough pictures, such that pores do not get lost between the slices. Increasing the number of images will not introduce as many elements as enhancing the resolution of the pictures. However, increasing the number of images could be pretty vital for the simulation time if the element height gets smaller than the width. In explicit simulations, the smallest element length is crucial for the incremental time step [47]. The height and width should preferably not differ too much.

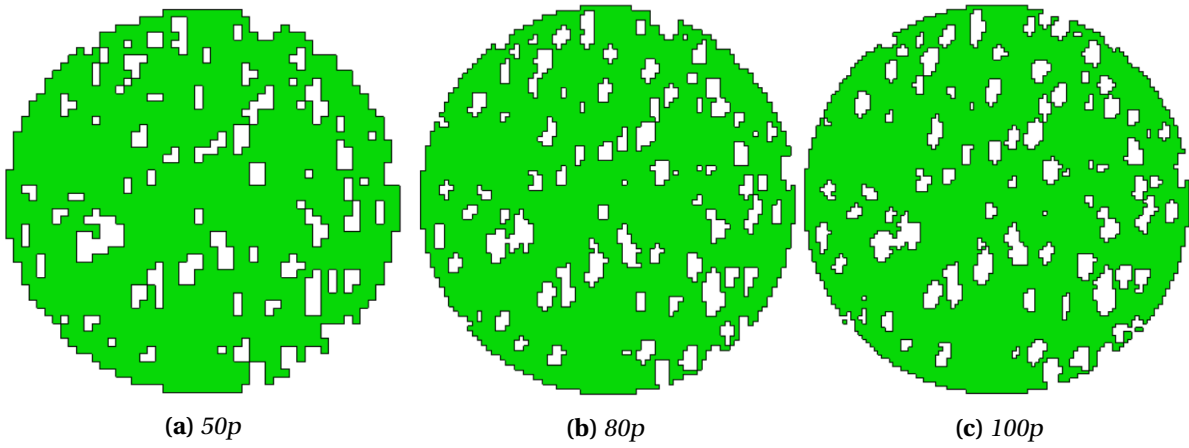


Figure 6.6: Horizontal (top-down) cut in the middle of specimen EH4 re-created based on a different amount of pixels (p).

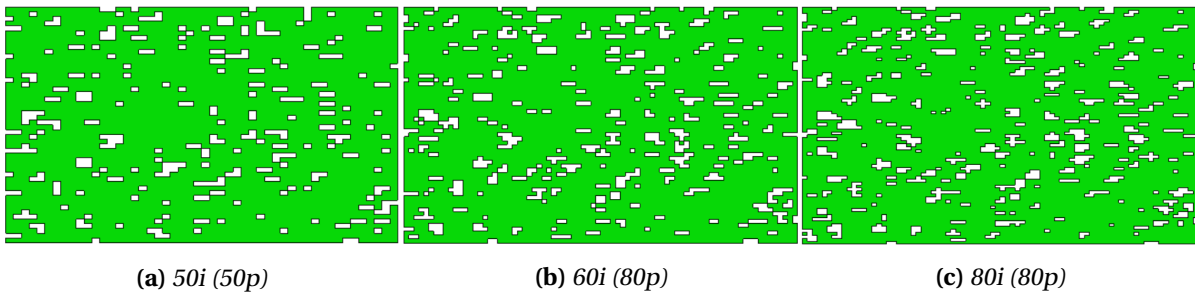


Figure 6.7: Vertical (side top) cut in the middle of specimen EH4 re-created based on a different amount of images (i).

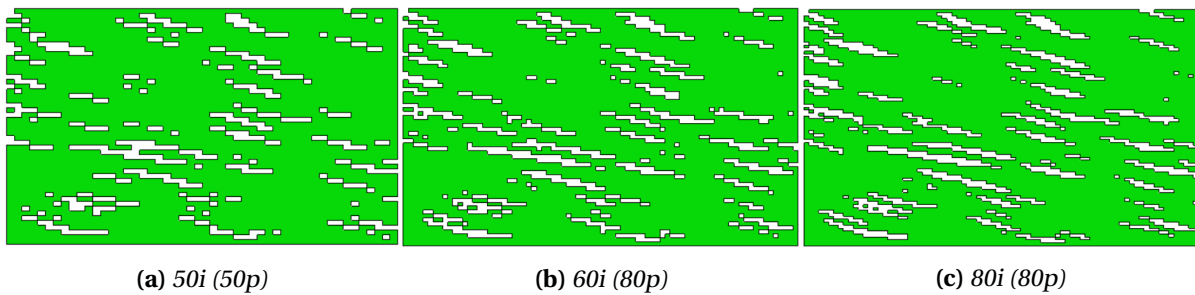


Figure 6.8: Vertical (side left) cut in the middle of specimen EH4 re-created based on a different amount of images (i).

Relative density

A problem connected with reducing the resolution of the images is that some pores might be neglected and others altered in size. To get a better understanding of the different replications' ability to re-create the original specimen the relative density was considered. In Figure 6.9b, the relative density of various replicas are compared to the original curve of EH4. From the figure, it can be seen that the relative density is a bit higher for all the numerical recreations. However, all curves follow the same general trend. It can also be seen that a coarser re-creation shifts the curves upwards. These results indicate that the model gets more matrix material at the expense of pore volume, which may lead to some increased strength in the simulations.

In Figure 6.9a, the relative density curves for all specimens are compared to the replicas. An interesting observation was made on the far left of the curves, where specimen EH5 is located. Here there is a significant gap between the replicas and the physical specimen. In Chapter 5, it was observed that the lower part of specimen EH5 consists of mostly small pores, which the numerical models is apparently not able to capture, hence the space between the curves. The re-creations show an RD over one! For the rest of the curve, the curvature is captured well for every specimen, but with a slight increase. Note that the curves have RD values above 1.0 at the edges, which is presumed to be caused by the rectangle shape of the elements not being able to produce a perfect circle.

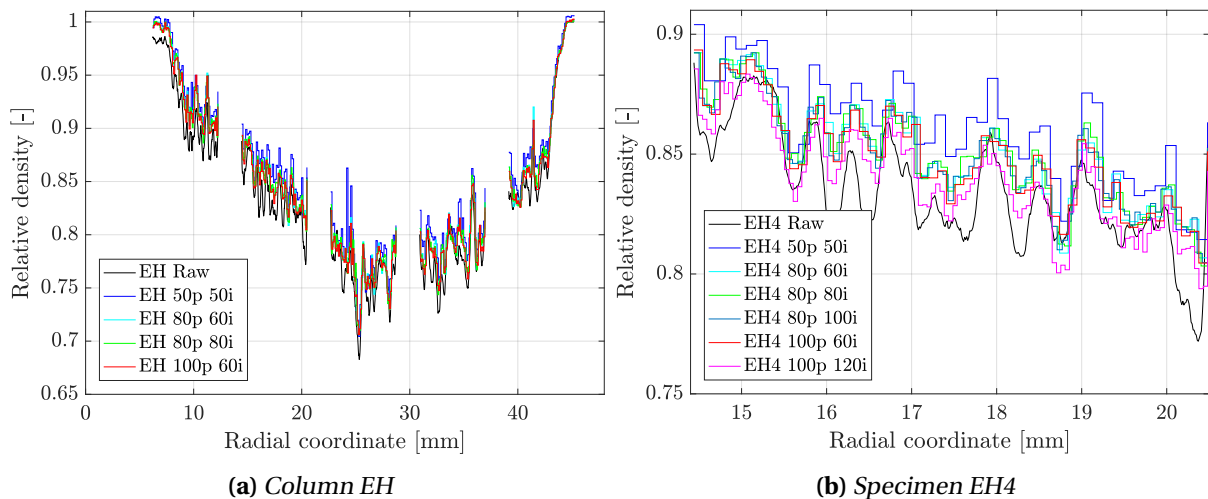


Figure 6.9: Relative density curves for the specimens and its replications.

Force-displacement

The resulting force-displacement curves from the numerical re-creation will give good indications to the accuracy of the model, and provide valuable insight when determining an acceptable mesh size. In Figure 6.10, the FD curves for six different re-creations are illustrated. The curves indicate that the yield strength increase with a coarser re-creation; the 50p50i replication had the highest force. In the middle four models (80p60i, 80p80i, 100p60i and 80p100i) lays close together. At the bottom, the 100p120i model is found and coincides well to the experimental values. Despite the difference in yield strength, all of the curves converge as the models get fully compressed. This behaviour indicates that the mesh size is of most importance around the yield point, while the pore structure is intact, and

gets less important when the pores get crushed flat. Note that internal friction coefficient was set to 0.025 in these simulations.

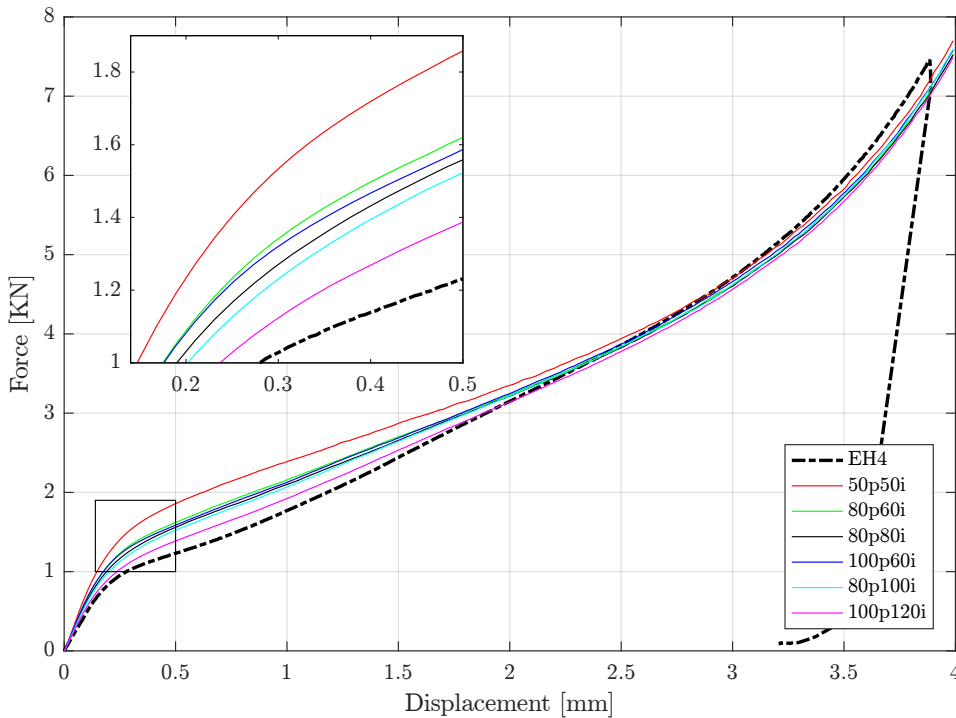


Figure 6.10: Force-displacement curves for different mesh sizes compared to the experimental values.

An explanation for the increased yield strength can be the use of cuboids in the re-creation. Figure 6.8 shows that the pores in EH4 get a stairway looking shape in the replications. It was assumed that the straight edges could lead to increased strength where the model ends up closing the pore as it jumps one level down (Fig. 6.11). Here, the nodes from the top of the pore will connect with the nodes at the bottom, thus an increase in strength.

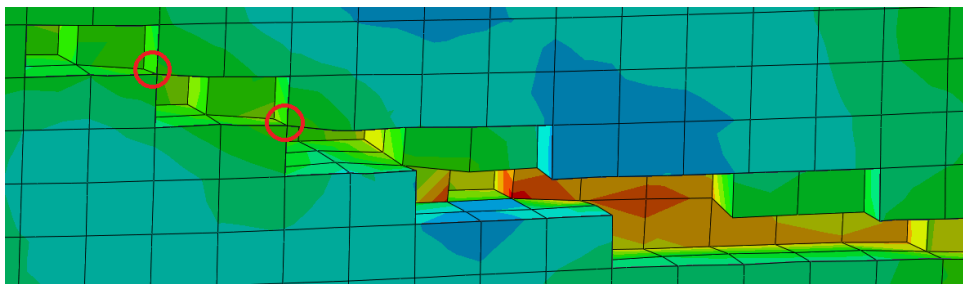


Figure 6.11: Pore gets closed as indicated by the red circles as it jumps one level.

As the results suggest, a finer re-creation fits better with the experimental results. However, Table 6.1 demonstrates that there is a significant increase in CPU-time when improving the mesh. For the coarsest re-creation, 50p50i, the simulation run for a little under 2 hours, while the finest, 100p120i, run for over 43 hours. An important aspect to note from the table is that the smallest length of an element is of greater importance than the number of elements, as seen by comparing re-creations 80p80i and 100p60i. 100p60i has almost 80000 more elements than 80p80i, however as 80p80i has a smaller element height it has a longer simulation run-time. It is therefore important to try to have

similar element width and height. Note that this does not conclude that the number of elements is unimportant for the CPU-time. 80p60i and 100p60i have the same element height, yet the increase of elements in 100p60i leads to three hours increase in simulation run-time.

Table 6.1: Parameters for different re-creations of specimen EH4. Note that all simulations were run on the same computer cluster, Snurre, with 8 cores.

Recreation type	# elements	Width of element	Height of element	CPU-time
[-]	[-]	[mm]	[mm]	[hh:mm:ss]
50p50i	84,589	0.200	0.120	01:46:25
80p60i	256,513	0.125	0.100	09:16:45
80p80i	324,024	0.125	0.075	13:46:02
80p100i	427,280	0.125	0.060	21:02:12
100p60i	402,964	0.100	0.100	13:20:37
100p120i	791,657	0.100	0.050	43:24:59

Based on the result found in this section the re-creation 80p60i was chosen for further investigation. This model produced similar results as the finer recreations (80p80i, 80p100i and 100p60i) in both relative density and force-displacement. However, it had a significant reduction in CPU-time. The 100p120i model showed a distinct improvement in the FD curve, but with a simulation run-time of 43 hours. Further investigation on this replication would be too time-consuming.

In Figure 6.12 the 80p60i re-creation of EH4 is illustrated. The model has been cut to illustrate the internal pore structure. The figure shows a similar pore structure as observed in Fig. 4.9, with long and flat pores. The recreation is not optimal, but as the model seems to reflect the pore morphology, it was assumed that it would produce satisfactory results.

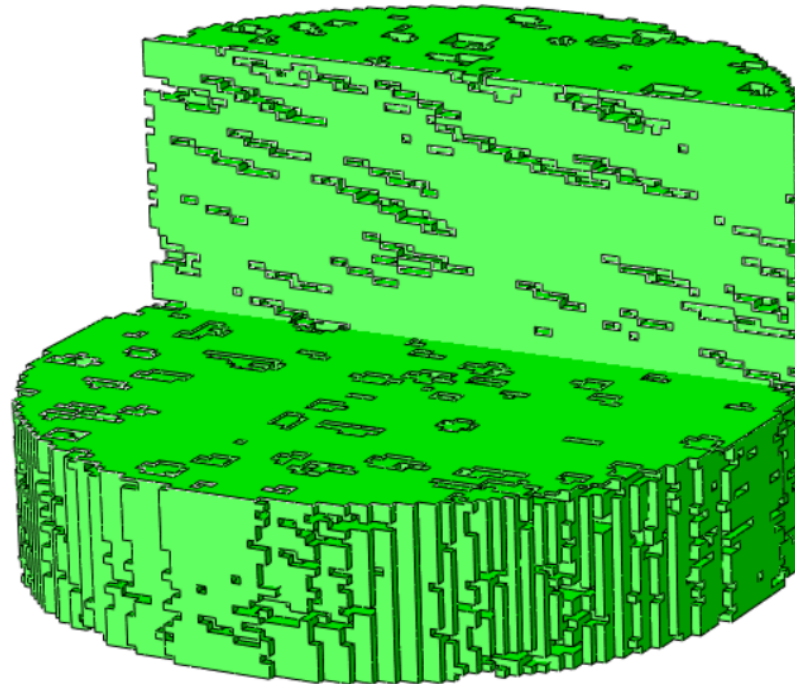


Figure 6.12: 80p60i re-creation of EH4 with a cut.

6.2.2 Element type

In Section 6.1, it was mentioned that the model was created with reduced integration eight node cube elements. This choice was made because of the reduced element's significant advantage in CPU-time, due to its simplified methods for strain calculation [21]. A problem connected with the use of reduced integration elements is hourglassing [48], and hourglass control is introduced to limit the problem. Two other element types were tested to verify that the reduced integration element produces an accurate result. The two other kinds were fully integrated cube element, C3D8, and cube element with incompatible modes, C3D8I.

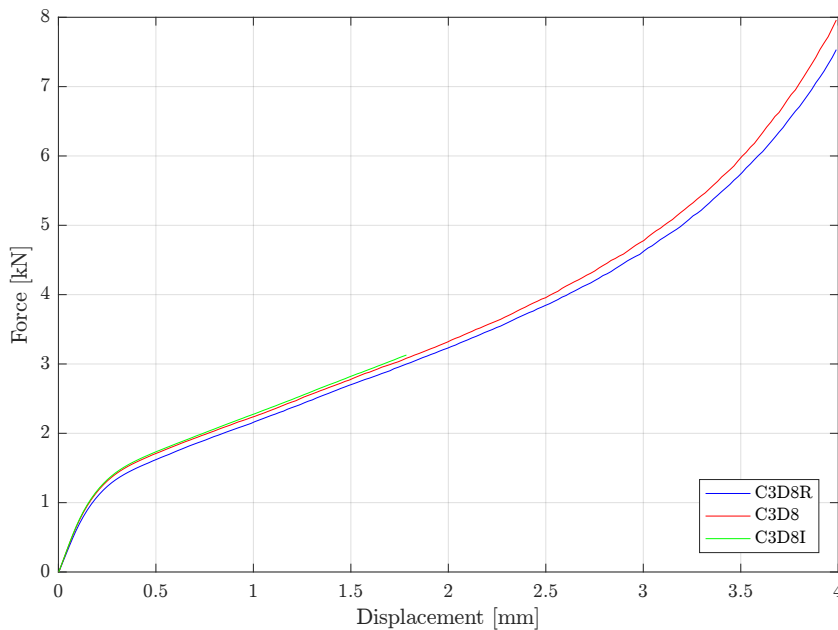


Figure 6.13: Force-displacement curves for different element types.

In Figure 6.13 the resulting force-displacement plot for the three different element type are illustrated. The simulation with C3D8I was not able to simulate the full deformation of the specimen and aborted due to excessively element distortion. The simulation with C3D8 was able to complete. A similar behaviour can be seen for all curves with a small increase in stiffness for C3D8 and C3D8I. In a non-linear analysis, fully integrated cube elements may lead to volumetric locking [21] and therefore excessive stiffness, which may explain the increase in stiffness observed in the plot. Another explanation could be that the C3D8R has numerical errors causing it to be slightly weaker. In addition to the possibility of volumetric locking, the C3D8 element model had a longer CPU-time (18 hours) than the reduced integrated elements (9 hours). The reason is connected to the number of integration points. The C3D8I element is similar to the C3D8 element, only with one extra node in height for each vertical edge, thus making it more suited for bending problems. As the elements investigated herein are mainly subjected to pure compression, this extension may not be very beneficial here. As the curves match reasonably well and the advantage in CPU-time, the C3D8R elements will be utilised in further simulations.

6.2.3 Material model

The material model employed in the simulations was calibrated in Section 5.4.1, by the use of the experimental results and inverse modelling. The material model showed satisfactory results within the tested region, but the plastic strain only reached a magnitude of approximate 1.0 for the solid specimen. The porous specimens may reach even higher strains because of the pores. Initially, the curve was extrapolated using a third-degree polynomial fitted to the end, to account for higher plastic strains. However, this is not necessarily the correct material behaviour.

Two additional material models were established to determine how the values in the material model at the extrapolated part affect the result. Both models have the same values until a plastic strain of 1.0 but split up afterwards. One of the material models had a perfectly plastic behaviour, while the other one had a sharp increase. Figure 6.14a shows the true stress-plastic strain curves for the two material models described together with the original one ("Calibrated"). There is a wide gap between the curves, which is done to be able to observe how the alterations to the material model affect the results. In Figure 6.14b, the force-displacement plots for the different material models are illustrated. The plot indicates that the alterations are of little importance to the result, and does only show a difference after the specimen has been displaced more than 3mm.

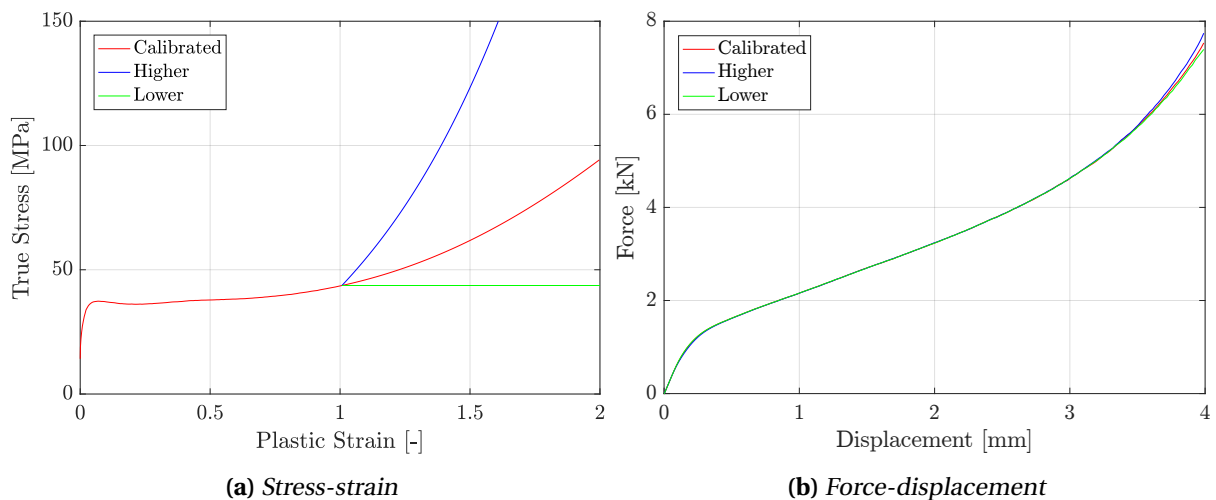


Figure 6.14: Different extrapolations of the material model and their impact on the resulting force-displacement curve of EH4.

An additional study was conducted on the material model to determine the sensitivity. Three new models were created, as seen in Fig. 6.15a. In the model "Higher" and "Lower", the plastic part of the calibrated material model was shifted up and down, respectively. The third model was created as perfectly-plastic to inspect the effect of softening and hardening. The yield point was set to 37.3MPa, the stress corresponding to the peak of the calibrated material model. Figure 6.15b shows the FD curves from the simulations with the different material models. Shifting the material model up or down leads to a shift in the FD curve, with an increasing effect as the specimen gets more displaced. By comparing the perfectly plastic model with the calibrated model, it seems that the lack of softening gives a stronger yield point, while the lack of hardening results in a weaker response at larger displacements. However, even though the perfectly plastic material model does not include work hardening/softening the results are quite satisfactory.

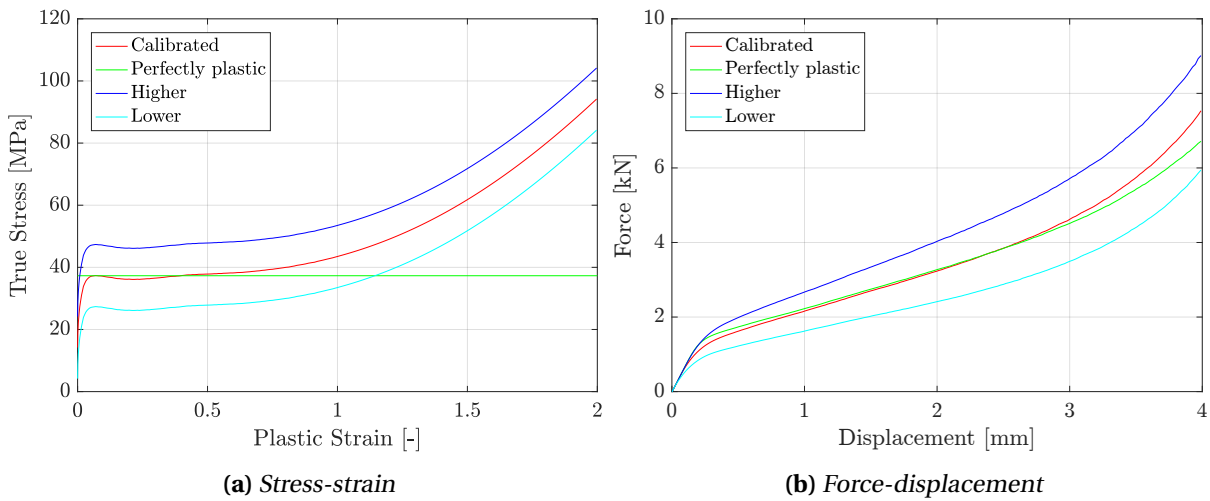


Figure 6.15: Different material models and their impact on the resulting force-displacement curve of EH4.

6.2.4 Friction

When conducting compression tests the introduction of friction is an unwanted effect, yet almost impossible to completely prevent. There is no easy way to determine the correct friction coefficient; it will have an unknown impact on the results. Grease was applied to the top and bottom of the specimens during the uniaxial compression tests, but friction forces were still present (barrelling). With the use of inverse modelling in the material model calibration, the external friction coefficient was found to be 0.025 (Sec. 5.4.1). For the interaction inside the specimen (pores), it was not possible to know the FC.

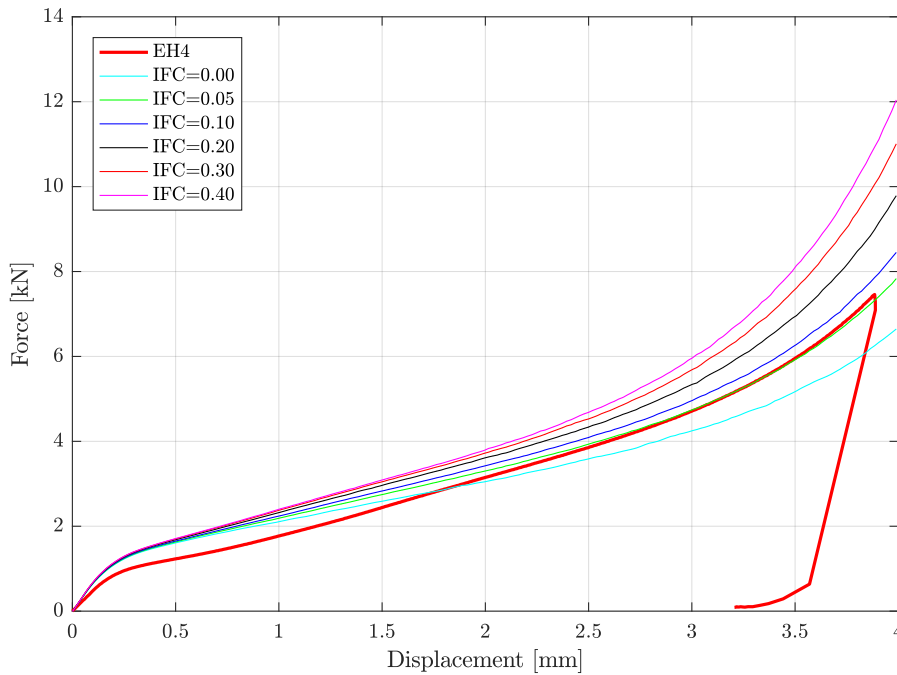


Figure 6.16: Force-displacement curves for specimen EH4 with different internal friction coefficients (IFC).

The original interaction formulation was described by general contact, with no concern for a separate internal friction coefficient (IFC). Different friction parameters were accounted for by modifying general contact formulation was to have individual property assignments for the external interaction, while the global property assignments set the internal friction parameters. Several friction coefficients were tested to determine the sensitivity. The IFCs tested were 0.0, 0.05, 0.1, 0.2, 0.3 and 0.4.

In Figure 6.16, the resulting force-displacement curves for the different friction coefficients are plotted. The curves illustrate that the changes made to the internal friction coefficient affect the curve significantly. The plot also shows that the curves are influenced more towards the end of the displacement. That is reasonable, as the pores need to be compressed for friction to occur. It can also be observed that changing the IFC gives larger response for the smaller values, i.e., the gap between 0.1 and 0.2 is greater than the difference between 0.2 and 0.3. By comparing the curves from the numerical simulations to the experiment (EH4), the simulation with an internal friction of 0.10 seems to be the best fit as they have similar curvature at the ending.

Another important aspect to consider when changing the friction is the visual effect it has on the deformed specimen. Figure 6.18 shows the final deformation of the numerical re-creations of specimen EH4 with different friction coefficients. There are no huge differences between the pictures, but by looking at the vertical edges at the periphery, some changes can be observed. The simulation with zero friction differs from the rest by having the largest expansion at the top of the specimen, while the rest has the most substantial increase around the middle. It can also be observed that an increase in friction gives a more curvy edge. By comparing the numerical re-creations to the final deformation observed in the experiment (Fig. 6.17), it can be seen that the right side edge is more straight like the numerical models with low internal friction (0.10f). The left side edge is partly covered in grease, thus limiting the visual part of the curvature, but it seems to be somewhat similar to the numerical re-creations with an IFC above zero.

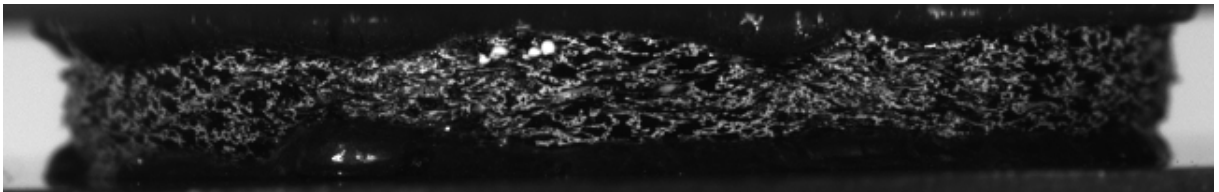


Figure 6.17: Final deformation of EH4.

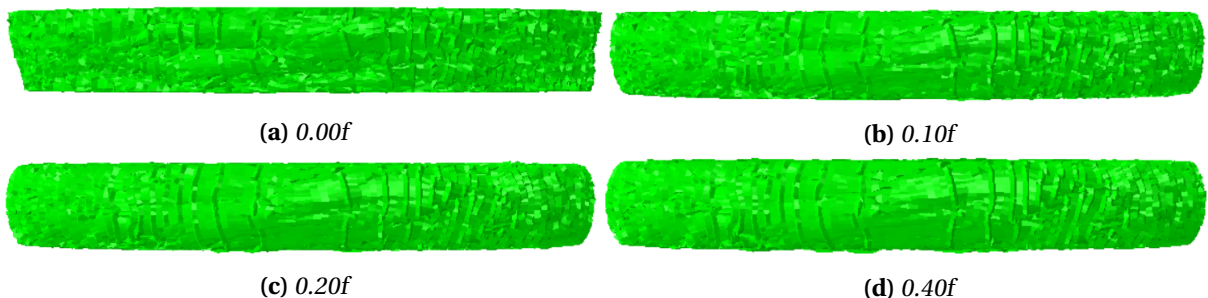


Figure 6.18: Final deformation of the numerical re-creation of EH4 with different friction coefficients.

6.2.5 Imperfections

In Figure 6.10, it was observed that the models had a too stiff behaviour at the beginning compared to the experiment. A possible remedy for this could be to introduce imperfections to the model. It was assumed that the perfect structure in the element composition caused increased strength in the model and that an introduction of imperfections could force the element structure to buckle (yield) earlier. To test this assumption distortion was introduced to the structure by displacing each node a random distance in the horizontal plane. The nodes were allowed to move up to a certain percentage of the element width in both directions in the horizontal plane. Three models were created with 8%, 20% and 40% imperfections, respectively. For the simulation with 20%, the nodes could also move in vertical directions, thus making a rough surface at the top and bottom. The rigid support and indenter were translated to account for the additional height.

Figure 6.19 illustrates how the introduction of imperfection affects the mesh structure. The visual deformation in the mesh is observable. However, the simulations showed minimal deviations on the resulting FD curves (Fig. 6.20). The simulation with 20% node displacement was the only simulation that yielded any noticeable difference. Remember that in this simulation the nodes was moved in a vertical direction as well as horizontal, which lead to a rough surface at the bottom and top. The shift in the curve for this simulation is assumed to be caused by this roughened surface. The study indicates that the numerical model is insensitive to imperfections.

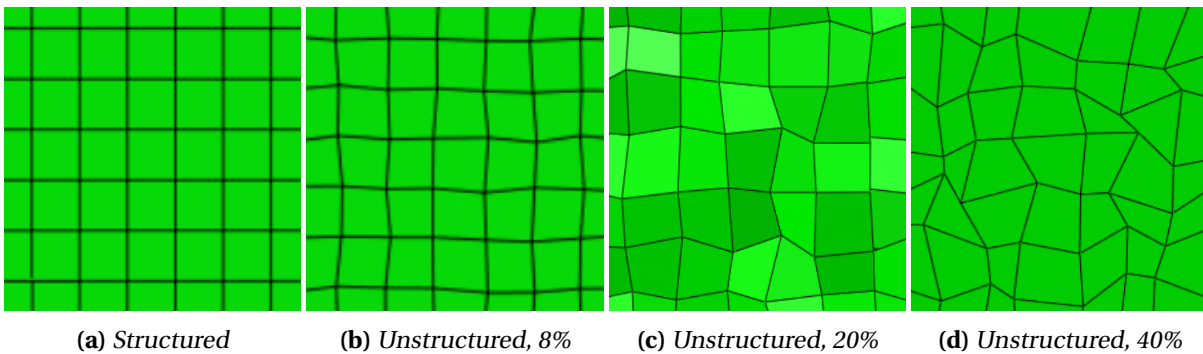


Figure 6.19: Illustration of the different element structures. The percentage tells how much of the element width each node could maximum be moved in the horizontal direction. Note that in (c) the nodes were displaced in the vertical direction as well.

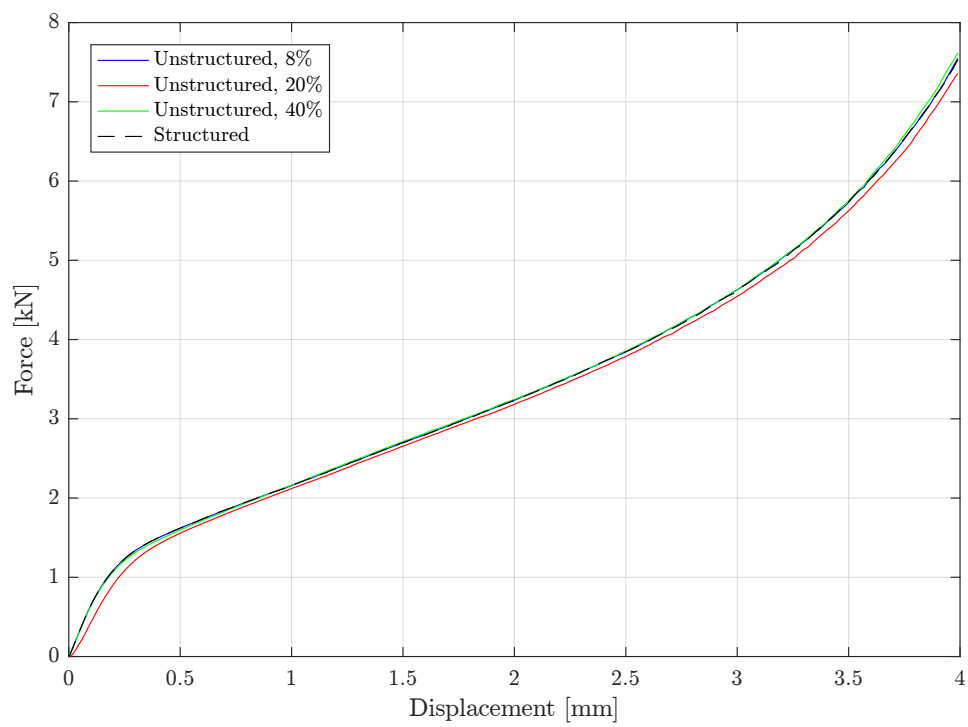


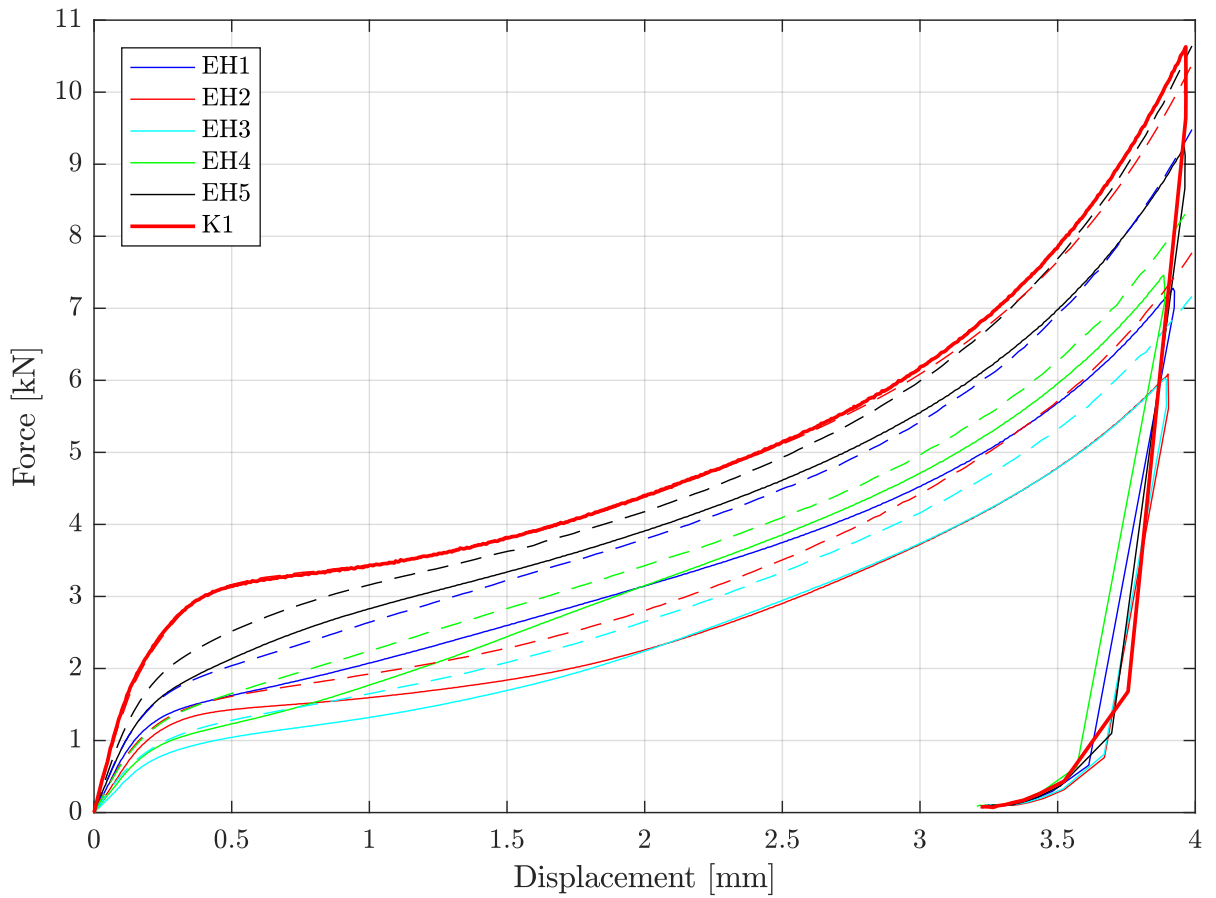
Figure 6.20: Force-displacement curves for different mesh structures.

6.3 Validation of the direct model

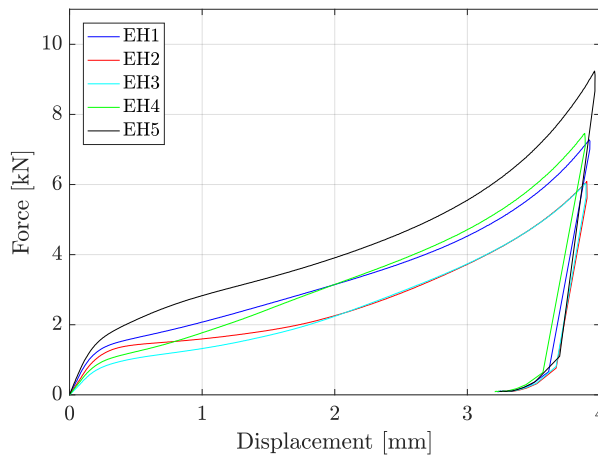
If the direct models are to be used in a further investigation of the coating, it is imperative that they can produce similar results as the experiments. Not only for specimen EH4 but every sample. The accuracy of the numerical models was tested by establishing all five specimens with the direct modelling technique described in Section 6.1, with an 80p60i mesh size. Based on the results found in the sensitivity study, the internal friction coefficient was set to 0.1, while the external friction coefficient was kept at 0.025. No imperfections were included.

Figure 6.21 shows the force-displacement curves for both the experiment and the simulations. By comparing the curves, it was observed that the simulations are not able to replicate the exact behaviour of the experiments. All the simulations overestimate the force with a stronger response. The yielding happens at a higher level of force in the simulations, resulting in elevated curves. At larger displacement, the simulations do not entirely copy the experiment; the same grouping with EH2 and EH3, and EH1 and EH4 are not achieved. The mesh size sensitivity of the numerical model (Sec. 6.2.1) was assumed to be the explanation of the increased strength.

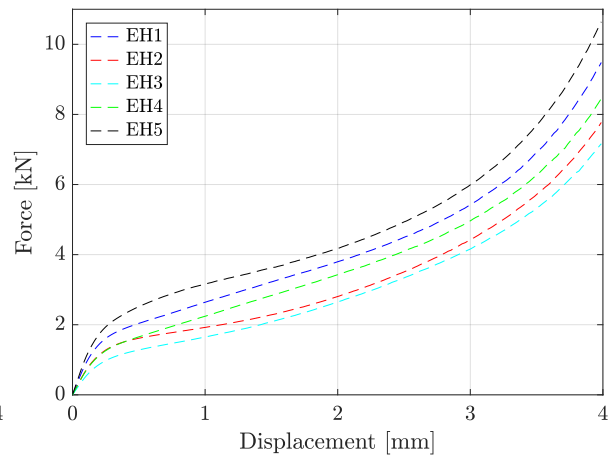
By looking past the increased strength of the numerical models, the general trends of the curves were captured by the simulations. Every one of the specimens has a distinct behaviour after yielding which is recognisable in the simulations. As the only difference between the numerical models is pore structure, the results indicate that the response is dependent on the pore morphology. The good correlation between the experiment and the simulations suggest that the models are able to replicate the pore structure and its behaviour during compression fairly accurate. The simulations should, therefore, be able to give some valuable insight into the structural behaviour of the specimens during compression. The numerical models were used to characterise mechanical properties of the porous polypropylene further.



(a) Comparison



(b) Experiments



(c) Numerical simulations

Figure 6.21: Force-displacement curves for the different specimens of the EH series, where the whole lines are from the experiments, and the stapled lines corresponds to the simulations.

6.4 Further characterisation and model capabilities

In Section 5.2, a characterisation of the pore morphology of the porous polypropylene was conducted. The mechanical properties proved difficult to understand completely. The results of the numerical direct modelled specimens could potentially show new information to help in that regard. The models will be further investigated for stress localisation, and a model of the entire porous polypropylene layer will be established to consider its behaviour.

The numerical models replicated the mechanical response of the porous specimen subjected to uniaxial compression, satisfactorily. The direct modelling technique may be able to capture other characteristics as well. The method will be used to investigate its ability to describe mechanical anisotropy, tension and fracture properties of the coating. The simulation results are also used to suggest characteristics of the porous polypropylene layer. However, the results should be observed with a critical view. Note that the results are not validated by any experiments.

6.4.1 Stress localisation

In Figure 6.22, the stress distribution at yielding (displacement in the vicinity of 0.2mm) are illustrated for the porous specimens. The figure shows the middle slice of all the replications, in two perpendicular directions. Looking at K1 (Fig. 6.23), a symmetric stress distribution is observed, while for the porous models the stress localises in bands connecting the pores, hence creating a unsymmetrical stress distribution.

It was assumed that the stress localised where the area is lowest. Hence, the pores should affect the localisation of the yield surface in the specimen. With that logic, the specimen with the lowest relative density (highest area reduction) (Fig. 5.20) should yield first. That is true for the specimen EH3. However, it does not explain why EH4 yields before EH2. Note that the RD curve was established by calculating the area reduction in the horizontal image slices. The lowest possible area is the surface connecting to the pores not only in the axial-hoop plane (3D surface). To explain the early yielding of EH4, it was assumed that the yield area (surface) was small, due to the pore morphology in the specimen.

In Section 5.2, it was showed that EH4 consists of many long and thin pores, with a relative slant orientation. Specimen EH2 has a fewer amount of pores which are large and round with a more vertical orientation. The difference in the morphology seems to give a lower yield area for EH4, thus explaining the earlier yielding.

Another characteristic of the EH4 specimen subjected to compression, was the steep FD curve (high slope of plateau). That may be explained by the fact that the pores are crushed faster, because of the long and flat shape, i.e. the specimen densifies quicker than the others. This was observed in the numerical models, where the pores in EH4 seemed to be faster compressed than EH2

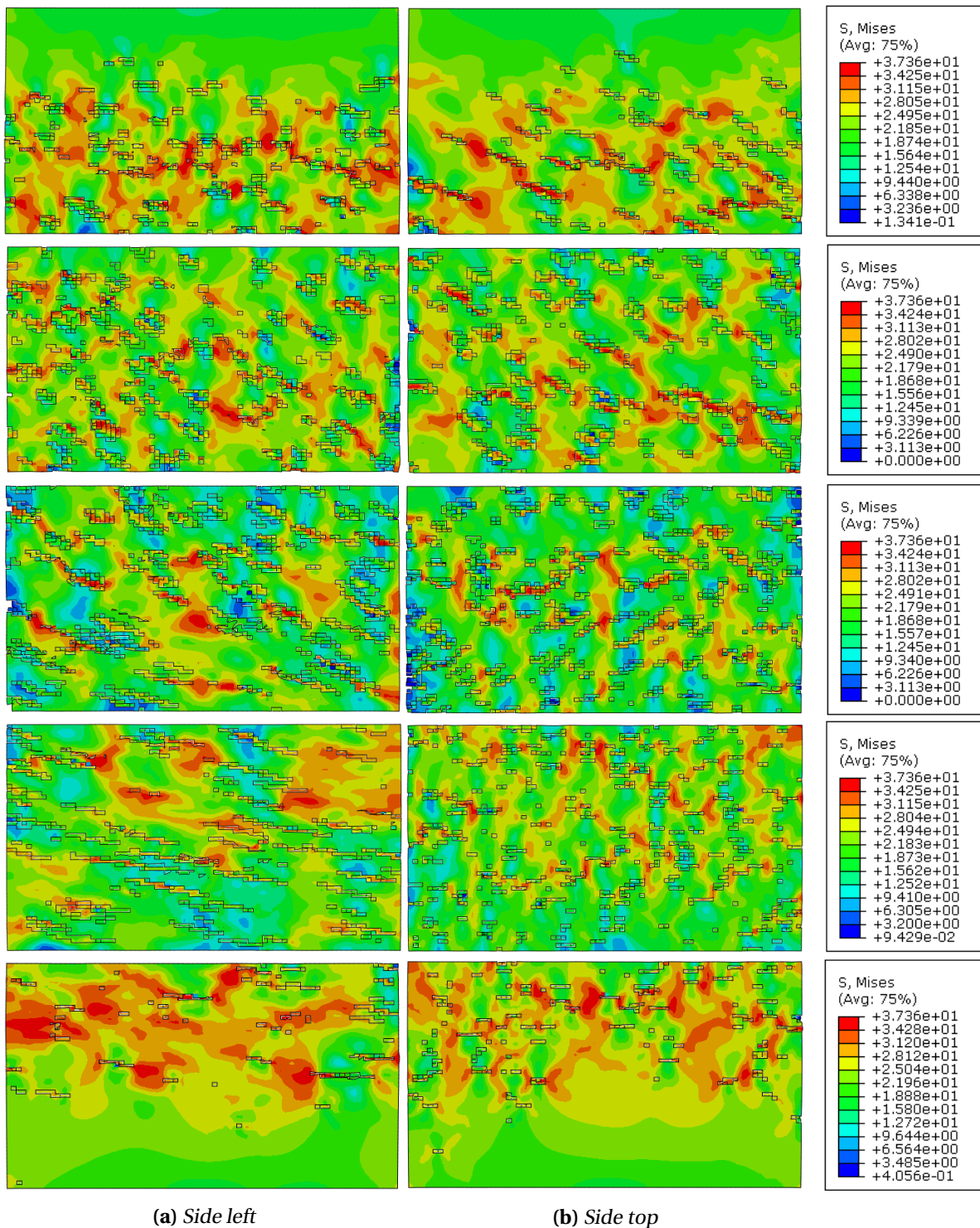


Figure 6.22: Stress distribution at yielding in the middle of the specimens, cut in two perpendicular directions, side left and side top. Each row correspond to one specimen, where the top row is EH1 and the bottom is EH5.

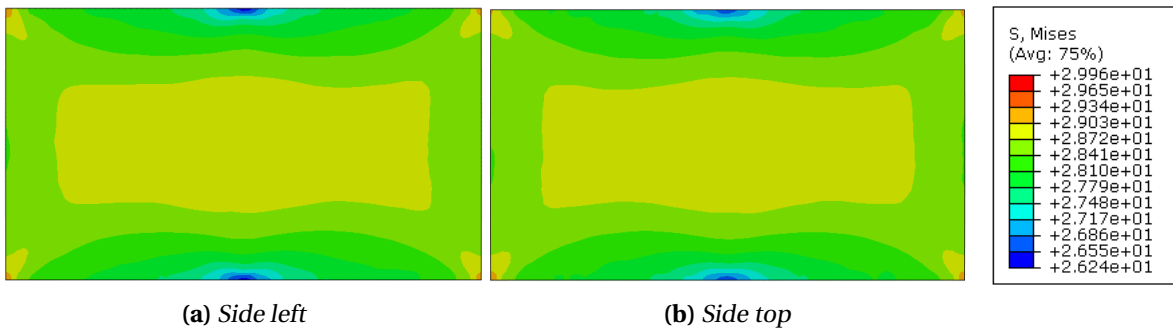


Figure 6.23: Stress distribution at a displacement of 0.23mm in the middle of the K1, cut in two perpendicular directions, side left and side top.

6.4.2 Block

The direct models of the specimens has shown satisfactory results and proved valuable when considering the internal behaviour. To further consider the interaction between the entire porous polypropylene layer and find out if it is possible with the direct modelling technique, a 60p300i model was established based on the CT-images from the block of the coating. The model is a replica of a column with dimensions of 10.85x10.85x39mm, extracted from the middle of the block (Fig. 6.24), thus spanning over the entire porous PP layer. In this way, all the specimens will be considered in the same analysis, and the model could give extended knowledge to the structural behaviour during compression of the coating. The model was established as the specimens in Section 6.3, consisting of 919,523 elements in the finished mesh. The model was added symmetry boundary conditions to prevent the model from buckling. However, the simulation would be futile after the block densifies (with no transverse expansion the pores may produce large distortions).

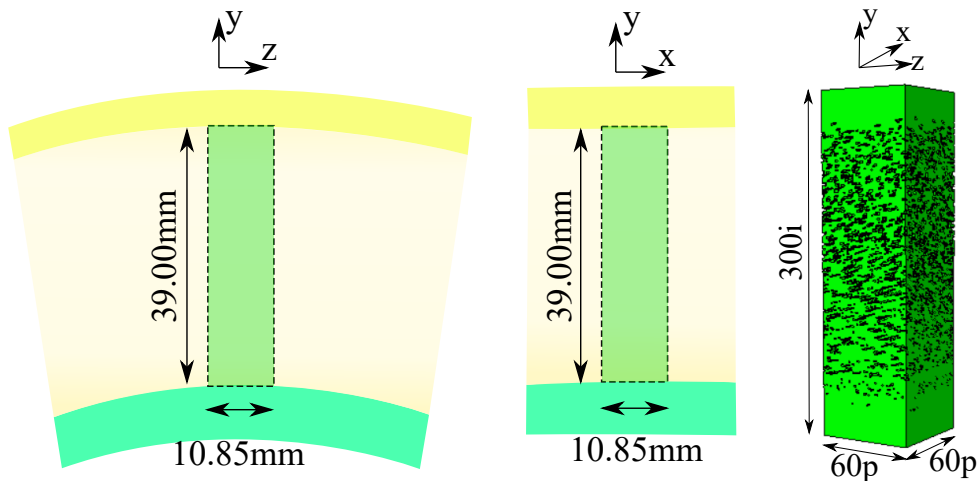


Figure 6.24: Illustration of the block, its measurements, and where it was extracted from.

In Figure 6.25, the simulation of the block is shown with a von Mises stress contour plot. The pictures illustrate how the stresses develop during compression. As can be seen, the middle is the first to yield. Then the stress distribution moves upwards before the bottom half starts to yield. The development of the stress distribution may be seen in relation to the relative density of the coating. The lowest relative density is found in the middle of the coating, and the upper part has a lower relative density than the bottom. These properties correlate with the stress distribution observed.

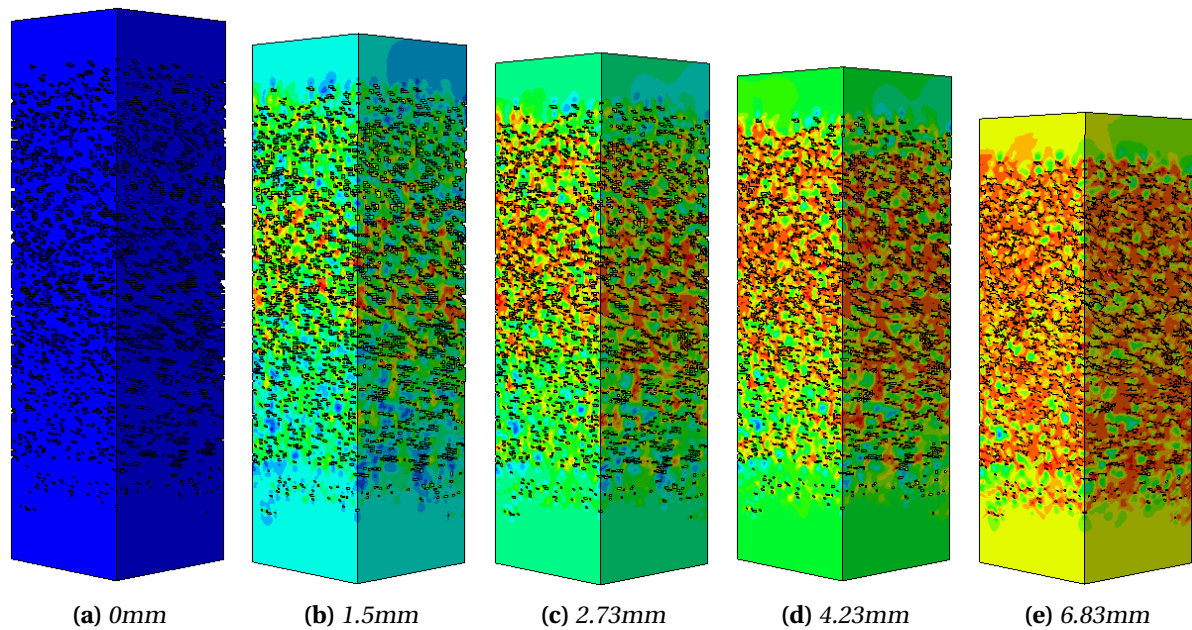


Figure 6.25: Column of the porous layer of the coating subjected to compression in radial direction. The colours represent the von Mises stress, where the red equals the yield stress (37.3MPa).

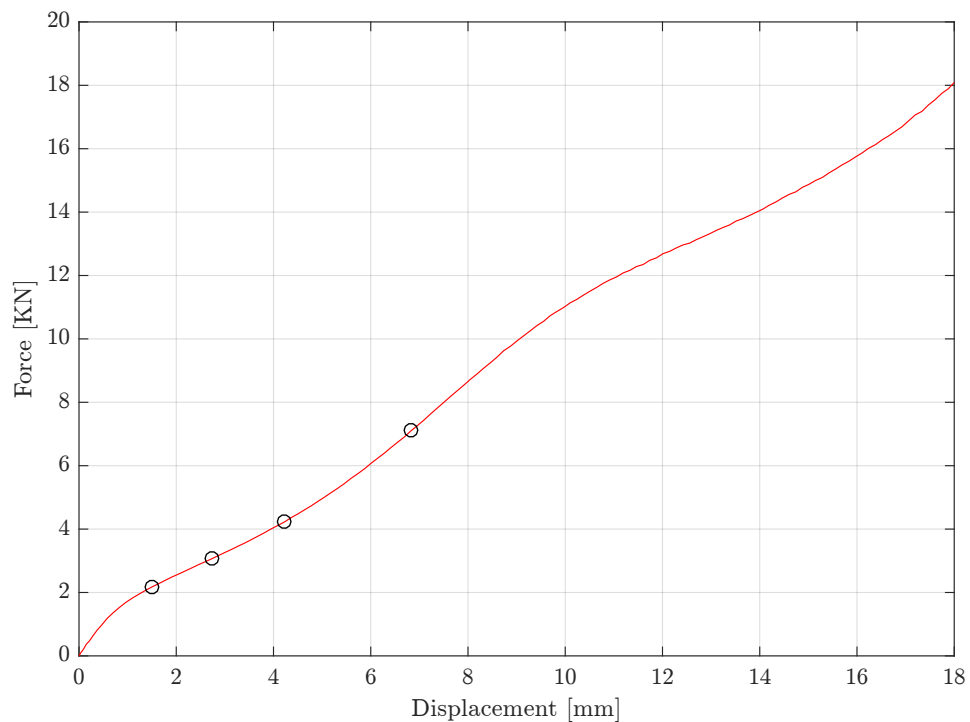


Figure 6.26: FD curve of the column with symmetrical boundary conditions at each side. The circles on the curve corresponds to displacements in Fig. 6.25. Note that the model shows clear signs of element distortions at a displacement of 10mm.

Figure 6.26 shows the FD-curve to the column. The curvature the first 8mm, could be explained by the observed stress distribution. The localised yielding in the middle causes a low yield point, followed by a steady increasing force, as more of the coating yields. When the coating starts to densify the curve gets steeper. From Figure 6.25d to Fig. 6.25e there can be observed that most of the porous parts have yielded and that the poreless parts towards the periphery experience an increased stress, thus indicating the densification. At a displacement of about 10mm the curvature changes. The model shows at this point clear signs of element distortion in the pores. The change in curvature observed is probably related to these distortions, rendering the FD results useless after this point. It was observed that the curvature resembles the compression results of a similar but larger block in [11].

6.4.3 Mechanical anisotropy

From the characterisation of the morphology of the pores, it was clear that mechanical anisotropy should be present in the porous coating. No experiments were conducted to validate this, but the numerical models re-created from the specimens could prove useful in this matter.

The material model used in the numerical re-creations do not account for anisotropy. Remember that polymers generally show an anisotropic response (Sec. 5.1). However, the models may describe mechanical anisotropy due to the inhomogeneous pore morphology. To investigate the property, new models were created. The models were established by the direct modelling technique to extract a cube from the specimens (Fig. 6.27). The cube was compressed in radial (r), axial (z) and hoop (θ) direction.

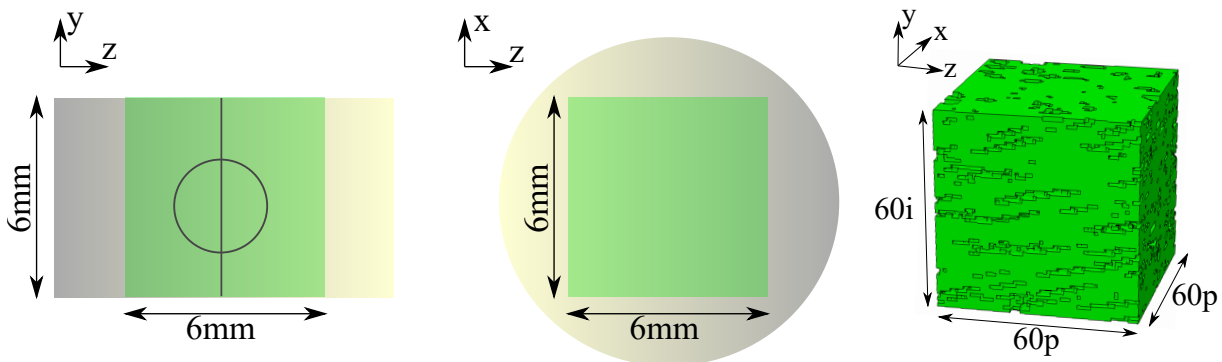


Figure 6.27: The cube used to test for mechanical anisotropy and its measurements. The green squares indicate where the cube was extracted from the specimens.

In Figure 6.29 (a-e), the force-displacement curves for the cubes compressed in the three different directions are depicted. The plots suggest that the cubes are weakest when compressed in the radial direction for displacements beneath 2mm. The result in the axial and hoop directions seem to coincide, but the z -direction gives an averagely stronger behaviour. The same results were observed in [12], where a similar experiment was conducted on physical specimens, providing confidence to the simulations. The curves appears to converge at larger displacements, due to densification.

In Figure 6.29f, the level of anisotropy is illustrated in a simplified way; the difference in force (Δ Force) between two directions are plotted for each cube. The force is obtained from where the difference is large, which was chosen to be at a displacement of 0.5mm. As the figures suggests, the level of anisotropy is dependent on which cube tested. That indicates that the underlying pore structure

affects the mechanical anisotropy.

In Section 5.2, the characterisation analyses suggested that the pore morphology was highly inhomogeneous and anisotropic, and depending on the radial coordinate. That property was assumed to cause mechanical anisotropy in the coating, with a different magnitude in the r-direction. The simulation results seemed to capture the expected behaviour; a low level of mechanical anisotropy for EH2, while EH4 has a higher level. Note that specimen cubes EH1 and EH5 has a high level of mechanical anisotropy because of the high relative density in the top or bottom (radial-direction) of the cubes.

6.4.4 Tension

In an impact event on the coated pipeline, the indenter produces compression behaviour where the impact happens. However, as in the case of Kvitebjørn (Sec. 1.1), the pipeline was dragged, and bending was present. So there would be tension on the other side of the pipe (corresponding to where the indenter impacts the pipe). A final numerical model should, therefore, be able to account for this consequence of the impact as well. In this section the direct models of the specimens are stretched in the radial direction, by translating the top surface, to investigate their ability to describe tension behaviour in the coating. Note that the results are not validated by any experiments.

The experiments conducted in this thesis did not include any tension tests of either the porous or solid polypropylene. The material model in tension was calibrated with a linear Drucker-Prager model (Sec. 5.4.1), where the tension data used was taken from the literature and the manufacturer of the PP (Tab. 5.1). With the utilisation of the DP-model, the force-displacement curves were assumed to be more realistic than if the compression data was used only. As discussed in Section 5.1, polymers show a pressure sensitive response. However, the numbers should be observed with a critical view.

In Figure 6.32, the results of the simulations of the EH specimens in tension are displayed (no fracture). This result illustrates a strong strain localisation. Note that the strain band is not horizontal, it follows the path between the largest pores in each specimen. Also, large distortion of the elements is present and void (pore) growth (Fig. 6.28).

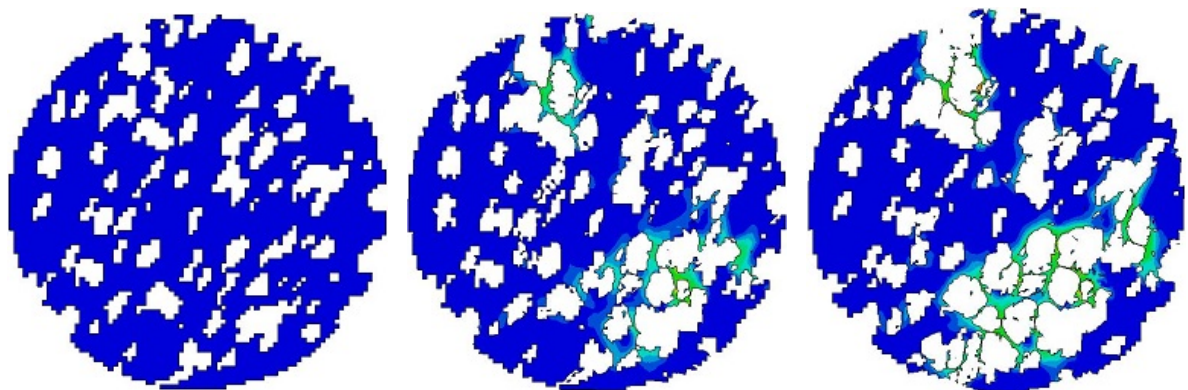


Figure 6.28: EH3 tension simulation results illustrated by one slice in the middle. No fracture was included in the numerical model. The strain localisation and void growth are visible.

It was observed that the equivalent plastic strain localised so that the surface with the lowest area

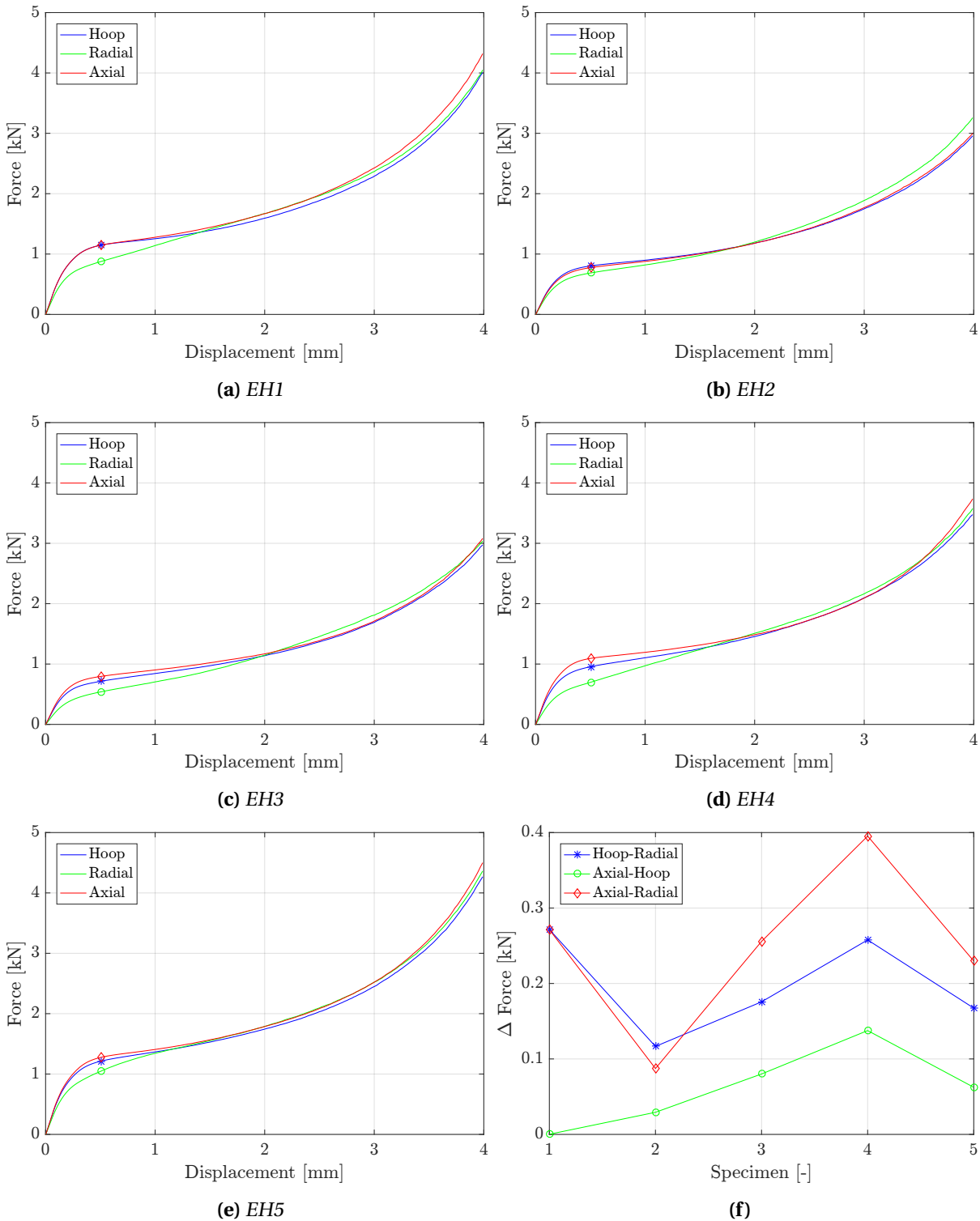


Figure 6.29: Figures (a)-(e) depict the force-displacement curves for the specimen cubes, compressed in three different directions. (f) illustrates the level of anisotropy by comparing the difference in force between two compression directions. The force is gathered at a displacement of 0.5 mm, illustrated by the points at the curves.

started to neck, i.e. the largest pores determines where the yielding surface appear. Considering the relative density of the coating (Fig. 5.3), the lowest area seems to be found in the middle of the porous PP layer (EH3), which may explain why the strain localisation happens closer to the centre of the coating. The RD of specimen EH1 and EH5 are quite steep, resulting in the fracture occurring almost entirely at the end of the samples.

Failure was assumed to take place where the distortions are large, i.e. in the localised strain bands. Therefore a simple failure criterion was added the numerical models. A fracture model was not calibrated, but a ductile damage evolution with a constant fracture strain surface (Sec. 2.1.3) was used. The fracture strain was set to 1.0. In Figure 6.30, the simulation result of EH3 subjected to tension with a fracture criterion is shown. The simulations of the rest of the EH specimen behaved the same way; the fracture happened where the strain localises (Fig. 6.32).

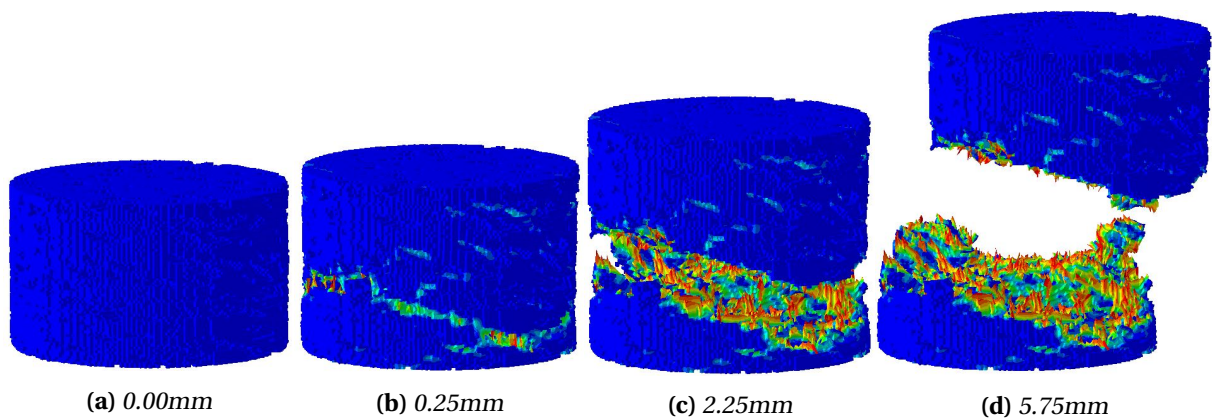


Figure 6.30: EH3 tension simulation results with a fracture criterion. Each image displays the equivalent plastic strain at the corresponding displacement (of top part). Note that the two parts move away from each other in the horizontal directions as well as the vertical.

Although the simulations were conducted as a test of the direct modelling technique's ability to describe the tension in the coating, a possible characteristic of the mechanical behaviour of the porous polypropylene was observed. The failure mechanics was ductile; the void growth and coalescence were seen in the results as partly illustrated in Figure 6.28. The theory of ductile damage (Sec. 2.1.3) state that fracture occurs due to nucleation, void growth (and strain localisation) and coalescence. These phenomena are observed in the simulation results, all except nucleation (voids are already present).

In Figure 6.31, the force-displacement curves of tension simulations are plotted (with and without a fracture criterion). The stapled curves are the result without fracture. It was observed that a fracture strain of 1.0 led to the same peak force as without a failure criterion. After the peak, the elements starts to erode, and the force quickly reduces as the displacement increases. The specimens create an order resembling the beginning of the compression tests (Fig. 6.21). EH5 with the highest capacity followed by EH1, then EH2 and EH4, and EH3 with the lowest capacity.

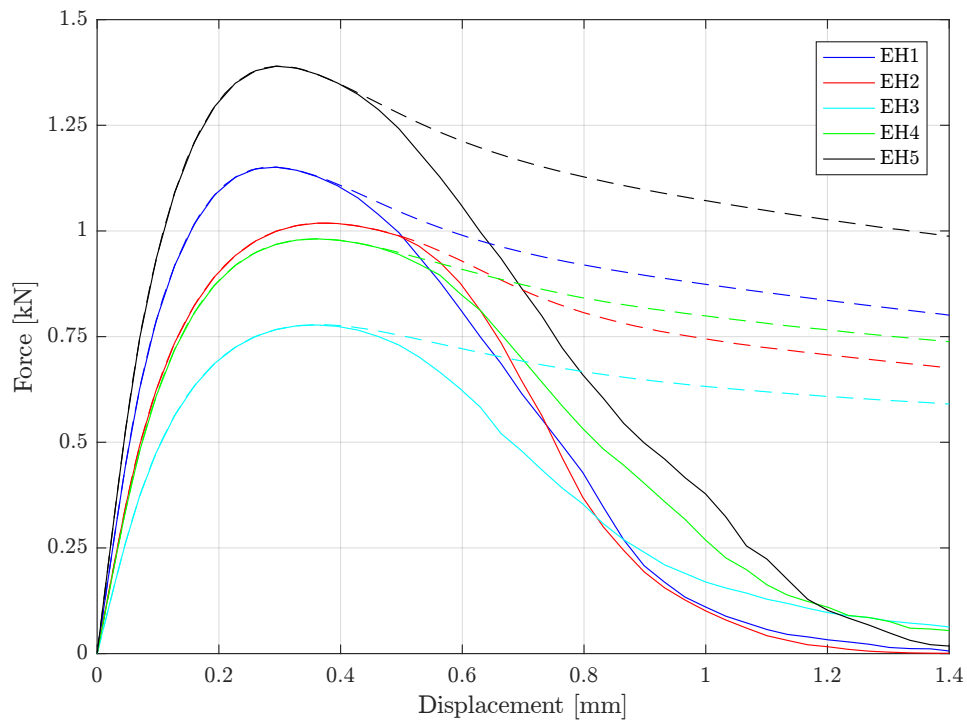


Figure 6.31: FD curves for all specimens stretched in the radial direction. For the whole lines, the model fracture at a strain of 1.0, while the stapled line has no fracture criteria.

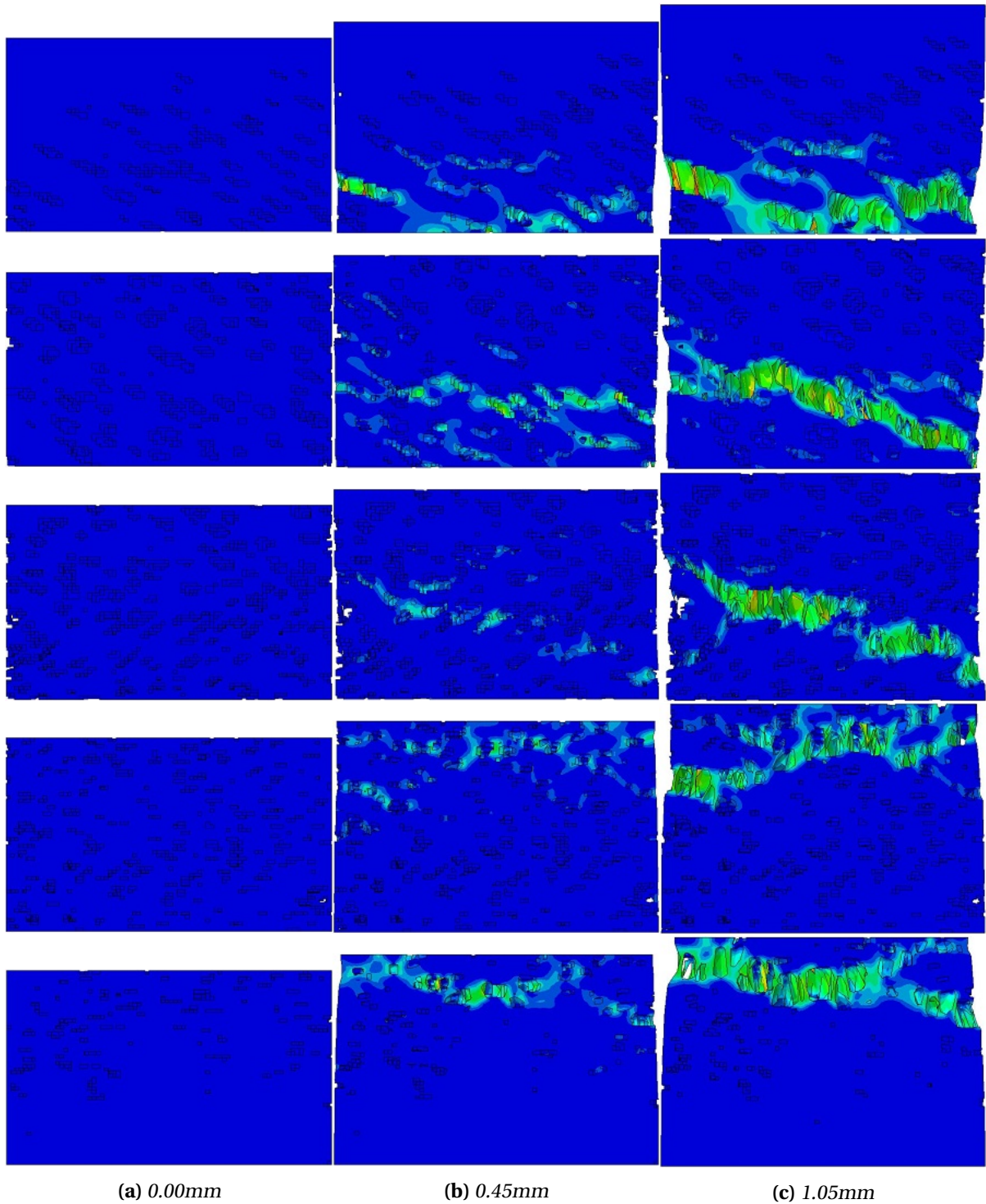


Figure 6.32: *EH series tension simulation results without fracture criteria. Each row corresponds to one specimen, where the top row is EH1, and the bottom one is EH5, and each column corresponds to a certain displacement of the specimen. The colours represent the amount of plastic equivalent strain (PEEQ), where blue is relatively zero strain. The strain localisation and void growth are observable. Coalescence is not, due to the excluded fracture criteria.*

6.5 Summary and discussion

A direct modelling technique was established to create numerical replications of the pore morphology of the coating. The method used X-ray computed tomography image slices to re-create parts of the coating with cuboid elements where the slices showed matrix material. The method was used to establish replications of the specimens subjected to uniaxial compression, which were employed in an attempt to further characterise the mechanical behaviour of the coating.

A sensitivity study was conducted on the numerical re-creations of the specimens. The method used to establish the direct models made it natural to start the study by determining the mesh size sensitivity. The results indicated that the force-displacement curve for the model converged towards the experimental values as the mesh got finer but with a rapidly increasing simulation time. An 80p60i re-creation was chosen for further studies, as it showed promising results with a reasonable simulation time. Other studies indicated that the numerical models were sensitive to the friction coefficient and the material model. Element type and imperfections seemed not to affect the resulting force-displacement curves. Note that the studies were mostly conducted on specimen EH4; the sensitivity of the different parameters may be different for the other models. However, it was assumed that the complex pore morphology of EH4 made it the most parameter sensitive specimen.

Based on the results found in the sensitivity study, replications of every specimen was created and subjected to uniaxial compression. The resulting FD curves were compared to the experimental, which showed that the simulations were a bit too strong but able to capture the general trend of the curves. The increased strength could be caused by a too coarse mesh.

The internal behaviour of the porous specimens during compression was investigated. The study indicated that the long and slant pores in the lower half of the coating (EH4) caused the specimen to yield with a low force. Also, the shape of the pores resulted in crushing of the pores early, so that the densification makes the slope of the curve high. The round and large pores at the top led to a stronger response at yielding, but a flat plateau.

A block of the entire polypropylene layer was established to investigate the behaviour of the coating during compression. The simulations suggested that the middle of the layer yields first, then the upper part, followed by the lower. The relative density of the coating correlates well with this result.

As the numerical models showed promising results, the direct modelling technique was used to further analyse the coating and test its capabilities to describe other mechanical properties than compression. The mechanical anisotropy of the specimens and its capacity in tension was tested.

To test for anisotropy, a cube was cut out of the specimens and compressed in all three directions. The simulations revealed an apparent difference in the compressive behaviour in the radial direction compared with the axial- and hoop direction. It was also noted significant variations between the specimens, where the lower half seemed to be more anisotropic than the top. These differences may be seen in relation to the differences in the morphology of the pores, where the long pores at the lower half are likely to cause more anisotropy than the round ones at the upper half. For the specimens, EH1 and EH5, the high relative density parts towards the periphery, are assumed to increase the strength for compression in the hoop- and axial direction, giving a high mechanical anisotropy.

Tension test simulations of the specimens were conducted. Strain bands were formed between the

largest pores. The strain localisation was developed towards the middle of the coating and seemed to be initiated at the lowest values of the RD curve. The models were run both with and without a fracture criteria. Both simulations appeared to be failing at the same place and had the same yield point. The resulting FD curves showed the same formation as observed in compression.

For the tests on mechanical anisotropy and tension of the numerical model, no experiments were conducted to validate the results. The test on mechanical anisotropy is likely to give reasonable results. The models have proved good results for compression on different pore structures, and compression in other directions is simply the same as having a different pore structure. Also, the results found were coinciding with similar experimental results in [12]. The results for the tension tests are less trustworthy; the material model for the matrix material are not optimised for tension, and there was no similar experiment to verify the results. Nonetheless, the simulations suggest that the direct modelling technique is capable of capturing the desired mechanical properties.

In the paper by Hegdal et al. [16], a porous coating was broken into smaller pieces and analysed for thermal effects. The pieces were further re-created numerically, in a similar way as herein, and studied for the thermal effects. The thermal properties of the solid material were used in the model. The results from the simulations were found to be in good agreement with the experimental data. The satisfactory results from both thermal simulation and the mechanical simulation could indicate that direct models could provide reasonable results when subjected to various tests, as long as a suitable material model of the matrix material has been calibrated.

The problem with the direct modelling technique used to re-create the CT-scanned specimens is that they require a lot of elements. The models are also mesh-sensitive; a fine mesh was necessary to capture the pore structure. The 80p60i models established herein used over 250,000 elements. If the whole coating were to be established the same way it would require a number of elements in the billions. The models are more suitable to study smaller parts of the coating, and then use the information from that study to calibrate material models that account for the pore structure.

Concluding remarks

The mechanical properties of the Thermostat [13] coating solution applied to offshore steel pipes for thermal insulation was further investigated. The preliminary studies indicated that the steel material was sufficiently characterised, but not the polymer coating. X-ray computed tomography scans and uniaxial compression tests were conducted on specimens extracted from the porous polypropylene layer. The results were analysed and used to understand the behaviour of the material. A direct modelling technique was employed, and compression and tension simulations were conducted to characterise the coating further and demonstrate the capabilities of the numerical models. In this chapter, the conclusions based on said work, and recommendations for further work, is presented.

7.1 Conclusions

As a result of the experiments, analyses and simulations conducted in this thesis, there were several concluding remarks to make. The conclusions are presented in the following lists.

X-ray computed tomography scans indicated that

- the pore morphology of the coating is inhomogeneous and anisotropic. The pore structure vary significantly in the radial direction, but not in the other directions.
- the relative density varies from 0.7 to 1.0 depending on the radial coordinate, the lowest value is located in the centre, and it is not symmetric about that point.
- the coating is not a foam, but a solid with isolated pores due to the high relative density.
- a transition zone is located in the middle of the porous polypropylene layer where the pore structure changes significantly. The change in morphology was assumed to be the extrusion process during manufacturing.

Uniaxial compression tests imply that

- the pore structure affects the compressive strength of the coating and that different morphology has various effects.
- a low relative density results in a weaker response due to the reduced area.
- the transverse expansion is reduced due to the relative density. It was found that the specimen with the lowest RD (EH3) expanded about 50% of the solid PP specimen K1.
- the mechanical behaviour of polypropylene is affected by strain rate.
- the polypropylene material exhibit softening as well as work hardening.

Numerical simulations suggested that

- the direct modelling technique were able to capture the the pore morphology's effect on the mechanical response.
- the numerical models are sensitive to mesh size, friction and the material model.
- the yielding of porous polypropylene happen at a lower force due to strain localisation between the pores.
- there are significant mechanical anisotropy in the coating.
- the coating is significantly stronger in compression than tension where strain is strongly localised due to pore structure.
- the failure mechanism in tension is void (pore) growth and coalescence.

7.2 Recommendations for further work

This thesis was a part of an ongoing research collaboration between Statoil and SIMLab. Accurate numerical models will be an invaluable aid when predicting the state of the pipe after an impact event. Much work remains to achieve that. Recommendations for further work are presented in the following.

The porous polypropylene layer need further characterisation, preferably in 3D; the analysis of the pores should take into account the curvature of the coating (hoop direction), and statistics could be made of the actual number of pores, and their three-dimensional size, volume and orientation.

The other layers in the coating solution (solid polypropylene and outer shield) is of interest concerning the mechanical properties. A proper description of them is necessary for a complete numerical model of the coating and to accurately investigate the energy absorption capability of the system.

More layers may affect the pore structure. The porous polypropylene and outer shield layers can be repeated for better insulation, and the effect of this extension should be investigated.

Additional experiments is recommended; CT scans and mechanical compression/tension tests of the coating at different areas (hoop angles) of the pipe.

Solid polypropylene should be further investigated. Find out how sensitive the material is to temperature, strain rate and pressure. Calibrate a material model which also accounts for anticipated anisotropy.

The direct modelling technique could be further optimised. The direct models showed satisfactory results, but the mesh sensitivity may be too great to simulate the pipe. Other meshing techniques should be tried, such as tetrahedral elements that can vary in size and describe the pores more accurately.

A generalised material model for the coating should be found for large scale simulations (impact on coated steel pipe). The direct modelling method may be employed to calibrate material models that capture the mechanical response without having to include the pores in the numerical model. Note that which material model to use may be difficult to identify, because of the complex pore morphology.

The insulation capabilities of the coating was assumed to be great. Since the main purpose of the coating is to work as a thermal insulator, the effects of the potentially significant difference in temperature over the coating (the water around offshore pipelines is about 4°C while the oil/gas inside

the steel pipe may be over 100°C) should be further investigated. In [16], the thermal conductivity has been studied and simulated for high-density polystyrene. It is recommended that similar simulations be run with mechanical compression and find out how an impact event changes the conductivity. The direct modelling technique could be employed here.

To investigate the joints between the pipes, where the steel is welded, and a solid polyurethane is added (Sec. 3.2.1), is of interest.

Other coating solutions could be of interest to characterise (such as the Therмотite[®] ULTRA[™] [49]) because of the different manufacturing processes. A goal of the research is to optimise the coating solution based on both insulation and mechanical (energy absorption) properties. It was assumed that the manufacturing process affected the pore structure, and, therefore, possibly the mechanical and thermal properties.

Bibliography

- [1] Statoil. Production resumed at kvitebjørn. <https://www.statoil.com/en/news/archive/2008/01/18/KvitebjornProd.html>. Cited: 16.05.2017.
- [2] Statoil. Small gas leak from kvitebjørn pipeline. <https://www.statoil.com/en/news/archive/2008/08/20/gasleakkvitebjorn.html>. Cited: 16.05.2017.
- [3] Petroleum Safety Authority Norway. Damage and incidents involving load-bearing structures and pipeline systems. <http://www.ptil.no/aging-and-life-extention/damage-and-incident-involving-load-bearing-structures-and-pipeline-systems-article430.html>. Cited: 16.05.2017.
- [4] M. Kristoffersen. *Impact against X65 offshore pipelines*. Phd thesis, Norwegian University of Science and Technology, 2015.
- [5] K. Slåttedalen and A. Ørmen. *Impact against offshore pipelines*. Master's thesis, Norwegian University of Science and Technology, 2010.
- [6] J. Fornes and S. Gabrielsen. *Impact against offshore pipelines*. Master's thesis, Norwegian University of Science and Technology, 2011.
- [7] M. S. Hovdelien and V. Aune. *Impact against offshore pipelines*. Master's thesis, Norwegian University of Science and Technology, 2012.
- [8] T. I. Asheim and I. Mogstad. *Impact against offshore pipelines*. Master's thesis, Norwegian University of Science and Technology, 2013.
- [9] E. Jakobsen. *Deformation of pressurized pipelines*. Master's thesis, Norwegian University of Science and Technology, 2013.
- [10] E. Digerud and K. Lofthaug. *Bending of x65 offshore steel pipes*. Master's thesis, Norwegian University of Science and Technology, 2014.
- [11] N. L. Holm and E.T. Røshol. *Denting of coated and uncoated offshore steel pipes*. Master's thesis, Norwegian University of Science and Technology, 2015.
- [12] O. Vestrum, M. Kristoffersen, M. Langseth, T. Børvik, M. A. Polanco-Loria, and H. Ilstad. Quasi-static and dynamic deformation of polymer coated pipes. *International Conference on Ocean, Offshore and Arctic Engineering*, ASME-36, No. 1:63–66, 2017.
- [13] Bredero Shaw. Thermotite: Polypropylene insulation system. <http://www.brederoshaw.com/solutions/offshore/thermotite.html>. Cited: 24.02.2017.

- [14] Borealis AG. Ba202e. <http://www.borealisgroup.com/en/polyolefins/products/Others/BA202E/>. Cited: 24.02.2017.
- [15] T. R. Tofteberg, J. P. Hegdal, Å. G. Larsen, T. Schjelderup, and E. L. Hinrichsen. Determining the morphology of chemically foamed pipe coating using image segmentation. Technical report, Sintef, NTNU, Bredero Shaw Norway, 2011.
- [16] J. P. Hegdal, T. R. Tofteberg, T. Schjelderup, E. L. Hinrichsen, F. Grytten, and A. Echtermeyer. Thermal conductivity of anisotropic, inhomogeneous high-density foam calculated from three-dimensional reconstruction of microtome images. Technical report, NTNU, Sintef, Bredero Shaw Norway, 2013.
- [17] O. S. Hopperstad and T. Børvik. *Materials mechanics Part I*. NTNU, Trondheim, Norway, 2015.
- [18] O. S. Hopperstad and T. Børvik. *Materials mechanics Part II*. NTNU, Trondheim, Norway, 2015.
- [19] R. D. Cook, D. S. Malkus, M. E. Plesha, and R. J. Witt. *Concepts and Applications of Finite Element Analysis*. Wiley, 4 edition, 2001.
- [20] K. M. Mathisen, 2016. Lecture Notes TKT4197 - Nonlinear Finite Element Analysis. SIMLab - Structural Impact Laboratory.
- [21] SIMULIA. Abaqus analysis user's guide, v6.14. <http://50.16.225.63/v6.14/books/usb/default.htm>, 2017. Cited: 20.02.2017.
- [22] Inc. ABAQUS. Lecture 6 - adaptive meshing and distortion control. <http://imechanica.org/files/16-adaptive-mesh.pdf>. Cited: 21.03.2017.
- [23] L. Salvo, P. Cloetens, E. Maire, S. Zabler, J.J. Blandin, J.Y. Buffière, W. Ludwig, E. Boller, D. Bellet, and C. Josserond. X-ray micro-tomography an attractive characterisation technique in materials science. *Nuclear Instruments and Methods in Physics Research*, B 200:273–286, 2003.
- [24] James R. Janesick. *Scientific Charge-Coupled Devices*. Spie Press, Bellingham, Washington USA, 2001.
- [25] J. F. Barrett and N. Keat. Artifacts in ct: Recognition and avoidance. *RadioGraphics*, 24(6):1679–1691, 2004. PMID: 15537976.
- [26] L. J. Gibson and M. F. Ashby. *Cellular Solids: Structure and properties*. Cambridge University, United Kingdom, Cambridge, 2nd edition, 1997.
- [27] J. A. Rinde. Poisson's ratio for rigid plastic foams. *Journal of Applied Polymer Science*, 14(8):1913–1926, 1970.
- [28] R. Lakes. Foam structures with a negative poisson's ratio. *Science*, 235(4792):1038–1040, 1987.
- [29] Nobuyuki Otsu. A threshold selection method from gray-level histograms. *IEEE Transactions on Systems, Man, and Cybernetics*, SMC-9, No. 1:63–66, 1979.
- [30] MathWorks. Matlab r2017a documentation. <https://se.mathworks.com/help/>. Cited: 17.03.2017.
- [31] A. Ghiotti, S. Fanini, S. Bruschi, and P.F. Bariani. Modelling of the mannesmann effect. *CIRP Annals - Manufacturing Technology*, 58:255–258, 2009.
- [32] M. Kristoffersen, T. Børvik, and M. Langseth. Quasi-static and dynamic denting of polymer

- coated and uncoated offshore steel pipes - material and component tests. Technical report, SIMLab - Structural Impact Laboratory, 2015.
- [33] Shawcor. Home page. <http://www.shawcor.com/>. Cited: 25.05.2017.
- [34] Bredero Shaw. Thermoflo: Polyurethane thermal insulation systems. http://brederoshaw.com/solutions/offshore/fj_thermoflo.html. Cited: 04.06.2017.
- [35] Mitutoyo. Mitutoyo home page. <http://www.mitutoyo.com/>. Cited: 16.03.2017.
- [36] Shinko/Vibra. Shinko weighing scales, dj series. <http://www.vibra.co.jp/global/discontinued/DJ.html>. Cited: 16.03.2017.
- [37] Nikon. Xt h 225 st industrial ct-scanning. http://www.nikonmetrology.com/en_EU/Products/X-ray-and-CT-Inspection/Computed-Tomography/XT-H-225-ST-Industrial-CT-Scanning. Cited: 17.03.2017.
- [38] ImageJ. Home page. <https://imagej.nih.gov/ij/>. Cited: 17.03.2017.
- [39] Instron. 5980 floor model systems for high-capacity universal testing. <http://www.instron.us/en-us/products/testing-systems/universal-testing-systems/electromechanical/5900/5980-floor-model>. Cited: 03.04.2017.
- [40] E. Fagerholt. *Field Measurements in Mechanical Testing Using Close-Range Photogrammetry and Digital Image Analysis*. Phd thesis, Norwegian University of Science and Technology, 2012.
- [41] Allied Vision. Prosilica gc2450. <https://www.alliedvision.com/en/products/cameras/detail/Prosilica%20GC/2450.html>. Cited: 03.04.2017.
- [42] Samyang. 100mm f2.8 ed umc macro. <https://www.samyanglensglobal.com/product/detail.do?SQ=3>. Cited: 03.04.2017.
- [43] Molykote. Molykote g-n metal assembly paste. <http://www.dowcorning.com/applications/search/products/details.aspx?prod=01889877&type=PROD>. Cited: 03.04.2017.
- [44] J. Halary, F. Laupretre, and L. Monnerie. *Polymer Materials: Macroscopic Properties and Molecular Interpretations*. Wiley, Hoboken, NJ, 1st edition, 2011.
- [45] P.A. Du Bois, S. Kolling, M. Koesters, and T. Frank. Material behaviour of polymers under impact loading. *International Journal of Impact Engineering*, 32(5):725 – 740, 2006. International Symposium on the Crashworthiness of Light-weight Automotive Structures International Symposium on the Crashworthiness of Light-weight Automotive Structures.
- [46] SIMULIA. Abaqus scripting user's guide, v6.14. <http://50.16.225.63/v6.14/books/cmd/default.htm>, 2017. Cited: 20.02.2017.
- [47] Inc. ABAQUS. Lecture 1 - overview of abaqus/explicit. <http://imechanica.org/files/0-overview%20Explicit.pdf>. Cited: 20.02.2017.
- [48] Inc. ABAQUS. Lecture 2 - elements. <http://imechanica.org/files/12-elements.pdf>. Cited: 12.03.2017.
- [49] Bredero Shaw. Thermotite ultra: Superior subsea insulation. http://brederoshaw.com/solutions/offshore/thermotite_ultra.html. Cited: 04.06.2017.

CT scans

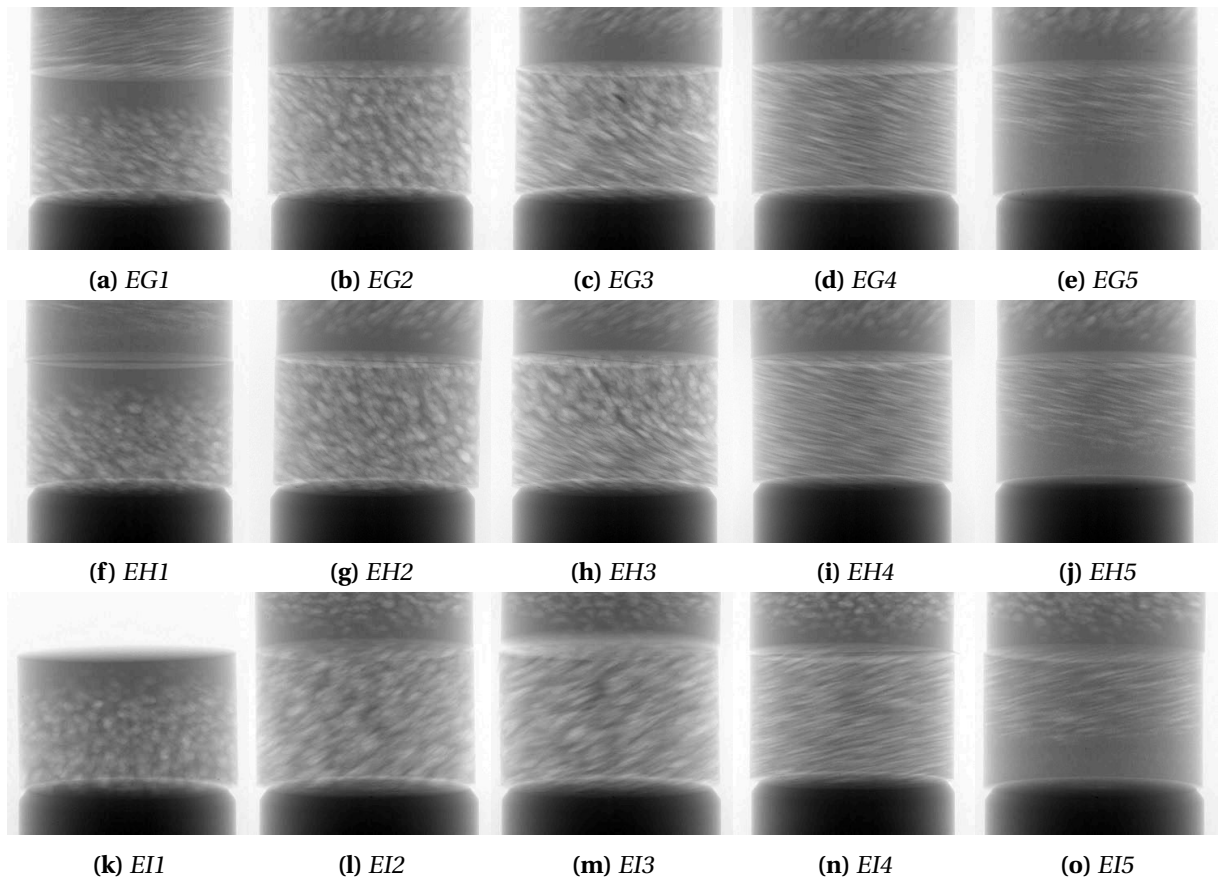


Figure A.1: CT scans of the specimens in raw format (not slices). Each image is at about the same angle of rotation.

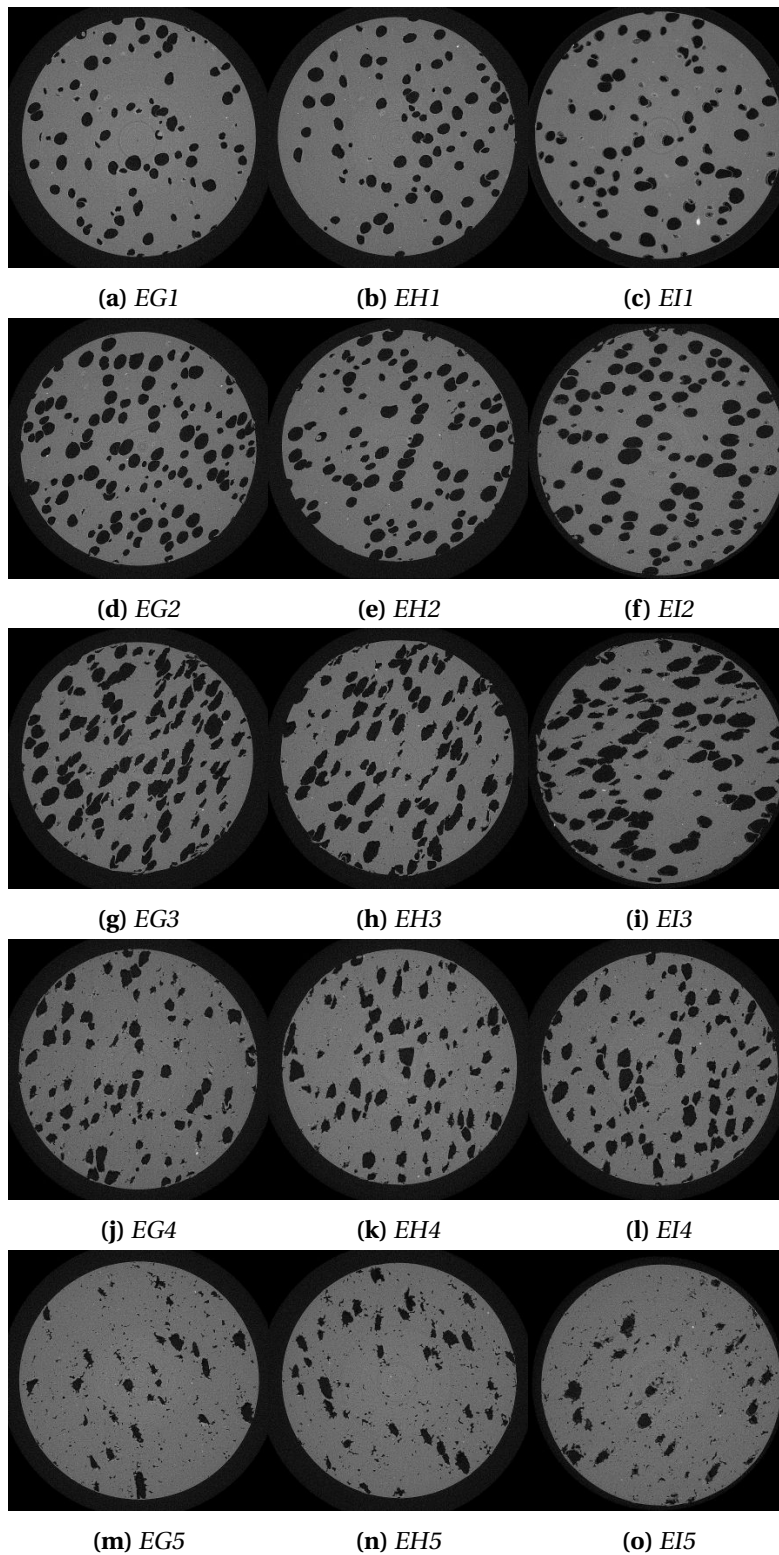


Figure A.2: CT scans of the specimens in 2D slice format (top-down). Each slice is in the middle of the corresponding specimen.

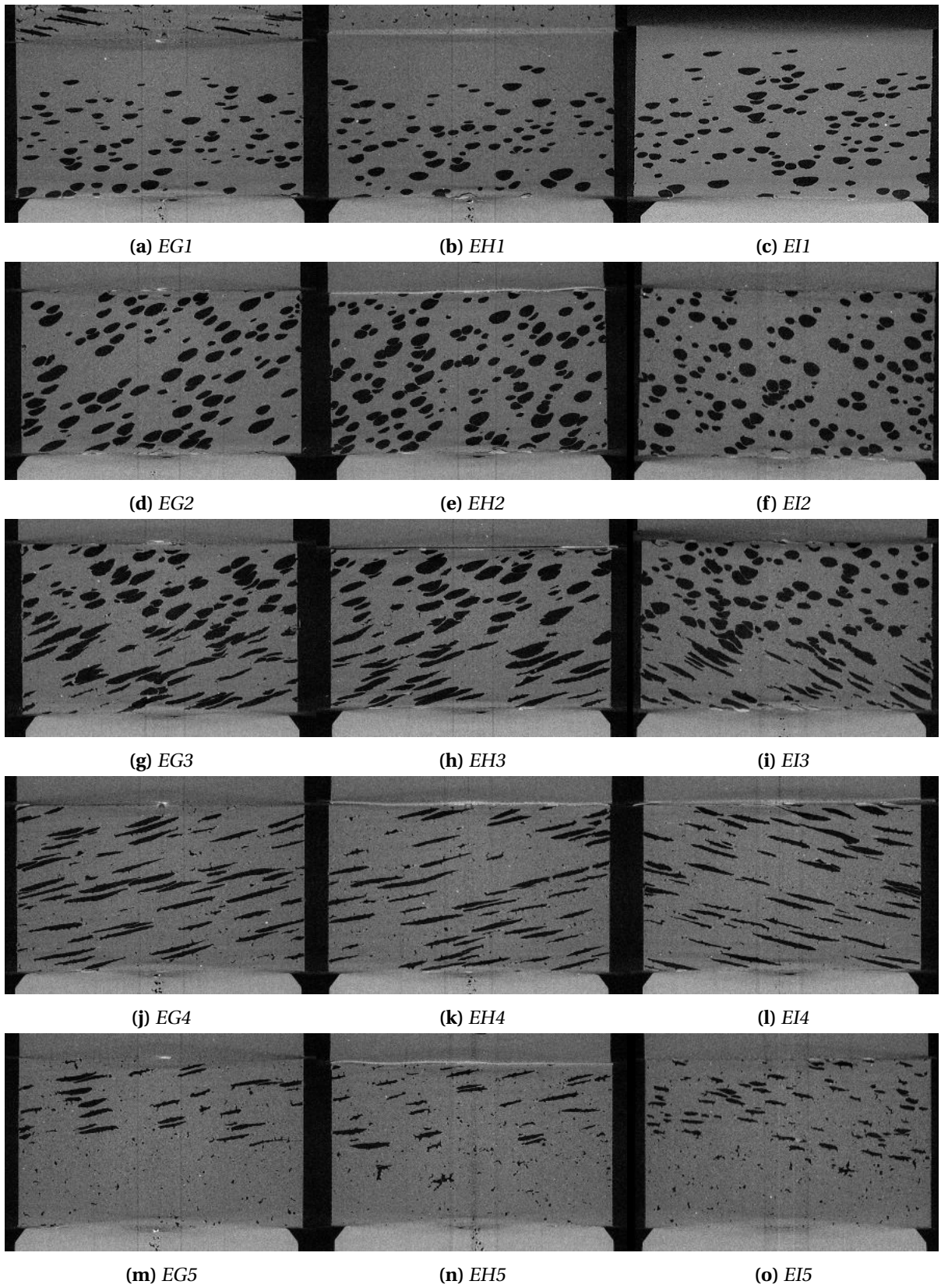


Figure A.3: CT scans of the specimens in 2D slice format (side left). Each slice is in the middle of the corresponding specimen.

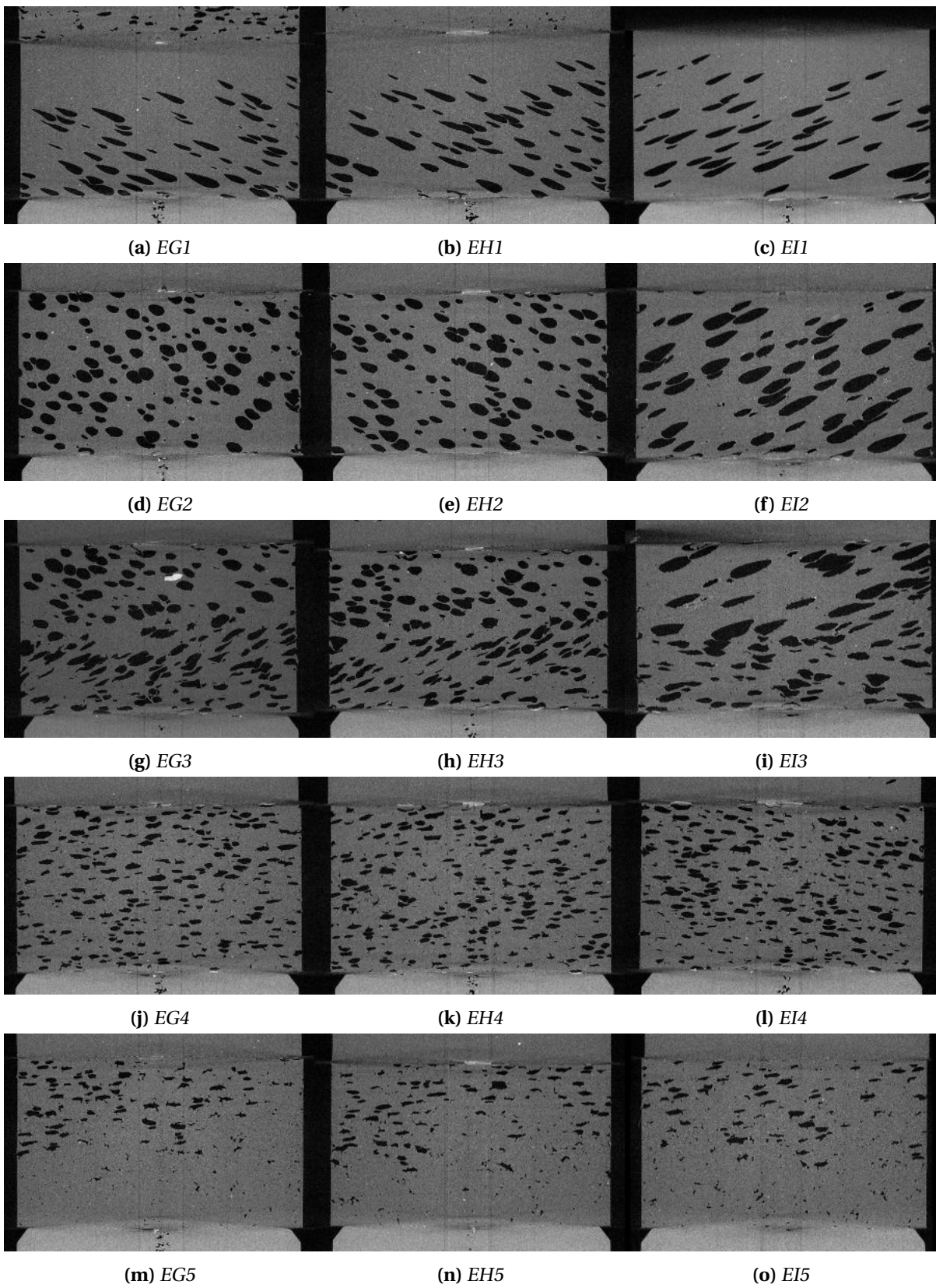


Figure A.4: CT scans of the specimens in 2D slice format (side top). Each slice is in the middle of the corresponding specimen.

Appendix B

Calculate mass by the use of relative density

To calculate the the mass from a relative density (RD) curve on a body, the well known equation

$$dM = \rho dV \quad (\text{B.1})$$

is employed, where dM is the mass, ρ is the density and dV is the volume. The area, A , of the surface in the body is assumed constant over the height (dz) and the density has a constant value, ρ_s , and the RD is a value between 0 and 1, ρ^* . Then eq. B.1 can be written as

$$dM = \rho_s \rho^* A dz \quad (\text{B.2})$$

Let n be the number of points (or increments) in height on which the body is discretized and i is the index of said points. It is assumed that the discretization is uniform, so that the height increment size ($dz = dh$) is constant. The increment mass is then calculated as

$$m_i = \rho_s \rho_i^* A dh \quad (\text{B.3})$$

The mass of the body is then the sum of all increments, i.e.

$$M = \sum_{i=1}^n m_i = \sum_{i=0}^n \rho_s \rho_i^* A dh \quad (\text{B.4})$$

Python script

```
#####  
# This scripts creates a model with cuboids based on binary text files.  
# The program is intended to replicate a porous specimen, in this case  
# a 80p60i re-creation of EH4.  
# Note that the script requires a text file with the plastic parameters  
# and binary text files telling where to place the cuboids.  
#####  
  
# To make features from Abaqus available to the script  
from part import *  
from material import *  
from section import *  
from assembly import *  
from step import *  
from interaction import *  
from load import *  
from mesh import *  
from optimization import *  
from job import *  
from sketch import *  
from visualization import *  
from connectorBehavior import *  
from abaqus import *  
from abaqusConstants import *  
import odbAccess  
  
import numpy as np  
import math  
  
session.journalOptions.setValues(replayGeometry=COORDINATE, recoverGeometry=  
    COORDINATE)  
  
#####  
# PRELIMINARIES  
#####  
workDirectory = 'D:/Skole/Masteroppgave/Abaqus/TestSpecimens/EH4/80p60i'  
modelName = 'EH4_80_60i'  
numberOfvoxels = 80  
numberOfImages = 60
```

```
os.chdir(workDirectory)                #Set work directory
mdb.Model(modelType=STANDARD_EXPLICIT, name=modelName) #Create a new model
if len( mdb.models.keys() ) == 2:      #Delete the default model if present
    del mdb.models['Model-1']

saveModel = 1          #If 1: save model
Cpus = 2               #Number of CPU's

#=====
#  MODEL PARAMETERS
#=====
#Material
materialName = 'Foam'
sectionName1 = 'Section-1'
rho = 9e-10          #Specify density
Emod = 1125.0        #Specify Youngs modulus
nu = 0.3             #Specify Poissons ratio

#Interaction
fricSurf = 0.025     #Surface friction
#Cretes a string to be used for the input file
if int(fricSurf*100)<10:
    fricToJobSurf = '_00%df' %int(fricSurf*1000)
else:
    fricToJobSurf = '_0%df' %int(fricSurf*1000)

fricInt = 0.10       #Internal friction
#Cretes a string to be used for the input file
if int(fricInt*100)<10:
    fricToJobInt = '_00%df' %int(fricInt*100)
else:
    fricToJobInt = '_0%df' %int(fricInt*100)

#Dimensions of Cylinder
lenXCube = 10        #Diameter in X-dir
lenYCube = 6         #Height
lenZCube = 10        #Diameter in Z-dir

#Information for inserting voxels into the assembly
lenXvoxel = lenZvoxel = float(lenXCube)/float(numberOfvoxels)
lenYvoxel = float(lenYCube)/float(numberOfImages)

#Information to insert rigid plates into assembly
hightSupport=-lenYvoxel*0.5 - 0.001
hightImpactor=lenYCube-lenYvoxel*0.5 + 0.001
rigidPlateSize = lenXCube*4

#Simulation
stepTime = 0.005     #Set length of simulation
velocity = (lenYCube*0.7)/stepTime #Set velocity

#=====
#  1. MATERIALS
#=====
#Set elastic parameters
mdb.models[modelName].Material(name=materialName)
mdb.models[modelName].materials[materialName].Density(table=((rho, ), ))
mdb.models[modelName].materials[materialName].Elastic(table=((Emod, nu), ))
```

```

#Set plastic parameters from text file
plasticTable = []
with open('PP_MM4.txt', 'r') as f:
    for line in f:
        data = line.split()
        numbers = (float(data[0]),float(data[1]))
        plasticTable.append(numbers)

mdb.models[modelName].materials[materialName].Plastic(table=tuple(plasticTable))

#=====
# 2. SECTIONS
#=====
mdb.models[modelName].HomogeneousSolidSection(material=materialName, name=
    sectionName1, thickness=None)

#=====
# 3. PARTS
#=====
#Create Small Cube (voxel)
voxelName = 'Voxel'
mdb.models[modelName].ConstrainedSketch(name='__profile__', sheetSize=300.0)
mdb.models[modelName].sketches['__profile__'].rectangle(point1=(-0.5*lenXvoxel,
    -0.5*lenYvoxel),
    point2=(0.5*lenXvoxel, 0.5*lenYvoxel))
mdb.models[modelName].Part(dimensionality=THREE_D, name=voxelName, type=
    DEFORMABLE_BODY)
mdb.models[modelName].parts[voxelName].BaseSolidExtrude(depth=lenZvoxel, sketch=
    mdb.models[modelName].sketches['__profile__'])
del mdb.models[modelName].sketches['__profile__']

#Mesh the voxel
mdb.models[modelName].parts[voxelName].seedPart(deviationFactor=0.1,
    minSizeFactor=0.1, size=lenZvoxel)
mdb.models[modelName].parts[voxelName].setElementType(elemTypes=(ElemType(
    elemCode=C3D8R, elemLibrary=STANDARD, secondOrderAccuracy=OFF,
    kinematicSplit=AVERAGE_STRAIN, hourglassControl=DEFAULT,
    distortionControl=DEFAULT), ElemType(elemCode=C3D6, elemLibrary=STANDARD),
    ElemType(elemCode=C3D4, elemLibrary=STANDARD)), regions=(
    mdb.models[modelName].parts[voxelName].cells.getByBoundingBox(-lenXvoxel,-
        lenYvoxel,-lenZvoxel,lenXvoxel,lenYvoxel,lenZvoxel), ))
mdb.models[modelName].parts[voxelName].generateMesh()

# Create rigid support/impactor plate
mdb.models[modelName].ConstrainedSketch(name='__profile__', sheetSize=
    rigidPlateSize)
mdb.models[modelName].sketches['__profile__'].Line(point1=(-rigidPlateSize*0.5,
    0.0), point2=(
    rigidPlateSize*0.5, 0.0))
mdb.models[modelName].sketches['__profile__'].HorizontalConstraint(addUndoState=
    False, entity=mdb.models[modelName].sketches['__profile__'].geometry[2])
mdb.models[modelName].Part(dimensionality=THREE_D, name='rigidPlate', type=
    ANALYTIC_RIGID_SURFACE)
mdb.models[modelName].parts['rigidPlate'].AnalyticRigidSurfExtrude(depth=
    rigidPlateSize,
    sketch=mdb.models[modelName].sketches['__profile__'])
del mdb.models[modelName].sketches['__profile__']
mdb.models[modelName].parts['rigidPlate'].ReferencePoint(point=(0.0, 0.0, 0.0))

#=====

```

```
# 4. ASSEMBLY
#=====
#Builds the specimen by importing, translating and merging the voxels, layer for
layer
#The process requires binary text files to determine where to place a voxel
voxelNr = mergedNr = rowNr = 0
rowList = instancesList = mergedInstancesList = []
for k in range (0,numberOfImages):
    #Read binary text file to decide where to place a voxel
    voxelList=np.loadtxt("Textfiles/bw%d.txt" %(k+1), ndmin=2)
    for i in range (0,len(voxelList)):
        for j in range(0,len(voxelList[i])):
            if voxelList[i][j]==0 :
                #Import a voxel to assembly
                mdb.models[modelName].rootAssembly.Instance(dependent=ON, name=
                    voxelName + '-%d' %voxelNr, part=
                    mdb.models[modelName].parts[voxelName])
                #Translate the voxel to correct place
                mdb.models[modelName].rootAssembly.translate(instanceList=(voxelName
                    + '-%d' %voxelNr, ),
                    vector=(lenXvoxel*j, lenYvoxel*k, lenZvoxel*i))
                #Put the voxel into a list
                instancesList.append(mdb.models[modelName].rootAssembly.instances[
                    voxelName + '-%d' %voxelNr])
                voxelNr +=1
            if len(instancesList)>1:
                #Merge all voxel from the first row in the text file
                mdb.models[modelName].rootAssembly.InstanceFromBooleanMerge(domain=MESH
                    ,
                    instances=tuple(instancesList), mergeNodes=BOUNDARY_ONLY, name='Row%
                    d' %rowNr, nodeMergingTolerance=0.0002,
                    originalInstances=DELETE)
                #Put the row into a list
                rowList.append(mdb.models[modelName].rootAssembly.instances['Row%d-1' %
                    rowNr])
                rowNr +=1
                #clear the voxel list before next row
                instancesList = []
        if len(rowList)>1:
            #Merge all rows into a layer
            mdb.models[modelName].rootAssembly.InstanceFromBooleanMerge(domain=MESH,
                instances=tuple(rowList), mergeNodes=BOUNDARY_ONLY, name='Merged%d' %
                mergedNr, nodeMergingTolerance=0.0002,
                originalInstances=DELETE)
            #Put the layer into a list
            mergedInstancesList.append(mdb.models[modelName].rootAssembly.instances['
                Merged%d-1' %mergedNr])
            mergedNr +=1
            #Clear the row list before next layer
            rowList = []
            #The merging process creates parts, which must be deleted
            for l in range(0,rowNr):
                del mdb.models[modelName].parts['Row%d' %l]
            rowNr=0

#Merge all levels into final MergedCylinder
mdb.models[modelName].rootAssembly.InstanceFromBooleanMerge(domain=MESH,
    instances=tuple(mergedInstancesList), mergeNodes=BOUNDARY_ONLY, name='
    MergedCylinder', nodeMergingTolerance=0.0002,
```

```

originalInstances=DELETE)

#Delete unnecessary parts (layers)
for i in range(0,(mergedNr)):
    del mdb.models[modelName].parts['Merged%d' %i]

if saveModel == 1:
    mdb.saveAs(pathName = modelName + '.cae')

#Import 2 rigidPlates, used to apply support and pressure
mdb.models[modelName].rootAssembly.Instance(dependent=ON, name='support',
    part=mdb.models[modelName].parts['rigidPlate'])
mdb.models[modelName].rootAssembly.Instance(dependent=ON, name='impactor',
    part=mdb.models[modelName].parts['rigidPlate'])

#Create surface for sup and impactor
mdb.models[modelName].rootAssembly.Surface(name='surfSupport', side1Faces=      #
    side1/2Faces determine which side that is selected
    mdb.models[modelName].rootAssembly.instances['support'].faces.
        getByBoundingBox(
            -1.1*0.5*rigidPlateSize, -1, -1.1*0.5*rigidPlateSize, 1.1*0.5*rigidPlateSize
            , 1, 1.1*0.5*rigidPlateSize))
mdb.models[modelName].rootAssembly.Surface(name='surfImpactor', side2Faces=
    mdb.models[modelName].rootAssembly.instances['impactor'].faces.
        getByBoundingBox(
            -1.1*0.5*rigidPlateSize, -1, -1.1*0.5*rigidPlateSize, 1.1*0.5*rigidPlateSize
            , 1, 1.1*0.5*rigidPlateSize))

#Translate rigidPlates to correct spot (0.001 from cube surface)
mdb.models[modelName].rootAssembly.translate(instanceList=('support',), vector
    =(0.5*(lenXCube-lenXvoxel), hightSupport, 0.5*(lenZCube-lenZvoxel)))
mdb.models[modelName].rootAssembly.translate(instanceList=('impactor',), vector
    =(0.5*(lenXCube-lenXvoxel), hightImpactor, 0.5*(lenZCube-lenZvoxel)))

#Create set for rigidPlates for use in BC and HistoryOutputRequest
mdb.models[modelName].rootAssembly.Set(name='RP-Support', referencePoints=(
    mdb.models[modelName].rootAssembly.instances['support'].referencePoints[2],
    ))
mdb.models[modelName].rootAssembly.Set(name='RP-Impactor', referencePoints=(
    mdb.models[modelName].rootAssembly.instances['impactor'].referencePoints[2],
    ))

#Section Assignment
mdb.models[modelName].parts['MergedCylinder'].SectionAssignment(offset=0.0,
    offsetField='', offsetType=MIDDLE_SURFACE, region=Region(
    elements=mdb.models[modelName].parts['MergedCylinder'].elements[0:(
        numberOfvoxels*numberOfvoxels*numberOfImages)]),
    sectionName='Section-1', thicknessAssignment=FROM_SECTION)

#Re-import MergedCylinder to assembly to update instances after section
assignment
del mdb.models[modelName].rootAssembly.features['MergedCylinder-1']
mdb.models[modelName].rootAssembly.Instance(dependent=ON, name='MergedCylinder',
    part=
    mdb.models[modelName].parts['MergedCylinder'])

#=====
# 6. STEP
#=====
#Set the step to Abaqus/Explicit

```

```
mdb.models[modelName].ExplicitDynamicsStep(name='Explicit', previous='Initial',
timePeriod=stepTime)

#=====
# 7. INTERACTIONS
#=====
#Create interaction property for pores
mdb.models[modelName].ContactProperty('IntProp-Pores')
mdb.models[modelName].interactionProperties['IntProp-Pores'].TangentialBehavior(
dependencies=0, directionality=ISOTROPIC, elasticSlipStiffness=None,
formulation=PENALTY, fraction=0.005, maximumElasticSlip=FRACTION,
pressureDependency=OFF, shearStressLimit=None, slipRateDependency=OFF,
table=((fricInt, ), ), temperatureDependency=OFF)
mdb.models[modelName].interactionProperties['IntProp-Pores'].NormalBehavior(
allowSeparation=ON, constraintEnforcementMethod=DEFAULT,
pressureOverclosure=HARD)

#Create interaction property for surface
mdb.models[modelName].ContactProperty('IntProp-Surf')
mdb.models[modelName].interactionProperties['IntProp-Surf'].TangentialBehavior(
dependencies=0, directionality=ISOTROPIC, elasticSlipStiffness=None,
formulation=PENALTY, fraction=0.005, maximumElasticSlip=FRACTION,
pressureDependency=OFF, shearStressLimit=None, slipRateDependency=OFF,
table=((fricSurf, ), ), temperatureDependency=OFF)
mdb.models[modelName].interactionProperties['IntProp-Surf'].NormalBehavior(
allowSeparation=ON, constraintEnforcementMethod=DEFAULT,
pressureOverclosure=HARD)

#Create surface for merged cylinder
mdb.models[modelName].rootAssembly.Surface(face1Elements=
mdb.models[modelName].rootAssembly.instances['MergedCylinder'].elements.
getByBoundingBox(
-lenXvoxel, -lenYvoxel, -lenZvoxel, lenXCube+lenXvoxel, lenYCube+lenYvoxel,
lenZCube+lenZvoxel), name='surfSpecimen')

#Create general contact interaction
mdb.models[modelName].ContactExp(createStepName='Explicit', name='Contact')
mdb.models[modelName].interactions['Contact'].includedPairs.setValuesInStep(
stepName='Explicit', useAllstar=ON)
mdb.models[modelName].interactions['Contact'].contactPropertyAssignments.
appendInStep(
assignments=((GLOBAL, SELF, 'IntProp-Pores'), (
mdb.models[modelName].rootAssembly-surfaces['surfImpactor'],
mdb.models[modelName].rootAssembly-surfaces['surfSpecimen'],
'IntProp-Surf'), (
mdb.models[modelName].rootAssembly-surfaces['surfSupport'],
mdb.models[modelName].rootAssembly-surfaces['surfSpecimen'],
'IntProp-Surf'), (
mdb.models[modelName].rootAssembly-surfaces['surfSpecimen'], SELF,
'IntProp-Pores')), stepName='Explicit')

#=====
# 8. BOUNDARY CONDITIONS
#=====
#Fix the support
mdb.models[modelName].DisplacementBC(amplitude=UNSET, createStepName='Initial',
distributionType=UNIFORM, fieldName='', localCsys=None, name='Fixed',
region=mdb.models[modelName].rootAssembly.sets['RP-Support'], u1=SET, u2=
SET, u3=SET, ur1=SET, ur2=SET, ur3=SET)
```

```

#Create amplitude
mdb.models[modelName].SmoothStepAmplitude(data=((0.0, 0.0), (0.1*stepTime, 1.0))
, name=
  'RampVelocity', timeSpan=STEP)

#Set the velocity of the indenter
mdb.models[modelName].VelocityBC(amplitude='RampVelocity', createStepName=
  'Explicit', distributionType=UNIFORM, fieldName='', localCsys=None, name=
  'Load', region=mdb.models[modelName].rootAssembly.sets['RP-Impactor'], v1=
  0.0, v2=-velocity, v3=0.0, vr1=0.0, vr2=0.0, vr3=0.0)

#=====
# 9. FIELD AND HISTORY OUTPUT
#=====
mdb.models[modelName].HistoryOutputRequest(createStepName='Explicit', name=
  'ReactionForceImpactor', rebar=EXCLUDE, region=
  mdb.models[modelName].rootAssembly.sets['RP-Impactor'], sectionPoints=
  DEFAULT, variables=('RF2', 'U2'))

#=====
# 10. JOB
#=====
jobName = modelName + fricToJobSurf + fricToJobInt
mdb.Job(activateLoadBalancing=False, atTime=None, contactPrint=OFF,
  description='', echoPrint=OFF, explicitPrecision=DOUBLE_PLUS_PACK,
  historyPrint=OFF, memory=90, memoryUnits=PERCENTAGE, model=modelName,
  modelPrint=OFF, multiprocessingMode=DEFAULT, name=jobName,
  nodalOutputPrecision=FULL, numCpus=Cpus, numDomains=Cpus,
  parallelizationMethodExplicit=DOMAIN, queue=None, resultsFormat=ODB,
  scratch='', type=ANALYSIS, userSubroutine='', waitHours=0, waitMinutes=0)

mdb.jobs[jobName].writeInput()

#Save the model if saveModel=1
if saveModel == 1:
  mdb.saveAs(pathName = modelName + '.cae')

```